An investigation of microtubule-kinetochore attachment mechanisms

Lucas Edward Murray

A dissertation

submitted in partial fulfillment of the

requirements for the degree of

Doctor of Philosophy

University of Washington

2024

Reading Committee:

Chip Asbury, Chair

Trisha N. Davis

Linda Wordeman

Program Authorized to Offer Degree:

Physiology and Biophysics

University of Washington

Abstract

An investigation of microtubule-kinetochore attachment mechanisms

Lucas Edward Murray

Chair of the Supervisory Committee:

Chip Asbury

Department of Physiology and Biophysics

The ability to replicate is a defining feature of life. At the center of eukaryotic cell division are a set of protein machines responsible for pulling apart the chromosomes before cells divide. Spindle microtubules grow from the poles of the cell and connect to chromosomes via protein complexes called kinetochores. Kinetochores must maintain tenacious attachments to microtubule tips, even as they assemble and disassemble underneath their grip. Additionally, kinetochores mediate an error correction process to ensure the proper attachments to microtubules are formed before separation of the chromosomes commences. Here, I work to understand how the proteins in the kinetochore work together to maintain attachments to microtubules. I investigate two different mechanisms for microtubule-kinetochore attachment: the conformational wave mechanism and the biased diffusion mechanism. I developed a new optical trapping assay, using it to show that microtubule protofilament morphological and energetic properties can be measured and changed. I investigate the role of protofilament curl enlargement in the attachment and motility of the kinetochore. I develop theoretical models that show that the biased diffusion mechanism can fit experimentally measured detachment rates for assembling and disassembling kinetochores. Finally, I show kinetochores exhibit asymmetry in

their sliding friction when they are dragged along microtubule lattices, a new phenomenon for microtubule-kinetochore biophysics. I argue this sliding friction forms the basis for a new mode of error correction during cell division, one that likely holds across most eukaryotic organisms.

Chapter 1

Introduction

The ability to replicate is a defining feature of living organisms. During an average human lifetime, it is estimated that our cells undergo 10^{16}, or ten thousand trillion divisions [1]. Cell division is by necessity an accurate process: the loss rate for a yeast chromosome is approximately one per million per cell per generation [2]. However, the consequences for errors in division can be severe. Early in development, errors in cell division can cause birth defects, genetic disorders, and loss of viability. During a human lifespan, errors in division are a primary driver of cancer, which remains the second most common cause of death in the United States [3]. At the heart of the division process are a set of protein machines that facilitate the separation of chromosomes. Spindle microtubules are dynamic protein fibers that grow from organizing centers at each pole of the cell and connect to the chromosomes via protein complexes called kinetochores. For an accurate mitosis, the kinetochores must establish persistent attachments to the spindle microtubules, even as they grow and shorten by addition and loss of thousands of protein subunits per second. Additionally, the kinetochores must also sense and correct errors in attachment.

Significant recent progress has been made to describe the structure of kinetochore subcomplexes, and we therefore have an increasingly clear static picture of how kinetochore components are linked together. The dynamic behavior of attachments between intact kinetochore complexes and microtubules has also been well characterized under tension with optical traps [4]. We know from these studies that tension stabilizes attachments between the kinetochore complex and microtubules. The primary kinetochore proteins that interact with microtubules are also known [5-8]. However, agreement has not emerged over a clear mechanism that explains how proteins in the kinetochore dynamically work together to establish attachments to the correct microtubule tips and sustain such attachments.

Two popular models of kinetochore-microtubule attachment, the biased diffusion model and the conformational wave model, could explain the strength and persistence of attachments [9]. The conformational wave model posits that curling protofilaments at microtubule tips physically capture elements of the kinetochore and tug it along as the microtubule disassembles. There is evidence for ring-based couplers ideal for capturing such a curling motion in yeast, and the protein complex that makes up these rings (Dam1c) is essential for forming high-strength attachments [10]. However, there is not a ring-forming homolog in vertebrates. To test the conformational wave model, a way to modify the mechanical and energetic properties of microtubule protofilament curls was needed. Previous work in our lab established a method to measure the energy released by protofilament curling, and estimates of protofilament mechanics were made from these measurements [11]. Here, I develop new methods to show that the mechanics of protofilament curling can be changed, and that the energetics of tubulin bending are conserved. Results suggest the ring-forming protein dam1c can harness larger protofilament curls to increase attachment lifetimes I the context of the kinetochore.

The biased diffusion model posits that a kinetochore is composed of many low-affinity microtubule binders that diffuse along the lattice in a thermally driven random walk. It is more energetically favorable to have a larger number of diffusors bound to the lattice, driving motion of the coupler towards more binding. Even under external load, a biased diffusion coupler can sustain

attachment to an assembling or disassembling microtubule tip. Many of the proteins that are known to directly mediate the microtubule-kinetochore attachment have been shown to associate with the microtubule lattice and diffuse along its length, a hallmark of the biased diffusion mechanism [10, 12-14]. Furthermore, kinetochores are known to be composed of many copies of such proteins [15, 16]. However, measuring or changing the copy number or affinity of microtubule binding proteins in intact kinetochores remains challenging. Some progress has been made to control the copy number of microtubule-binding proteins in a synthetic kinetochore particle, but the detachment rate of such a complex was not tested [17]. Here, I develop several biased diffusion models that, unlike published counterparts, are fully parameterized from single-molecule biophysical data. These models incorporate kinetochore flexibility, sliding asymmetry, and feedback on microtubule dynamic rates to achieve predictions of detachment rates that closely match those measured for reconstituted in-vitro microtubule-kinetochore attachments.

During early mitosis, before bi-orientation, kinetochores first bind the sides of microtubules and subsequently find the plus ends by directed transport or when side-attached microtubules shorten and bring their ends to the kinetochores. Mitotic accuracy depends on selective release of erroneous attachments, but the proposed mechanisms focus mainly on plus-end attachments. Whether erroneous side-attachments are distinguished from correct side-attachments is unknown. Through work with other members of the lab, I show that side-attached kinetochores are highly sensitive to microtubule polarity, gripping six-fold more strongly when pulled toward plus versus minus ends. This directionally asymmetric grip correlates with changes in the axial arrangement of subcomplexes within the kinetochores, suggesting that internal architecture dictates attachment strength. We propose that the kinetochore's directional grip promotes accuracy specifically during early mitosis, by stabilizing correct attachments even before both sisters have found plus ends.

References

[1] R. Weinberg, *The Biology of cancer*.

[2] R. Kumaran, S. Y. Yang, and J. Y. Leu, "Characterization of Chromosome Stability in Diploid, Polyploid and Hybrid Yeast Cells," *Plos One,* vol. 8, Jul 2013.

[3] R. L. Siegel, K. D. Miller, H. E. Fuchs, and A. Jemal, "Cancer statistics, 2022," *Ca-a Cancer Journal for Clinicians,* vol. 72, pp. 7-33, Jan 2022.

[4] B. Akiyoshi, K. K. Sarangapani, A. F. Powers, C. R. Nelson, S. L. Reichow, H. Arellano-Santoyo*, et al.*, "Tension directly stabilizes reconstituted kinetochore-microtubule attachments," *Nature,* vol. 468, pp. 576-U255, Nov 2010.

[5] M. E. Pesenti, D. Prumbaum, P. Auckland, C. M. Smith, A. C. Faesen, A. Petrovic*, et al.*, "Reconstitution of a 26-Subunit Human Kinetochore Reveals Cooperative Microtubule Binding by CENP-OPQUR and NDC80," *Molecular Cell,* vol. 71, pp. 923-+, Sep 2018.

[6] M. E. Pesenti, T. Raisch, D. Conti, K. Walstein, I. Hoffmann, D. Vogt*, et al.*, "Structure of the human inner kinetochore CCAN complex and its significance for human centromere organization," *Molecular Cell,* vol. 82, pp. 2113-+, Jun 2022.

[7] K. W. Muir, C. Batters, T. Dendooven, J. Yang, Z. Zhang, A. Burt*, et al.*, "Structural mechanism of outer kinetochore Dam1-Ndc80 complex assembly on microtubules," *Science (New York, N.Y.),* vol. 382, pp. 1184-1190, 2023 12 08 (Epub 2023 Dec 2023.

[8] T. Dendooven, Z. G. Zhang, J. Yang, S. H. McLaughlin, J. Schwab, S. H. W. Scheres*, et al.*, "Cryo-EM structure of the complete inner kinetochore of the budding yeast point centromere," *Science Advances,* vol. 9, Jul 2023.

[9] C. L. Asbury, J. F. Tien, and T. N. Davis, "Kinetochores' gripping feat: conformational wave or biased diffusion?," *Trends in Cell Biology,* vol. 21, pp. 38-46, Jan 2011.

[10] N. T. Umbreit, M. P. Miller, J. F. Tien, J. C. Ortola, L. Gui, K. K. Lee*, et al.*, "Kinetochores require oligomerization of Dam1 complex to maintain microtubule attachments against tension and promote biorientation," *Nature Communications,* vol. 5, p. 11, Sep 2014.

[11] J. W. Driver, E. A. Geyer, M. E. Bailey, L. M. Rice, and C. L. Asbury, "Direct measurement of conformational strain energy in protofilaments curling outward from disassembling microtubule tips," *Elife,* vol. 6, p. 18, Jun 2017.

[12] E. A. Geyer, M. P. Miller, C. A. Brautigam, S. Biggins, and L. M. Rice, "Design principles of a microtubule polymerase," *Elife,* vol. 7, p. 23, Jun 2018.

[13] N. T. Umbreit, D. R. Gestaut, J. F. Tien, B. S. Vollmar, T. Gonen, C. L. Asbury*, et al.*, "The Ndc80 kinetochore complex directly modulates microtubule dynamics," *Proceedings of the National Academy of Sciences of the United States of America,* vol. 109, pp. 16113-16118, Oct 2012.

[14] L. A. Helgeson, A. Zelter, M. Riffle, M. J. MacCoss, C. L. Asbury, and T. N. Davis, "Human Ska complex and Ndc80 complex interact to form a load-bearing assembly that strengthens kinetochore-microtubule attachments," *Proceedings of the National Academy of Sciences of the United States of America,* vol. 115, pp. 2740-2745, Mar 2018.

[15] K. Johnston, A. Joglekar, T. Hori, A. Suzuki, T. Fukagawa, and E. D. Salmon, "Vertebrate kinetochore protein architecture: protein copy number," *Journal of Cell Biology,* vol. 189, pp. 937-943, Jun 2010.

[16] A. P. Joglekar, D. C. Bouck, J. N. Molk, K. S. Bloom, and E. D. Salmon, "Molecular architecture of a kinetochore-microtubule attachment site," *Nature Cell Biology,* vol. 8, pp. 581-585, Jun 2006.

[17] V. A. Volkovn, P. J. H. in't Veldt, M. Dogterom, and A. Musacchio, "Multivalency of NDC80 in the outer kinetochore is essential to track shortening microtubules and generate forces," *Elife,* vol. 7, Apr 2018.

Chapter 2

Measuring the working strokes of protofilaments as they curl outward from disassembling microtubule tips

Originally published in Optical Tweezers. Methods in Microbiology , vol. 2478 (2022) 653-676

ABSTRACT

Optical traps have enabled foundational studies of how mechanoenzymes such as kinesins and dynein motors walk along microtubules, how myosins move along F-actin, and how nucleic acid enzymes move along DNA or RNA. Often these filamentous substrates serve merely as passive tracks for mechanoenzymes. However, microtubules and F-actin are themselves dynamic protein polymers capable of generating movement and force independently of conventional motors. Microtubule-driven forces are particularly important during mitosis, where they align duplicated chromosomes at the metaphase plate and then pull them apart during anaphase. These vital movements depend on specialized protein assemblies called kinetochores that couple the chromosomes to the tips of dynamic microtubule filaments, thereby allowing filament shortening to produce pulling forces. Although great strides have been made towards understanding the structures and functions of many kinetochore subcomplexes, the biophysical basis for their coupling to microtubule tips remains unclear. During tip disassembly, strain energy is released when straight protofilaments in the microtubule lattice curl outward, creating a conformational wave that propagates down the microtubule. A popular viewpoint is that these curling protofilaments hook elements of the kinetochore and tug on them, transferring some of their curvature strain energy to the kinetochore. As a first step toward testing this idea, we recently developed a laser trap assay to directly measure the working strokes generated by curling protofilaments. Our 'wave' assay is based on an earlier pioneering study, with improvements to allow curl-driven movements to be measured as functions of force and to quantify the conformational strain energy they carry. In this chapter, we provide a detailed protocol for our assay and describe briefly our instrument set-up and data analysis methods.

Introduction:

Optical tweezers have proven to be ideal tools to study the mechanochemistry of a wide variety of biological molecules and processes. Since Arthur Ashkin's seminal work introducing the optical trap to the world [5], the technique has been used extensively to study the motions and forces produced by single kinesins and dynein on microtubules [6-9], by myosins on F-actin fibers [10-12], by polymerases along DNA and RNA [13,14], and many other mechanoenzymes [15-17]. Often the filamentous substrates (microtubules, F-actin, or DNA) can be considered passive tracks along which the motor enzymes move. However, in some important instances microtubules [18-22] and F-actin [23-25] can themselves produce movement and force independently of conventional motor enzymes. Here, we describe an optical trapping-based assay to measure the mechanical work output generated by individual disassembling microtubule tips (fig. 1).

Microtubules are hollow, filamentous protein polymers that grow and shorten by rapid addition and loss of αβ-tubulin heterodimers from their tips. αβ-tubulin subunits are GTP-hydrolyzing (GTPase) enzymes that associate together in two fundamental ways to form a microtubule: longitudinal (head-to-

tail) associations form protofilaments, while lateral (side-to-side) associations bridge these protofilaments, usually in groups of 13, to form the hollow microtubule body. Because free αβ-tubulin subunits adopt a curved conformation that must straighten to accommodate formation of lateral interactions with neighboring subunits in the lattice, the lattice holds strain energy [26,27]. After GTP-tubulin heterodimers are embedded in the microtubule lattice, their GTPase activity is stimulated and the lattice is destabilized. Strained αβ-tubulin subunits trapped in the lattice can only release their stored energy during tip disassembly, when protofilaments curl outwards from the tip and splay apart. These curling protofilaments form a conformational wave that propagates down the microtubule. Lattice strain energy is fundamentally important for all current models of microtubule dynamic instability but, until recently, its magnitude could only be estimated indirectly, using thermodynamic approaches or analyses based on the bending rigidity of intact microtubules [28-30]. The assay described here provides a more direct approach.

Dynamic microtubules are also the basis of the mitotic spindle that aligns and segregates duplicated chromosomes during eukaryotic cell division [31]. The vital chromosome movements of mitosis are generated when spindle microtubules shorten, thereby pulling against specialized protein structures on each chromosome called kinetochores. The kinetochores harness energy released from disassembling microtubules by maintaining persistent, load-bearing attachments to the filament tips, even as the tips crumble beneath them [18,32,19,20]. Despite great progress in understanding the molecular structures of both kinetochore subcomplexes and microtubules, it remains unclear how kinetochores remain coupled to dynamic microtubule tips and how they harness the energy released during tip disassembly [33]. According to one of the leading models, the conformational wave model, curling protofilaments at disassembling microtubule tips physically capture and pull on elements of the kinetochore to drive motility [18]. Alternatively, coupling could be maintained by biased diffusion, which can operate independently of any spring-like curling action of the protofilaments [34].

Using the optical trapping assay describe here, we recently showed that protofilaments indeed release substantial mechanical energy as they curl outward from disassembling microtubule tips, and this energy (when extrapolated) is more than sufficient to account for kinetochore movement in vitro [1]. To measure the energy carried by the conformational wave, we modified an assay pioneered in an earlier study [35], adding a feedback-controlled laser trap and other improvements to prevent the microbeads used in the assay from restricting the curling of the protofilaments. We describe our protocol in detail here, including how to prepare a disposable channel slide sparsely decorated with coverslip-anchored microtubules, some of which have microbeads tethered to their sides. The microbeads become tethered by virtue of being sparsely decorated with recombinant yeast tubulin, which incorporates into growing microtubule tips. This tethered bead arrangement forms a mechanical lever that amplifies the molecular-scale motions generated by the curling protofilaments and enables their measurement in an optical trap. In addition to slide preparation and trapping procedures, we also describe data interpretation and analysis.

Because this “wave assay” provides a direct way to measure protofilament strain energy, it will be essential for testing rigorously whether curling protofilaments contribute to kinetochore-microtubule coupling. Already the assay has demonstrated the spring-like elasticity of protofilament curls and established that they carry sufficient energy to explain microtubule-driven kinetochore motility. But rigorously testing their importance for kinetochore motility will also require modifying their energy and measuring how such modifications affect kinetochore-microtubule coupling. We envision that the wave

assay will be useful for identifying assay conditions or tubulin mutants that alter wave energy and, more generally, for examining the mechanochemistry of tubulins from different organisms and/or with various post-translational modifications.

Materials:

1.1. Instrument Design and Optical Layout

Our instruments feature a simple fixed laser trap, with feedback control implemented via movement of a computer-controlled piezo specimen stage (fig. 2). Video-enhanced differential interference contrast (ve-DIC) optics are included for visualization of microtubules and beads, and an additional 473-nm laser is included for optical severing of microtubules (i.e., laser 'scissors'). The instruments are constructed on standard inverted research microscopes and include some custom mounting hardware. Their construction and optical layout is detailed in prior publication [36]. This assay should be able to be performed on any microscope equipped with a feedback-controlled optical trap, cutting laser, and DIC optics for viewing individual, unlabeled microtubules.

1.2. Tubulin purification

The wave assay as described here relies on purified, tagged recombinant yeast tubulin. A 6x-His-tag on the C-terminal tail of the β-subunit of this recombinant tubulin allows the αβ-tubulin heterodimers to be strongly tethered to streptavidin-coated microbeads functionalized with biotinylated anti-penta-His antibody. The recombinant yeast tubulin has been purified from an *S. cerevisiae* strain with an inducible overexpression system, aliquoted and snap-frozen, shipped on dry ice, and stored at -80 °C. The method for tubulin preparation is detailed in prior publications [37,38]. Though the protocol we present relies on this recombinant yeast tubulin, any similarly tagged tubulin should work for the purposes of this assay. Our past work suggests that whatever method is used to tether tubulin to a microbead, a tether of sufficient length between the bead and the tubulin is required. We estimate that our tether length is approximately 36 nm when the streptavidin, antibody, and C-terminal tail of tubulin are considered. With the use of 440-nm microbeads, we estimate a leverage of 2 to 2.5-fold (i.e., trapping forces exerted parallel to the microtubule long-axis cause 2 to 2.5-fold larger normal forces exerted laterally against the curling protofilaments) (fig. 9a-b). Without a source for recombinant tubulin, a tether of sufficient length could be recapitulated by linking anti-digoxygenin-coated beads to biotinylated tubulin via a bifunctional DNA molecule.

Regardless of the tethering method, waves generated by native tubulin purified from bovine brain can be measured in the assay. The methods by which this we incorporate native, untagged tubulin into the wave assay are described below. Purification of tubulin from bovine brain is detailed in a prior publication [21]. Alternatively, porcine brain tubulin can be purified or purchased from Cytoskeleton Inc. or PurSolutions

1.3. Biotin-tubulin microtubule seed preparation

1. 5X BRB80 buffer: 400 mM PIPES, 5 mM $MgCl_2$, 2.5 mM EGTA (doi:10.1101/pdb.rec086694).
2. Biotinylated porcine tubulin (Cytoskeleton Cat #T333).
3. Bovine or porcine brain tubulin (purified as in [39] or purchased from Cytoskeleton Inc. e.g. Cat. #HTS03).
4. GMPCPP 10 mM (Jena Bioscience Cat #NU-405S).
5. Purified water (Milli-Q water is used here "MQ-H_2O", but double-distilled will likely suffice).

6. 1,4-dithiothreotol (DTT) 40 mM in MQ-H_2O (Sigma cat # 10197777001).
7. 80% glycerol (20% MQ-H_2O).
8. Bucket of ice.
9. Heat Block equilibrated to 30 °C (Thermo Fischer Cat # 88870001).

1.4. Anti-His bead preparation

1. MQ-H_2O.
2. 5X BRB80 buffer: 400 mM PIPES, 5 mM $MgCl_2$, 2.5 mM EGTA (doi:10.1101/pdb.rec086694).
3. Streptavidin coated polystyrene beads, 440 nm in diameter, 1% weight/volume (Spherotech Cat #SVP-05-10).
4. Penta-His biotin conjugate (Qiagen Cat #34440), a mouse monoclonal IgG1 antibody that binds tightly and specifically to five (or more) consecutive Histidine residues and is conjugated to biotin.
5. Bovine serum albumin (BSA) (Calbiochem cat # 126609) 40 mg/mL in 1X BRB80.
6. 1,4-dithiothreotol (DTT) 1 M in MQ-H_2O (Sigma cat # 10197777001).
7. Tip Sonicator (Branson Ultrasonics Sonifier S-250A) with ½-inch diameter tip.
8. Tube rotator (Thermo Fisher C415110), placed in a cold room or refrigerated cabinet at 4 °C.
9. Benchtop centrifuge (Eppendorf model 5415 D), placed in a cold-room or refrigerated cabinet.

1.5. Disposable channel slides

1. KOH cleaned coverslips, protocol described in prior work [36].
2. Microscope slides (Gold Seal #3011).
3. Double-stick office tape (Scotch #665-6).
4. Oven (Thermo Fisher PR305225G), equilibrated to to 55 °C.
5. Slide humidity chamber: briefly, a 200 µL pipette tip box is adapted to hold a disposable channel slide. Two razor blades are taped down to the tip tray to act as standoffs to support the slide. A damp paper towel is placed under the tip tray to keep enough humidity in the box to prevent rapid drying of the slide during the incubation steps described below in section 3.5.

1.6. Preparing coverslip-anchored microtubules with side-bound microbeads

1. 5X BRB80 buffer: 400 mM PIPES, 5 mM $MgCl_2$, 2.5 mM EGTA (doi:10.1101/pdb.rec086694).
2. Anti-His beads (prepared as described below in section 3.3 using materials from 2.4 above).
3. Bovine serum albumin (BSA) (Calbiochem cat # 126609), >150 mg/mL in 1X BRB80, filtered at 0.1 µm.
4. 100 mM GTP (Sigma G8877) in MQ-H_2O, buffered to pH 7.
5. Biotinylated bovine serum albumin (Vector Laboratories B-2007-10).
6. Avidin DN (Vector Laboratories A-3100-1).
7. Biotin-tubulin microtubule seeds (prepared as described below in 3.2, using materials in 2.3).
8. MQ-H_2O, filtered at 0.1 µm.
9. 1,4-dithiothreotol (DTT) (Sigma cat # 10197777001), 40 mM in MQ-H_2O .
10. Glucose, 2.4 M in MQ-H_2O.
11. Recombinant yeast tubulin (2 to 5 µM).
12. Bovine brain tubulin (assumes 190 µM) (optional, see Methods).

13. Oxygen scavenger 100X (glucose oxidase + catalase) (Sigma Cat. #G2133, Sigma Cat #C3515). Mix to 10,000 units/mL glucose oxidase, 100,000 units/mL catalase, in 1X BRB80. Filter at 0.1 µm, aliquot into 5 µL volumes and freeze in liquid N_2.
14. Clear nail polish.
15. Ultra-centrifuge capable of reaching 90,000 RCF at 4 °C and TLA-100 rotor (e.g. Beckman-Coulter Optima MAX-XP Ultracentrifuge and TLA-100 fixed-angle rotor), or 0.1 µm centrifugal spin filter (e.g. EMD-Millipore cat# UFC30VV). Spin filters have been associated with ~50% tubulin loss in our hands, but are a more affordable option if an ultracentrifuge is not accessible.

1.7. Measuring pulses of motion generated by curling protofilaments

1. Suitable optical trap, e.g. constructed as in reference [36]. The trap should be operable in 'force clamp' mode, with the force kept constant under feedback control.
2. The LabView code that we use to implement feedback can be freely downloaded from prior publication [1], and we are happy to offer assistance or advice on its use.

Methods:

3.1. Tubulin purification

1. Purification of recombinant tubulin from yeast is detailed in prior publication [37,38].
2. Purification of tubulin from bovine brain is detailed in prior publication [39].

3.2. Biotin-tubulin microtubule seed preparation

1. Make 2X Nucleation Buffer (NB) (65 µL 80% glycerol, 100 µL 5X BRB80, 50 µL 10 mM GMPCPP, 10 µL 40 mM DTT, 25 µL MQ-H_2O), place on ice.
2. Reconstitute 20 µg of biotin tubulin (Cytoskeleton, Cat #T333) in 10 µL of ice-cold 1X BRB80.
1. Add 240 µg of bovine brain tubulin (12.6 µL of 190 µM bovine tubulin) to the reconstituted biotin tubulin from step 2 (target ratio is 7 to 8.5% biotinylated tubulin). Add enough 1X BRB80 to make the final volume 50 µL. This should yield a solution of 4 to 5 µM tubulin.
2. Mix 40 µL of the tubulin mix from Step 3 with 250 µL 2X NB and 210 µL of MQ-H_2O. *Final concentrations in the seed nucleation mixture:* 10% glycerol, 1X BRB80, 1mM GMPCPP, 0.8mM DTT, 4.8 µM bovine tubulin, 0.4 µM biotinylated tubulin
3. Incubate 1 hr at 37 °C, then snap freeze in 15 µL aliquots. Store at -80 °C. When thawing, transfer directly to 30 °C, attempting to keep aliquot's transit through the 0 to 15 °C temperature range as brief as possible.
4. Check seeds by visualizing product using ve-DIC (look for microtubules 1-3 µm In length). Their nucleation capacity can be tested by growing microtubules from bovine brain tubulin according to, "Preparing coverslip-anchored microtubules with side-bound microbeads" (see section 3.5 below), optionally omitting the beads.

3.3. Anti-His bead preparation

1. In a 500 µL eppendorf tube, mix 145 µL of MQ-H_2O, 53 µL 5X BRB80 and 22.5 µL 440 nm streptavidin coated polystyrene beads.
2. Sonicate in ice-water bath for 5 min, to break up bead clumps that tend to form in the concentrated bead stock. We use a custom jig made of wire to hold a 500 µL Eppendorf tube directly in front of the ½ -inch sonicator tip. Both tube and tip are submerged in ice-water during sonication to minimize heating.
3. Mix sonicated beads with 4.5 µL Penta-His biotin conjugate, set on rotator at 4 °C for 1 hr to allow binding of biotinylated antibodies to streptavidin on the beads.
4. Make assay buffer (AB) (1.5 mL 40 mg/mL BSA, 1.5 mL 5X BRB80, 4.5 mL MQ-H_2O, 7.5 µL 1 M DTT). Filter at 0.1 µm. *Final assay buffer concentration:* 8 mg/mL BSA, 1X BRB80, 1 mM DTT.
5. Increase the volume of bead mix to 500 µL by adding 275 µL of Assay Buffer (AB).
6. Resuspend gently, sonicate 1 min and resuspend again to encourage bead clumps to break apart and ensure the bead mix is as homogenous as possible.
7. Spin at 13,000 RPM for 9 min at 4 °C to separate beads from antibody-containing solution. Gently aspirate and discard supernatant, leaving just enough to keep bulk of pellet hydrated. Quickly re-suspend pellet in 500 µL AB. Sonicate 1 min.
8. Repeat step 7 five times. At the last re-suspension, re-suspend pellet to make a final volume of 225 µL. *Final concentrations in the anti-His bead mixture:* 8 mg/mL BSA, 1X BRB80, 1 mM DTT, 60pM 440-nm polystyrene beads.
9. Store Anti-His beads on tube rotator at 4 °C, rotating continuously for up to one month. Ensure that the beads are freely dispersed in solution prior to use. Formation of a web-like precipitate has been associated with beads that do not perform as expected in assays.

3.4. Preparing disposable channel slides

1. Place a microscope slide on a clean, flat surface.
2. Lightly stretch 3-inch strips of ¼-inch wide double-stick tape, adhering tape perpendicular to the microscope slide to define channel boundaries, securing tape at each end to the underlying surface. Three strips of tape should allow construction of two 1mm wide channels (fig 3). When constructed properly, the channels should be perpendicular to the microscope slide, allowing the slide to be loaded with solution via pipette while in the coverslip-down position.
3. Trim the tape at the edge of the microscope slide with a razor blade.
4. Lightly adhere a KOH-cleaned coverslip to the tape pattern on the microscope slide, orienting the long dimension of the coverslip orthogonally to the long dimension of the slide.
5. Use a 1 mL pipette tip to press down, and back and forth on areas of the glass-tape sandwich to fully seal the chamber sides.
6. Place the newly constructed chamber in a heated oven at 55 °C for at least 10 min prior to filling chambers with buffers.
7. .

3.5. Preparing coverslip-anchored microtubules with side-bound microbeads

The steps below describe how to produce a slide sparsely decorated with coverslip-anchored dynamic microtubules, with beads tethered to the sides of some microtubules. The wave assay developed in our lab originally relied entirely on recombinant yeast tubulin. We have since adapted our approach to allow other tubulin sources to be used, including native brain tubulin. Incorporating native, untagged tubulin requires some additional steps, which are indicated as "optional" below.

1. Place TLA-100 rotor with two tubes on cold-block in 4 °C fridge. Turn on Ultra-centrifuge, set to 4 °C, turn on vacuum.
2. Prepare two 1 mL aliquots of 1XBRB80. Place one on ice, one at 37 °C.
3. Prepare 120 µL 40 mg/mL BSA from high-concentration stock. Place on ice.
4. Prepare 50 µL 40 mM DTT. Store at room temp.
5. Prepare 2X growth buffer (2X GB): mix 21 µL MQ-H_2O, 48 µL 5X BRB80, 48 µL 40 mg/mL BSA, 3 µL 100 mM GTP. Place on ice.
6. Prepare 1X GB: mix 50 µL 2X GB, 50 µL MQ-H_2O. Place on ice.
7. Prepare reaction mix (RXN) (fig. 3i): mix 25 µL 2X GB, 1 µL 40 mM DTT, 1 µL 2.4 M glucose.
8. Make bead dilution (fig 3ii): mix 5 µL 40 mg/mL BSA, 5 µL biotinylated BSA, 17.5 µL anti-His beads. Sonicate for 5 min on ice at 8 intensity, constant pulse. Incubate for 25 mins, rotating at 4 °C. Including biotinylated BSA is important during this incubation step to ensure that any remaining streptavidin, not already bound to biotinylated anti-His antibody, becomes occupied. Fully occupying the streptavidin prevents direct binding of beads to biotinylated coverslip-anchored microtubule seeds, an arrangement that would be difficult to distinguish from the desired tethering, where beads are attached via anti-His antibodies and C-terminal tubulin tails to the sides of microtubule extensions.
9. Make flow chamber with KOH-cleaned coverslip and double-stick tape according to instructions in section 3.4 (fig. 3iii). Warm in 55 °C oven for 15 min.
10. Add 35 µL of biotinylated BSA (BBSA) to an empty eppendorf tube, incubate at 37 °C. Add 35 µL of Avidin DN to another empty eppendorf tube, incubate at 37 °C.

11. Initialize microscope: turn on Hg-arc lamp, trap laser, set trap laser power, turn on cutting laser.
12. Start slide incubation (fig. 3iv): add 15 µL BBSA to each lane on a slide fresh from oven, aspirating from one end of a channel to pull 15 µL through. Place the filled slide in a humid slide box, avoiding dirtying the coverslip via contact with other surfaces, and incubate for 15 min.
13. Clarify tubulin (fig. 3v): When bead dilution mix from step 7 above has incubated for 17 of its full 25 min, spin recombinant yeast tubulin in cold TLA-100 rotor at 90,000 RPM, 4 °C, 10 min in Ultra-centrifuge.
14. Functionalize beads (fig. 3vi, skip this step if performing an assay with recombinant tubulin alone) When bead dilution from step 7 has incubated for its full 25 min, add 5 to 10 µL 2 to 7 µM of yeast tubulin directly from rotor to bead dilution, pipetting from the center of the supernatant to avoid accidentally collecting any pelleted debris. Mix gently but thoroughly by pipetting and incubate 10 min at 4 °C, rotating, to allow binding of His-tagged recombinant tubulin to anti-His antibodies on beads.
15. Wash beads (fig 3vi, skip this step if performing an assay with recombinant tubulin alone) Simultaneous with slide incubation, spin functionalized beads (now carrying yeast tubulin) at 4 °C, in cold benchtop centrifuge at 13,000 RPM, 10 min. Discard supernatant (try to keep beads from contacting air), re-suspend in 27.5 µL cold 1XGB + 1 µL BBSA.
16. Slide Incubation (fig 3vii): After slide prepared in step 12 above has incubated (with BBSA) for its full 15 min, wash each lane with 80 µL warm 1X BRB80. Add 15 µL of avidin DN to each lane. Incubate slide in humidity chamber for 5 min.
17. Retrieve Biotin-tubulin microtubule seeds from -80 °C freezer, transfer quickly to 37 °C
18. Slide Incubation (fig 3viii): wash each lane with 40 µL warm 1X BRB80. Dilute 1 to 10 µL of warm seeds in 50 µL BRB80 (according to desired density of microtubule seeds on slide surface). Add 15 µL diluted seeds to each lane and incubate for 5 mins in humidity chamber. Warm 1X GB by placing on 37 °C block.
19. Remove any unbound microtubule seeds by washing each lane with 20 µL warm 1X GB. Incubate slide in humidity chamber.
20. Finish reaction mix (fig. 3ix): Add to RXN: tubulin (to a target concentration of 12 to 20 µM for bovine tubulin, or 1.5 to 3 µM for yeast tubulin), 4 µL of bead dilution, 1 µL of 100X oxygen scavenger, and enough cold 1X BRB80 to bring the reaction mix volume to 50 µL. Mix thoroughly by pipetting. *Final concentrations in reaction mix:* 1X BRB80, 8 mg/mL BSA, 1 mM DTT, 12 to 20 µM bovine tubulin or 1.5 to 3 µM yeast tubulin, ~3 pM beads, 1 mM GTP, 1 mM DTT, 25 to 50 mM glucose, ~200 µg/mL glucose oxidase, ~35 µg/mL catalase.
21. Add reaction mix to chamber, seal edges with nail polish (fig. 3x). Mount the slide on the optical trap. Monitor the coverslip surface by ve-DIC for microtubule growth from coverslip-anchored seeds and free-floating tubulin-coated beads. Tubulin coated beads become incorporated into microtubules at their growing tips, remaining attached at their point of incorporation as the microtubule continues to grow. Such beads are observed subsequently as side-attached to a coverslip-anchored, growing microtubule.

We note that several aspects of the preparation must be optimized to produce a sufficient number of coverslip-anchored microtubules with side-attached beads that do not contact other microtubules. First, the density of microtubule seeds on the surface should be tuned low enough to mitigate microtubules contacting each other during growth, but high enough so the tubulin-decorated beads can encounter and incorporate into growing tips. Moreover, the

concentration of free tubulin should be tuned high enough that microtubules are predominantly in their growth regime, with catastrophes minimized, but not so high that overgrowth leads to significant contact of microtubules with each other (crossing or bundling). Lastly, we use the concentration of anti-His antibody to tune the amount of tubulin on the surface of the tubulin-decorated beads. If beads are decorated too densely with tubulin, then their binding to a growing tip can inhibit further polymerization, and most microtubule-bound beads are seen in a "lollipop" configuration, without any microtubule extension past the bead (see fig 3b). This configuration is unusable in the wave assay. Microtubules that only disassemble to a side-attached bead and no further are another indicator that the tubulin density on the beads is too high. In both of these cases, we suspect that multiple attachments between bead and microtubule stabilize the lattice. The amount of tubulin on beads may be tuned down to the single-molecule level by adjusting the antibody level such that only 50% of beads bind when held in contact with a growing microtubule tip (this procedure is documented in reference [1]).

We suggest that tubulin, especially recombinant tubulin, should be used as quickly as possible after thawing. Tubulin aliquots should be handled such that they transit through the thaw process as quickly as possible (e.g., thawing by holding a tube in hand), with all subsequent handling at 4 °C (on ice). In our experience, recombinant tubulin is prone to aggregation, and aggregation increases with time, temperature, and concentration. We include a clarifying ultracentrifugation step in this protocol to eliminate any aggregate already present in freshly thawed tubulin samples. When large aggregates are present on a slide prepared as described section 3.5, we observe heavy decoration of aggregate with anti-His beads, depletion of free beads in solution, and slower growth of surface-attached microtubules. We therefore suspect tubulin aggregate can act as a sink for anti-His beads and free tubulin, effectively limiting the time during which the slide prepared in section 3.5 can be used for the measurements described in section 3.6. In addition, aggregates directly interfere with trapping of anti-His beads as aggregates are attracted to the trap. Therefore, depending on the particular lab setup and experimental practices, we recommend the timing of steps 13 through 15 and step 20 above (in section 3.5) be adjusted to minimize the time between thawing and using tubulin, and minimize instances where tubulin aliquots are above 4 °C.

3.6. Measuring pulses of motion generated by curling protofilaments

The optical trap setup used for this assay is described in previous work [36]. Briefly, a 1064-nm laser is used as a trapping beam, and a 473-nm laser as a microtubule cutting beam. The 1064-nm laser is focused at the center of the field of view. The 473nm cutting laser is focused into an ellipse at an intermediate distance between the trap center and the edge of the field of view. Both lasers are actuated independently by shutters. To measure pulses generated by protofilaments curling outward from disassembling microtubule tips:

1. Identify a suitable bead laterally attached to a microtubule (fig. 5b). This microtubule should be firmly anchored to the slide surface, able to freely rotate about its surface anchor, and without other interfering microtubules bundled alongside or crossing along its length. The microtubule will need to be oriented such that its plus end intersects with the cutting beam. Suitable microtubules with side-bound beads are sometimes found already in this orientation. However, in cases where an otherwise suitable microtubule is misoriented, we often find that by using the trap it is possible to reorient them by swiveling them about their coverslip-anchor. The cutting laser can also sometimes be used to trim away interfering microtubules.
2. Establish initial loaded state: Trap the laterally attached bead and pull the microtubule and bead towards cutting laser. Raise the bead slightly above the coverslip surface to ensure

the surface does not interfere with the measurement. Turn on the force clamp, placing the bead and microtubule under tension, with the plus-end of the microtubule passing though the cutting region.

3. Initiate microtubule depolymerization by trimming off the stabilizing cap of the microtubule using the cutting laser. Record position signals from the trapped bead using the force clamp software. When the bead detaches from the microtubule, stop the force clamp software and make relevant notes for the bead-microtubule pair.

3.7. Analyzing wave assay data

Our optical traps use a simple stage-based feedback-control. Therefore, the stage and bead position signals encode the pulse data to be analyzed. Bead-trap separation encodes the level of force and is then decimated to 200 Hz before recording. The stage position encodes bead movement relative to the coverslip and is updated and stored at 50 Hz. Each pulse event is captured with a 10 to 20s recording of the stage and trap separation signals.

Our custom analysis software (written in IGOR Pro, Wavemetrics) facilitates data analysis and is available upon request, but data can be analyzed relatively easily using any data processing software. Briefly, the stage position along the x-axis (parallel with the microtubule axis) is plotted against time to visualize microtubule disassembly-driven pulses (fig. 6a). A pulse can be parameterized by its amplitude, risetime, and ability to be differentiated from baseline noise (fig 6a,b). We define pulse amplitude as the difference between the maximum value at the peak and the arithmetic mean of at least 2 seconds of the signal directly prior to the pulse. We require an amplitude of at least 3 times the RMSD of the baseline noise for a candidate pulse to be valid. Pulse amplitudes for recombinant yeast tubulin range from 40 to 100 nm, well above the mean baseline noise (RMSD ≈ 4 nm), making them easily distinguishable (fig. 7). Pulse risetimes (i.e the times for the pulses to depart from the baseline and reach their maximum value) typically range from 100 to 400 ms.

The geometric arrangement of the bead, tether, and microtubule in the wave assay creates a lever system that amplifies protofilament curl motions by a modest amount that is sensitive to tether length and bead size (fig 9a, [1]). Figure 9b shows the predicted relationship between pulse amplitude and curl height for a 36 nm tether and a 440 nm bead. The amplification in this case is 2 to 2.5-fold, and the pulse amplitude varies roughly linearly with curl height until the height approaches the tether length.

By enabling measurements of pulse properties as functions of force, the wave assay provides a unique window into both the mechanics and thermodynamics of microtubule tip disassembly. Pulse amplitudes measured in the wave assay decrease as the force of the laser trap is increased (fig. 8), demonstrating directly that curling protofilaments behave like springs. The area under the pulse amplitude vs. force curve (which is independent of geometric details such as bead size) represents the total available mechanical work output from the subset of curling protofilaments that push against the microbead. The total work available from yeast tubulin pulses, W ~ 300 pN·nm, is a substantial amount of mechanical energy, roughly 70-fold greater than thermal energy (k_BT ~ 4.1 pN.nm) [1].

This large capacity for work output in the wave assay can be related to fundamental thermodynamic properties, such as the total mechanical energy released by *all* the protofilaments curling out from a disassembling microtubule tip (i.e., not just the subset that pushes against the microbead), and also

the curvature strain energy per tubulin dimer, given estimates for the fraction of protofilaments and the number of tubulin dimers that produce force in the assay (fig. 9c). Based on the geometry of the bead and tether, we estimate that a maximum of four protofilaments could push simultaneously against the bead (fig 9d), which implies that W represents only about one-third of the total mechanical energy available from the entire disassembling tip (4 out of 13 protofilaments, or 31%). Based on the morphological characteristics of curling protofilaments seen in electron micrographs [40,2,41], we infer that curling protofilaments typically contain about four tubulin dimers, which suggests a maximum of 16 tubulin dimers (4 curls with 4 dimers each) might contribute to W and therefore that the strain energy per tubulin dimer is at least 19 pN.nm (i.e., W divided by 16). We consider this estimate a lower-bound because it assumes simultaneous pushing by four protofilaments, which might not always occur. Nevertheless, it corresponds to approximately 22% of the total energy available from GTP hydrolysis.

The energetic estimates obtained here using the wave assay show that protofilament curls are powerful and carry a substantial fraction of the energy transduced from GTP hydrolysis by tubulin. Determining mechanistically how this mechanical energy is harnessed, and how much of it is harnessed by kinetochores and other microtubule tip-couplers is an area for future work. The wave assay will be useful for this endeavor because of its unique ability to directly assess the mechanical strain energy released by curling protofilaments, and to test strategies for altering this strain energy.

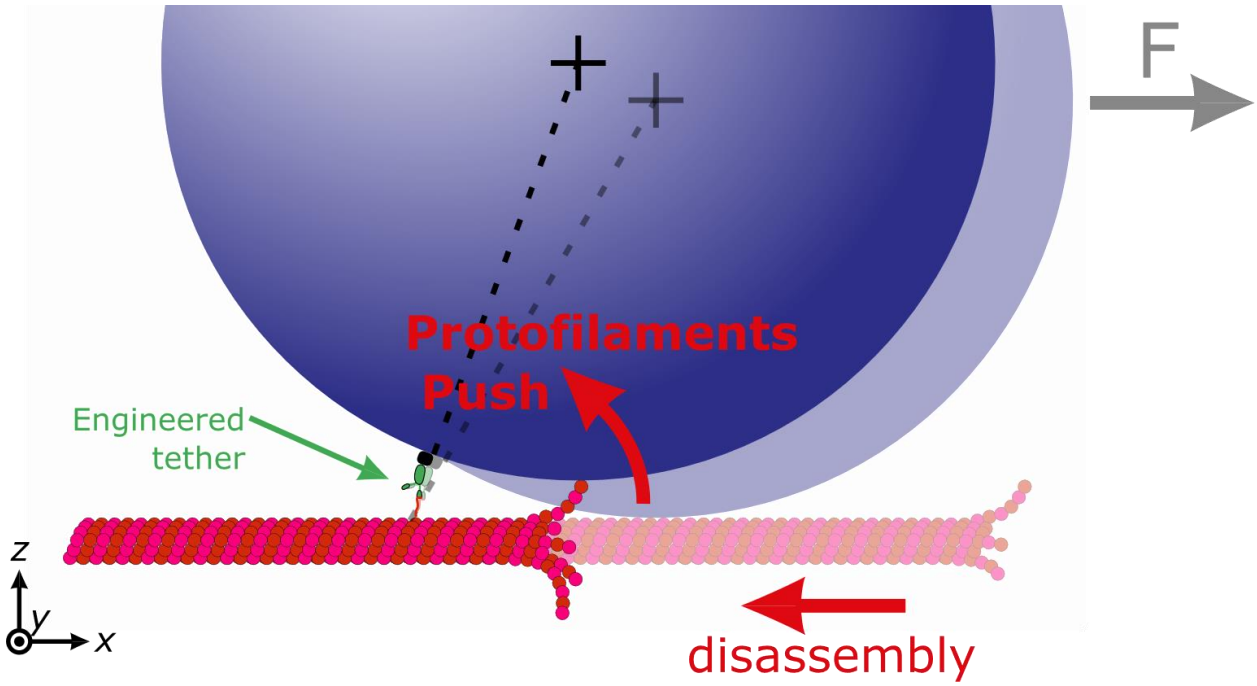

Figure 1: Curling protofilaments at a disassembling microtubule tip cause a pulse in bead-motion parallel to the microtubule axis. A streptavidin-coated microsphere (blue with center marked by black cross) is attached to a microtubule composed of recombinant 6x-His-tagged yeast tubulin (pink and red) by an anti-penta-His antibody (green). The bead is pulled rightward with a feedback-controlled optical trap such that it rests against the side of the microtubule at a secondary contact point. When the disassembling tip reaches this secondary contact point, curling protofilaments push laterally against the bead, causing it to rotate about the tether. The bead moves initially against the force of the optical trap (i.e., leftward) before the microtubule disassembles past the tether and releases the bead. The component of motion parallel to the long-axis of the microtubule (i.e., along the x-axis) is measured. The transverse component of motion (i.e., along the y- or z-axes) cannot be measured because the microtubule tip, which is unsupported, is not stiff enough to push the bead laterally against the transverse trapping forces.

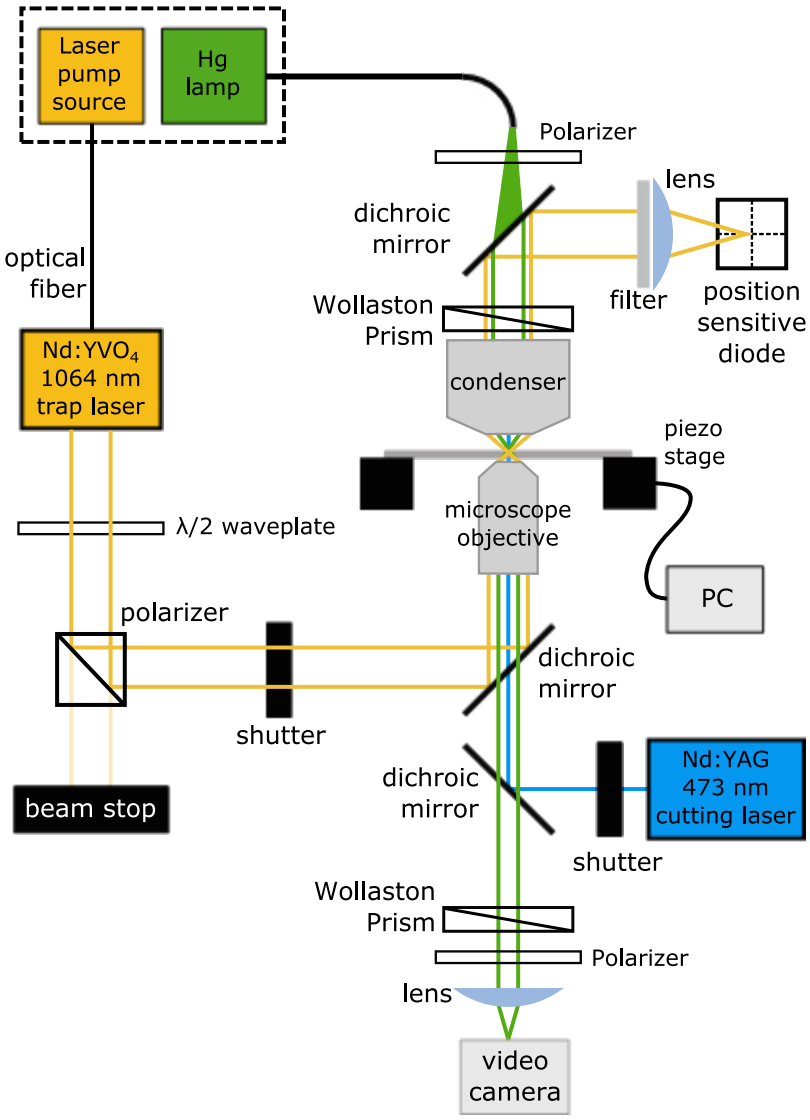

Fig 2: Overall optical layout: The laser pump source for the 1064-nm laser and mercury-arc lamp are located outside the microscope room (dashed box) to minimize heat and noise. The arc-lamp and laser pump beams are coupled to the instrument via optical fibers. The λ/2 waveplate and polarizer allow a fraction of the 1064-nm laser power to be selected for trapping. The trapping laser is actuated by an operator-controlled shutter during experiments. The trap laser enters and exits the microscope via dichroic mirrors that pass visible light. A lens projects the trapping beam through a neutral density filter onto a position sensitive diode. Trapping-beam position data is used to implement feedback by controlling the motion of the piezo specimen stage. A long-pass dichroic mirror introduces the 473-nm cutting laser into the instrument. Two Wollaston prisms and two polarizers form the DIC system. A video camera is used for contrast-enhanced DIC imaging of microtubules.

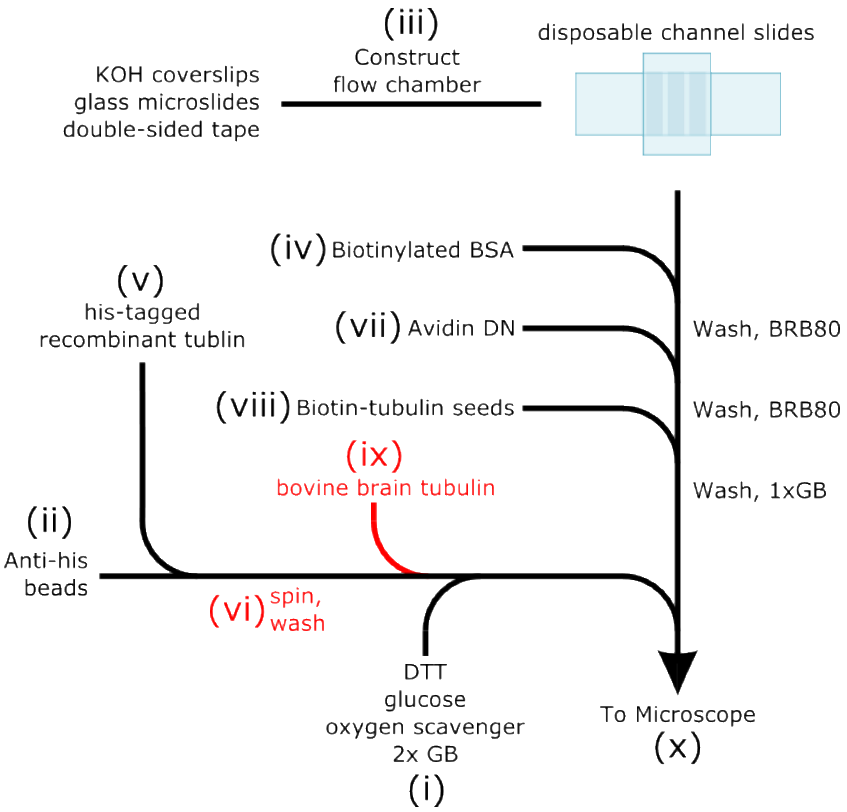

Fig 3: Order of operations for preparing coverslip-anchored microtubules with side-bound microbeads (i) Buffers and reaction mixes are prepared. (ii) Anti-His beads are passivated and washed. (iii) A disposable channel slide is constructed. (iv) Warm biotinylated BSA is added to the disposable channel slide. (v) His-tagged recombinant tubulin is clarified. (vi) (optional step for bovine brain tubulin wave assay) His-tagged, clarified yeast tubulin is incubated with anti-His beads. Subsequently these beads are washed and resuspended. (vii) BSA is washed from the disposable channel slide, and warm avidin is introduced and incubated on the slide. (viii) Avidin is washed from the disposable channel slide, and warm biotin-tubulin microtubule seeds are incubated on the slide. (ix) (optional for bovine brain tubulin wave assay) bovine tubulin is added to the reaction mix. (x) The slide is washed with 1X growth buffer (1x GB), and reaction mix containing anti-His beads decorated with recombinant tubulin, free tubulin, reducing agent, oxygen scavenger system, and GTP is added to the disposable channel slide. Subsequently the slide is sealed to prevent evaporation and mounted on the trapping microscope.

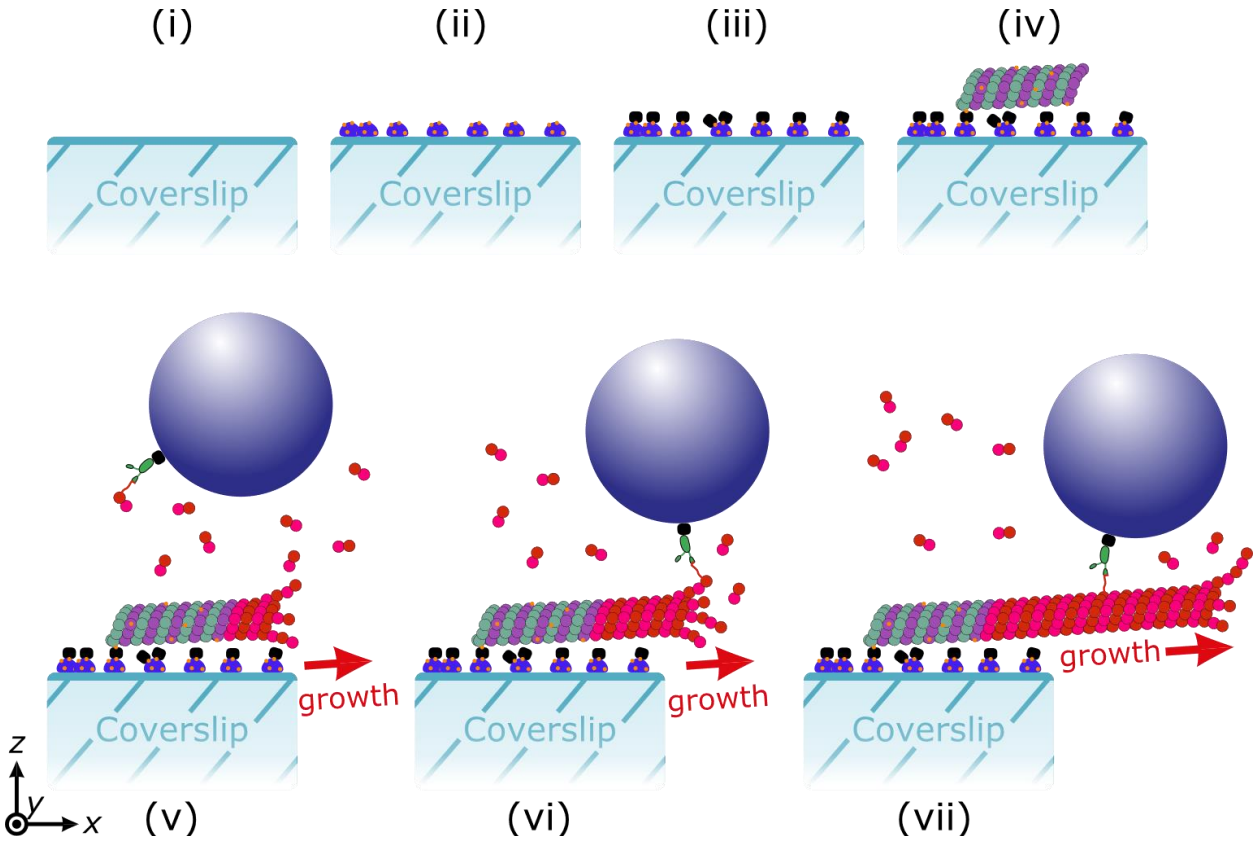

Fig 4: Tubulin-decorated beads become incorporated into growing microtubule tips: (i) A clean disposable channel slide is constructed. (ii) Biotinylated bovine serum albumin (BBSA) is flowed into the chamber, and non-specifically adsorbs to the clean surface (purple dots). (iii) Avidin DN (black squares) is flowed into the chamber and binds to BBSA already adhered to the slide surface. (iv) Biotinylated GMPCPP-stabilized short microtubules "seeds" made from bovine brain tubulin (purple and green) are flowed into the chamber and bind to the avidin DN on the surface. These seeds serve as the nucleation point for further microtubule growth. (v) A reaction mixture containing His-tagged recombinant tubulin-decorated beads (blue) and His-tagged recombinant yeast tubulin (pink and red) is flowed into the chamber. Microtubule extensions composed of recombinant yeast tubulin grow from coverslip-anchored bovine brain tubulin seeds. Streptavidin-coated microspheres are sparsely decorated with biotinylated Anti-His antibody (green), through which they bind free His-tagged recombinant yeast tubulin. (vi) Bead-bound tubulin incorporates into growing microtubules at their assembling tips. (vii) Microtubule assembly continues past the beads, converting tip-attached beads into a side-attached beads. All elements are drawn approximately to scale except the beads, which are at 1/4 relative scale to accommodate inclusion in the diagram.

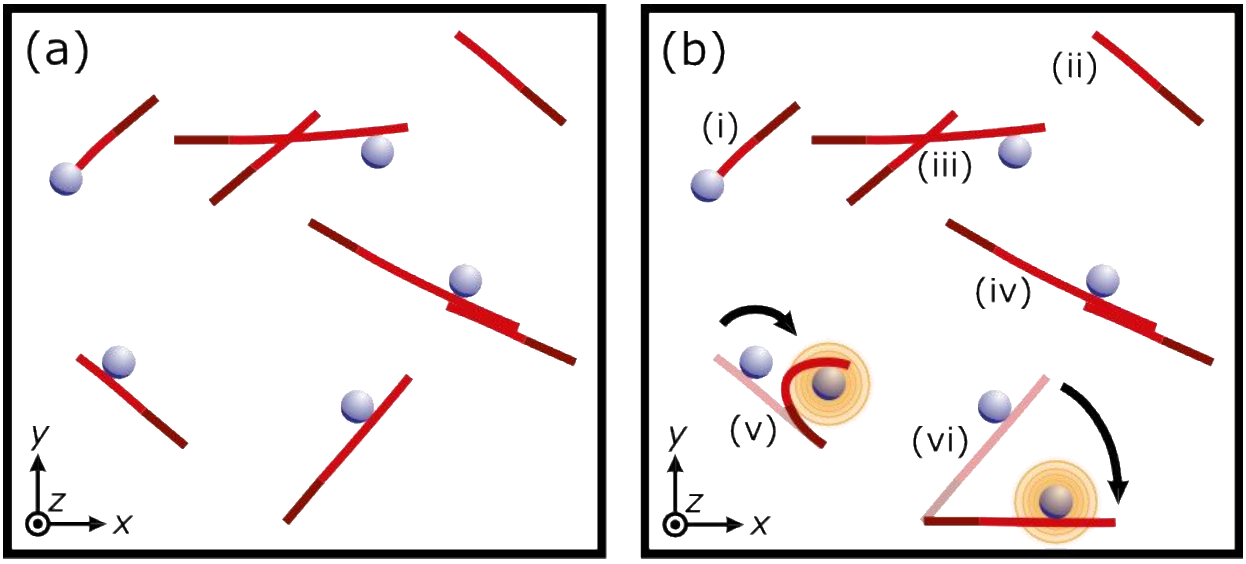

Fig. 5 - Selecting a microtubule-bead pair suitable for measurement. (a) Top-down view of a typical slide as prepared by the protocol in 3.5. Coverslip-anchored biotinylated microtubule seeds (dark red) nucleate dynamic microtubule extensions polymerized from recombinant His-tagged yeast tubulin (red). Tubulin-coated beads (blue) become incorporated into growing microtubules. (b) The measurements detailed in section 3.6 require a coverslip-anchored microtubule to have a side-attached bead, and be free from the mechanical influence of other microtubules. (i) This microtubule-bead pair has a bead end-bound to the microtubule, and is not a suitable choice for measurement. (ii) This microtubule has no attached bead. (iii) Although this microtubule does have a side-attached bead, another microtubule crosses along its length, potentially interfering with the measurements. The interfering microtubule might be carefully trimmed away using laser scissors. (iv) This microtubule-bead pair is bundled with another microtubule, preventing re-orientation. The interfering microtubule might be carefully trimmed away using laser scissors. (v) This microtubule-bead pair is properly isolated and has a suitable side-attached bead, but it is not oriented along the measurement axis (x-axis) and the seed is anchored too firmly to the coverslip, such that it cannot be reoriented by manipulation with the laser trap (orange). (vi) This isolated microtubule bead pair is anchored to the coverslip and able to be reoriented for measurement along the x-axis (motion to measurement axis is represented by black arrow). See section 3.6 for details.

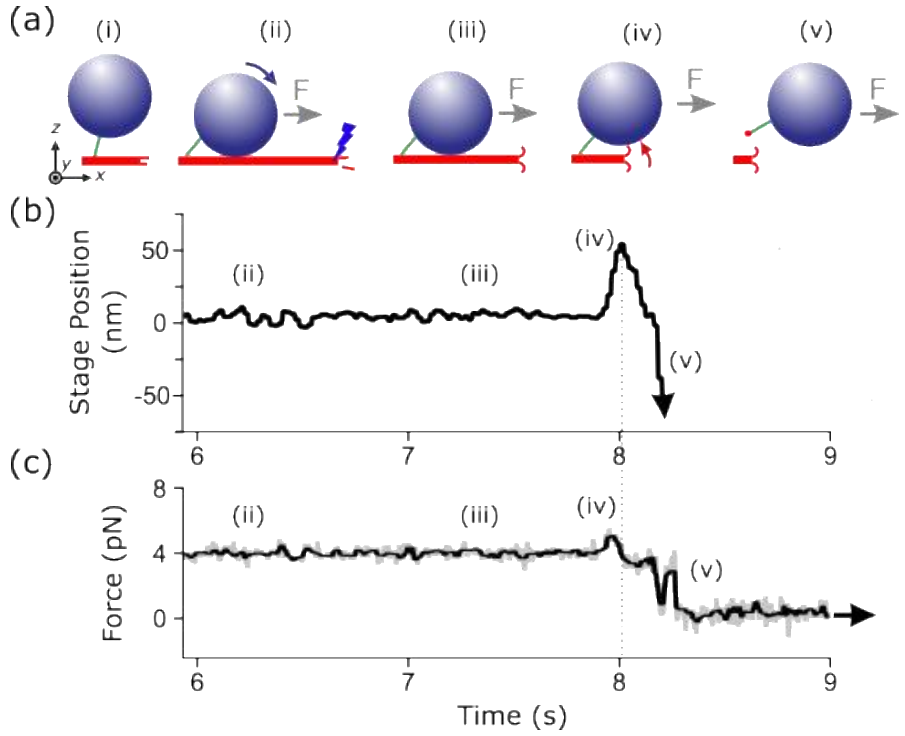

Fig 6: Measuring pulses of bead motion generated by curling protofilaments: (a) (i) Side-attached bead on a coverslip-anchored microtubule. (ii) The bead-microtubule is maneuvered to be oriented along the x-axis (the measurement axis) and is pulled opposite the direction of the coverslip-anchored seed with a force of 4 pN. This pulling force presses the bead against the body of the microtubule. Data acquisition is initiated, and the end of the microtubule is trimmed off with laser-scissors to initiate microtubule depolymerization. (iii) The microtubule depolymerizes towards the tensioned bead. (iv) When the depolymerizing microtubule tip reaches the location where the bead makes contact with the microtubule, protofilament curls push on the bead, causing it to rock back about its tether. (v) The microtubule continues to depolymerize past the bead-tether, releasing the bead from the microtubule. The force clamp program attempts to maintain the requested load force, and therefore pulls the bead rapidly away from the measurement location. (b) The stage position is plotted vs. time. All labels correspond to the events denoted in (a). The maximum of the pulse is denoted by (iv). (c) The trap force is plotted vs. time. The force clamp is able to maintain the requested 4 pN load force, even during the 130 millisecond protofilament curl-induced pulse of motion. The trap force falls to zero rapidly once the bead is completely detached from the microtubule.

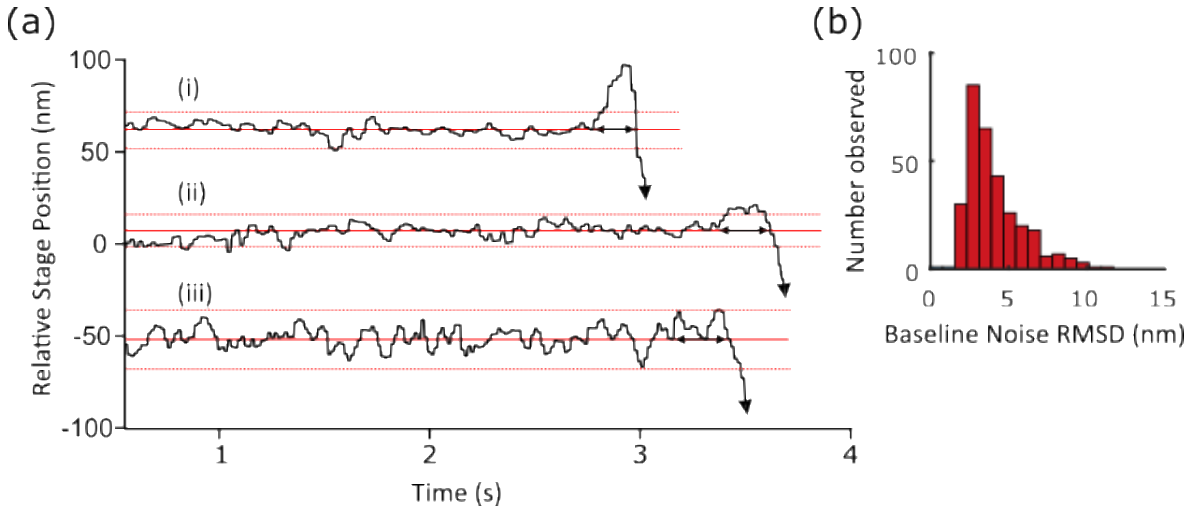

Fig 7: Distinguishing wave assay pulses from noise: (a) Plot of three relative stage position traces over time. The baseline noise is characterized by the mean position (solid red line) computed over a two second window preceding a candidate pulse. The noise magnitude is bounded well by an interval (dotted red lines) defined by ±3 times the root-mean-square-deviation (±3X RMSD) of the position signal around its baseline. Each pulse can then be parametrized by a risetime, usually between 100 and 500 milliseconds and an amplitude, typically 6 to 100 nm. (i) The first trace shows a pulse clearly distinguishable from the baseline noise, with a peak well above the 3X RMSD threshold. (ii) The second trace shows a pulse just satisfying the 3X RMSD criterion. (iii) The third pulse does not satisfy the 3X RMSD criterion, and is therefore rejected from aggregation into statistics of wave assay pulses. (b) The distribution of the baseline noise RMSD (from N=318 recorded events) shows a mode around 3 nm, with a long tail attributable to rarer high-noise traces. The distribution shows that pulses of ~10 nm are usually detectable above the 3X RMSD criterion. Because the minimum RMSD is ~2 nm, the minimum detectable pulse amplitude is ~6 nm. There may be conditions where many pulse amplitudes are measured close to the baseline noise. In this case, smaller pulses are likely to be erroneously rejected, skewing the mean pulse amplitude towards a higher value. In this case, the median or mode are better summary statistics. Small pulses, with amplitudes below 10 nm, are therefore likely to be missed, potentially skewing the mean pulse amplitude towards a higher value. In cases where a large fraction of events fail to produce detectable pulses, or where the pulse amplitudes are very close to the detection threshold, the median or mode might be better summary statistics.

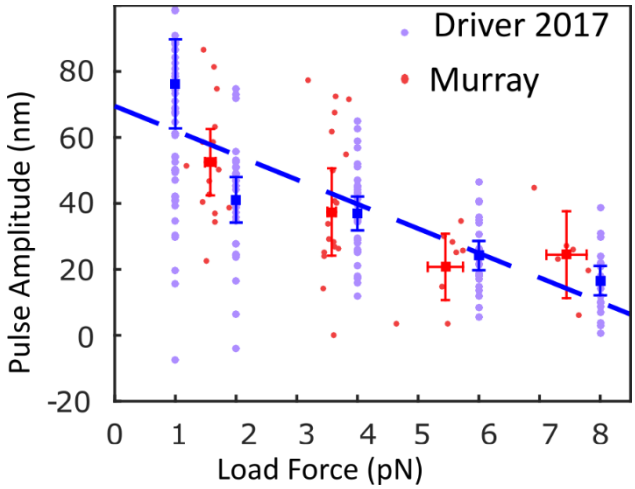

Figure 8: Protofilament curls are spring-like and release a substantial amount of mechanical energy during microtubule disassembly: Pulse amplitude plotted vs. load force applied. Data are plotted as individual puleses (small dots), and means for each load force (squares). Error bars represent a 95% CI (Student's t). Data reported previously [1], is plotted in blue. New data recorded independently and reproducing the same trend is plotted in red. Force suppresses pulse amplitudes, indicating that protofilaments are spring-like. The area under the fit line estimates the substantial work done by curling protofilaments on the bead (~300 pN·nm).

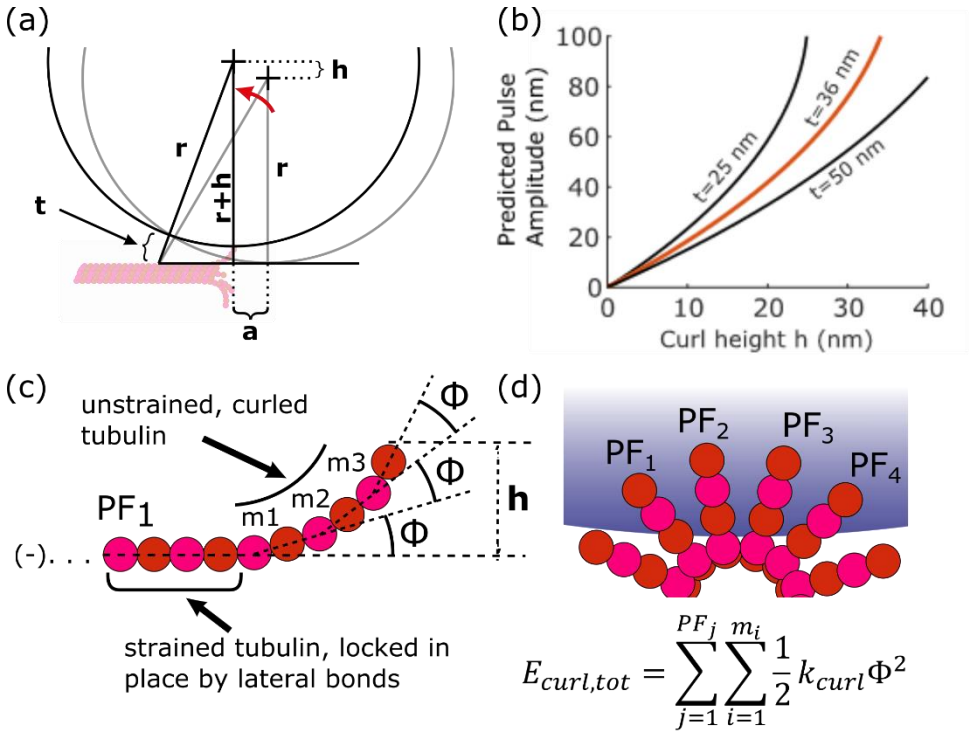

Fig 9: Leverage in the wave assay and how curl properties can be related to measured wave energies (a) The arrangement of the bead and its engineered tether creates a mechanical lever system that modestly amplifies the motion of the curling protofilaments. The relationship between the measured pulse amplitude, *a*, and the protofilament curl height, *h*, depends on the tether length, *t*, and the bead radius, *r*. (b) The predicted *a*-vs-*h* relationship for tether lengths of 25, 36, and 50 nm and a bead radius of 220 nm. For a 36-nm tether (as we calculate is used in our assay), protofilament curl motions are amplified between 2 and 2.5-fold. For all tether lengths, the *a*-vs-*h* relationship is approximately linear until the curl height approaches the tether length, at which point significant non-linearities arise. (c) Parameterization of protofilament curl morphology. Protofilament height *h* is a function of the number of tubulin dimers in the protofilament (contour length) and the mean angle per dimer Φ. The morphological parameters can be estimated from cryo-electron micrographs and tomograms of disassembling microtubule tips [2-4]. (d) End-view of a disassembling microtubule tip, indicating that up to four protofilaments could push on a tethered bead. The equation below relates curl energy to protofilament morphological parameters and the mean stiffness per dimer, k_{curl}.

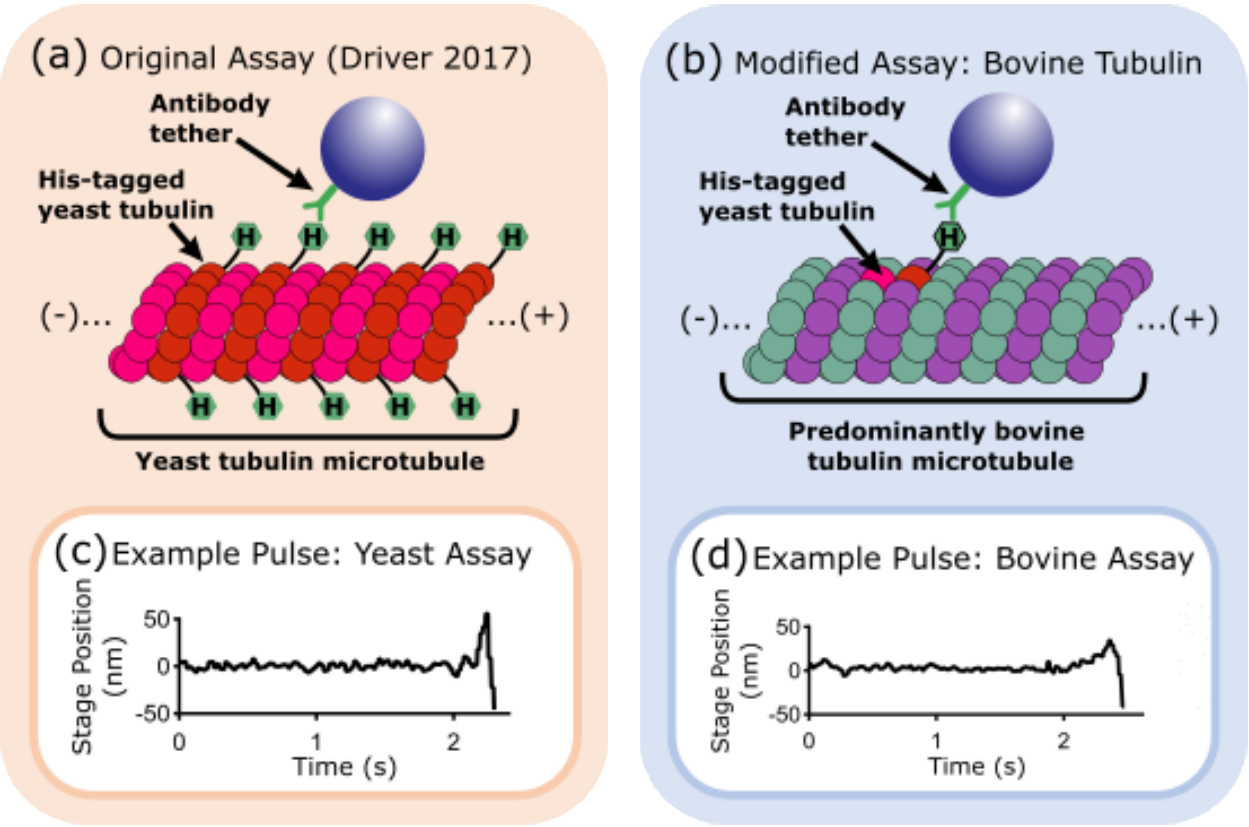

Figure 10: Comparison of wave assay and modifications to allow pulses to be measured from native bovine brain tubulin. (a) Anti-penta-His antibody decorated beads bind recombinant his-tagged yeast tubulin. The tubulin-decorated beads become incorporated into microtubules composed of recombinant yeast tubulin. (b) Anti-penta-His antibody decorated beads are first incubated with His-tagged yeast tubulin before mixing with tubulin purified from bovine brain. The yeast tubulin-coated beads incorporate into growing microtubules composed primarily of native bovine brain tubulin. (c) Pulse from yeast tubulin-only assay. (d) Pulse from bovine tubulin assay, often smaller than those observed in the yeast tubulin assay.

Bibliography

1. Driver JW, Geyer EA, Bailey ME, Rice LM, Asbury CL (2017) Direct measurement of conformational strain energy in protofilaments curling outward from disassembling microtubule tips. eLife 6:18. doi:10.7554/eLife.28433
2. McIntosh JR, Grishchuk EL, Morphew MK, Efremov AK, Zhudenkov K, Volkov VA, Cheeseman IM, Desai A, Mastronarde DN, Ataullakhanov FI (2008) Fibrils Connect Microtubule Tips with Kinetochores: A Mechanism to Couple Tubulin Dynamics to Chromosome Motion. Cell 135 (2):322-333. doi:10.1016/j.cell.2008.08.038
3. McIntosh JR, O'Toole E, Morgan G, Austin J, Ulyanov E, Ataullakhanov F, Gudimchuk N (2018) Microtubules grow by the addition of bent guanosine triphosphate tubulin to the tips of curved protofilaments. J Cell Biol 217 (8):2691-2708. doi:10.1083/jcb.201802138
4. O'Toole E, Morphew M, McIntosh JR (2020) Electron tomography reveals aspects of spindle structure important for mechanical stability at metaphase. Mol Biol Cell 31 (3):184-195. doi:10.1091/mbc.E19-07-0405
5. Ashkin A, Dziedzic JM, Bjorkholm JE, Chu S (1986) OBSERVATION OF A SINGLE-BEAM GRADIENT FORCE OPTICAL TRAP FOR DIELECTRIC PARTICLES. Opt Lett 11 (5):288-290. doi:10.1364/ol.11.000288
6. Nicholas MP, Rao L, Gennerich A (2014) An Improved Optical Tweezers Assay for Measuring the Force Generation of Single Kinesin Molecules. Mitosis: Methods and Protocols 1136:171-246. doi:10.1007/978-1-4939-0329-0_10
7. Korten T, Nitzsche B, Gell C, Ruhnow F, Leduc C, Diez S (2011) Fluorescence Imaging of Single Kinesin Motors on Immobilized Microtubules. Single Molecule Analysis: Methods and Protocols 783:121-137. doi:10.1007/978-1-61779-282-3_7
8. Lang MJ, Asbury CL, Shaevitz JW, Block SM (2002) An automated two-dimensional optical force clamp for single molecule studies. Biophysical Journal 83 (1):491-501. doi:10.1016/s0006-3495(02)75185-0
9. Gennerich A, Carter AP, Reck-Peterson SL, Vale RD (2007) Force-induced bidirectional stepping of cytoplasmic dynein. Cell 131 (5):952-965. doi:10.1016/j.cell.2007.10.016
10. Sommese RF, Sung J, Nag S, Sutton S, Deacon JC, Choe E, Leinwand LA, Ruppel K, Spudich JA (2013) Molecular consequences of the R453C hypertrophic cardiomyopathy mutation on human beta-cardiac myosin motor function. Proc Natl Acad Sci U S A 110 (31):12607-12612. doi:10.1073/pnas.1309493110
11. Ketelaar T, van der Honing HS, Emons AMC (2010) Probing cytoplasmic organization and the actin cytoskeleton of plant cells with optical tweezers. Biochem Soc Trans 38:823-828. doi:10.1042/bst0380823
12. Vanzi F, Capitanio M, Sacconi L, Stringari C, Cicchi R, Canepari M, Maffei M, Piroddi N, Poggesi C, Nucciotti V, Linari M, Piazzesi G, Tesi C, Antolini R, Lombardi V, Bottinelli R, Pavone FS (2006) New techniques in linear and non-linear laser optics in muscle research. J Muscle Res Cell Motil 27 (5-7):469-479. doi:10.1007/s10974-006-9084-3
13. Wang MD, Schnitzer MJ, Yin H, Landick R, Gelles J, Block SM (1998) Force and velocity measured for single molecules of RNA polymerase. Science 282 (5390):902-907. doi:10.1126/science.282.5390.902
14. Abbondanzieri EA, Greenleaf WJ, Shaevitz JW, Landick R, Block SM (2005) Direct observation of base-pair stepping by RNA polymerase. Nature 438 (7067):460-465. doi:10.1038/nature04268
15. Smith DE, Tans SJ, Smith SB, Grimes S, Anderson DL, Bustamante C (2001) The bacteriophage phi 29 portal motor can package DNA against a large internal force. Nature 413 (6857):748-752. doi:10.1038/35099581
16. Aubin-Tam M-E, Olivares AO, Sauer RT, Baker TA, Lang MJ (2011) Single-Molecule Protein Unfolding and Translocation by an ATP-Fueled Proteolytic Machine. Cell 145 (2):257-267. doi:10.1016/j.cell.2011.03.036

17. Gore J, Bryant Z, Stone MD, Nollmann MN, Cozzarelli NR, Bustamante C (2006) Mechanochemical analysis of DNA gyrase using rotor bead tracking. Nature 439 (7072):100-104. doi:10.1038/nature04319
18. Koshland DE, Mitchison TJ, Kirschner MW (1988) POLEWARDS CHROMOSOME MOVEMENT DRIVEN BY MICROTUBULE DEPOLYMERIZATION INVITRO. Nature 331 (6156):499-504. doi:10.1038/331499a0
19. Lombillo VA, Stewart RJ, McIntosh JR (1995) MINUS-END-DIRECTED MOTION OF KINESIN-COATED MICROSPHERES DRIVEN BY MICROTUBULE DEPOLYMERIZATION. Nature 373 (6510):161-164. doi:10.1038/373161a0
20. Inoue S, Salmon ED (1995) FORCE GENERATION BY MICROTUBULE ASSEMBLY DISASSEMBLY IN MITOSIS AND RELATED MOVEMENTS. Mol Biol Cell 6 (12):1619-1640
21. Dogterom M, Yurke B (1997) Measurement of the force-velocity relation for growing microtubules. Science 278 (5339):856-860. doi:10.1126/science.278.5339.856
22. Kerssemakers JWJ, Munteanu EL, Laan L, Noetzel TL, Janson ME, Dogterom M (2006) Assembly dynamics of microtubules at molecular resolution. Nature 442 (7103):709-712. doi:10.1038/nature04928
23. Cameron LA, Footer MJ, van Oudenaarden A, Theriot JA (1999) Motility of ActA protein-coated microspheres driven by actin polymerization. Proc Natl Acad Sci U S A 96 (9):4908-4913. doi:10.1073/pnas.96.9.4908
24. Footer MJ, Kerssemakers JWJ, Theriot JA, Dogterom M (2007) Direct measurement of force generation by actin filament polymerization using an optical trap. Proc Natl Acad Sci U S A 104 (7):2181-2186. doi:10.1073/pnas.0607052104
25. Bieling P, Li TD, Weichsel J, McGorty R, Jreij P, Huang B, Fletcher DA, Mullins RD (2016) Force Feedback Controls Motor Activity and Mechanical Properties of Self-Assembling Branched Actin Networks. Cell 164 (1-2):115-127. doi:10.1016/j.cell.2015.11.057
26. Aldaz H, Rice LM, Stearns T, Agard DA (2005) Insights into microtubule nucleation from the crystal structure of human gamma-tubulin. Nature 435 (7041):523-527. doi:10.1038/nature03586
27. Brouhard GJ, Rice LM (2014) The contribution of alpha beta-tubulin curvature to microtubule dynamics. J Cell Biol 207 (3):323-334. doi:10.1083/jcb.201407095
28. Desai A, Mitchison TJ (1997) Microtubule polymerization dynamics. Annu Rev Cell Dev Biol 13:83-117. doi:10.1146/annurev.cellbio.13.1.83
29. Caplow M, Shanks J (1996) Evidence that a single monolayer tubulin-GTP cap is both necessary and sufficient to stabilize microtubules. Mol Biol Cell 7 (4):663-675. doi:10.1091/mbc.7.4.663
30. Mickey B, Howard J (1995) RIGIDITY OF MICROTUBULES IS INCREASED BY STABILIZING AGENTS. J Cell Biol 130 (4):909-917. doi:10.1083/jcb.130.4.909
31. MacIntosh JR (2017) Mechanisms of mitotic chromosome segregation. MDPI, Basel
32. Koshland DE, Goldbeter A, Stock JB (1982) AMPLIFICATION AND ADAPTATION IN REGULATORY AND SENSORY SYSTEMS. Science 217 (4556):220-225. doi:10.1126/science.7089556
33. Asbury CL, Tien JF, Davis TN (2011) Kinetochores' gripping feat: conformational wave or biased diffusion? Trends Cell Biol 21 (1):38-46. doi:10.1016/j.tcb.2010.09.003
34. Hill TL (1985) THEORETICAL PROBLEMS RELATED TO THE ATTACHMENT OF MICROTUBULES TO KINETOCHORES. Proc Natl Acad Sci U S A 82 (13):4404-4408. doi:10.1073/pnas.82.13.4404
35. Grishchuk EL, Molodtsov MI, Ataullakhanov FI, McIntosh JR (2005) Force production by disassembling microtubules. Nature 438 (7066):384-388. doi:10.1038/nature04132
36. Franck AD, Powers AF, Gestaut DR, Davis TN, Asbury CL (2010) Direct physical study of kinetochore-microtubule interactions by reconstitution and interrogation with an optical force clamp. Methods 51 (2):242-250. doi:10.1016/j.ymeth.2010.01.020
37. Johnson V, Ayaz P, Huddleston P, Rice LM (2011) Design, Overexpression, and Purification of Polymerization-Blocked Yeast alpha beta-Tubulin Mutants. Biochemistry 50 (40):8636-8644. doi:10.1021/bi2005174

38. Geyer EA, Burns A, Lalonde BA, Ye XC, Piedra FA, Huffaker TC, Rice LM (2015) A mutation uncouples the tubulin conformational and GTPase cycles, revealing allosteric control of microtubule dynamics. eLife 4:20. doi:10.7554/eLife.10113
39. Castoldi M, Popova AV (2003) Purification of brain tubulin through two cycles of polymerization-depolymerization in a high-molarity buffer. Protein Expr Purif 32 (1):83-88. doi:10.1016/s1046-5928(03)00218-3
40. Mandelkow EM, Mandelkow E, Milligan RA (1991) MICROTUBULE DYNAMICS AND MICROTUBULE CAPS - A TIME-RESOLVED CRYOELECTRON MICROSCOPY STUDY. J Cell Biol 114 (5):977-991. doi:10.1083/jcb.114.5.977
41. McIntosh JR, O'Toole E, Zhudenkov K, Morphew M, Schwartz C, Ataullakhanov FI, Grishchuk EL (2013) Conserved and divergent features of kinetochores and spindle microtubule ends from five species. J Cell Biol 200 (4):459-474. doi:10.1083/jcb.201209154

Chapter 3

Working strokes produced by curling protofilaments at disassembling microtubule tips can be biochemically tuned and vary with species

Originally published in eLife, vol. 11 (2022), e83225

Abstract

The disassembly of microtubules can generate force and drive intracellular motility. During mitosis, for example, chromosomes remain persistently attached via kinetochores to the tips of disassembling microtubules, which pull the sister chromatids apart. According to the conformational wave hypothesis, such force generation requires that protofilaments curl outward from the disassembling tips to exert pulling force directly on kinetochores. Rigorously testing this idea will require modifying the mechanical and energetic properties of curling protofilaments, but no way to do so has yet been described. Here, by direct measurement of working strokes generated in vitro by curling protofilaments, we show that their mechanical energy output can be increased by adding magnesium, and that yeast microtubules generate larger and more energetic working strokes than bovine microtubules. Both the magnesium and species-dependent increases in work output can be explained by lengthening the protofilament curls, without any change in their bending stiffness or intrinsic curvature. These observations demonstrate how work output from curling protofilaments can be tuned and suggest evolutionary conservation of the amount of curvature strain energy stored in the microtubule lattice.

Introduction

Microtubules are filamentous polymers central to the active transport of cargoes in cells. While they often serve as passive tracks along which dynein and kinesin motors move, these filaments can also drive motility directly. Dynamic microtubules in the mitotic spindle transport chromosomes during cell division by shortening while their disassembling tips remain coupled via kinetochores to the chromosomes [1-3]. Dynamic microtubules also generate force to properly position the mitotic spindle and the nucleus within cells [3-7]. These microtubule-driven movements are powered by GTP hydrolysis. GTP is incorporated into the assembling polymer tip and then hydrolyzed, depositing energy into the GDP-tubulin lattice. The stored lattice energy is released during disassembly and can be harnessed to generate pulling force. Thus microtubules, like dynein and kinesin motors, convert chemical energy into mechanical work [3]. How they do so remains poorly understood.

Two distinct classes of mechanism could explain how disassembling microtubule tips generate pulling force: the biased diffusion and conformational wave mechanisms [8]. According to biased diffusion-based models, a tip-coupler such as the kinetochore undergoes a thermally driven random walk along the microtubule surface that is biased at the tip, due to the affinity of the coupler for the microtubule. If the affinity of the coupler for the microtubule is sufficiently high and if its diffusion is sufficiently fast, then the coupler can remain persistently associated with the disassembling tip, where it will experience a thermodynamic force in the direction of disassembly [9]. The effect is analogous to capillary action that pulls fluids into narrow channels. Biased diffusion of a key kinetochore element, the Ndc80 complex, has been observed directly on microtubules in vitro [10].

By contrast, force generation in conformational wave-based models depends on structural changes at disassembling microtubule tips. During disassembly, individual rows of tubulin dimers called protofilaments curl outward from the tip before breaking apart, creating a wave of conformational change that propagates down the long axis of the microtubule [11, 12]. These curling protofilaments are proposed to physically hook the kinetochore and pull against it to drive motility [13]. Prior work showed

that the amount of mechanical strain energy released by curling protofilaments is more than sufficient to account for kinetochore motility [14]. However, whether kinetochores specifically harness any of this strain energy remains unclear, owing in part to the lack of methods for modifying mechanical or energetic properties of protofilament curls.

Many prior studies have established that added magnesium profoundly affects the dynamics of microtubules in vitro, altering the rates of switching between tip growth and shortening [15], accelerating tip disassembly [16], and lengthening the protofilament curls at disassembling tips [17]. Binding of magnesium to acidic residues in the disordered C-terminal tail of tubulin is implicated in magnesium-dependent acceleration of disassembly [18-21]. Faster disassembly by itself might explain why magnesium also lengthens protofilament curls, because it implies a faster rate of curling (i.e. that GDP-tubulins are losing their lateral bonds and curling outward more quickly; [22]). However, magnesium might also stabilize the longitudinal bonds within protofilament curls, thereby reducing the rate at which the curls break. To disentangle magnesium's effects on curling and breakage rates, a systematic examination of curl contour length as a function of disassembly speed is required.

Previously, we developed an assay for measuring forces and displacements generated by curling protofilaments [14] based on earlier pioneering work [23]. In our 'wave' assay, the curling protofilaments push laterally against a microbead tethered to the microtubule wall, thereby generating a brief pulse of bead motion against the force of a feedback-controlled laser trap. We show here that the sizes of these pulses – and the mechanical work energy that can be harnessed from them – are substantially increased by the addition of millimolar levels of magnesium. By measuring wave pulses after proteolytic cleavage of the β-tubulin C-terminal tail, we show that magnesium enlarges the pulses independently of its acceleration of disassembly, indicating that magnesium directly stabilizes the longitudinal bonds within protofilament curls. We also demonstrate that pulses generated by yeast tubulin are larger than those generated by bovine brain tubulin. A simple mechanical model shows that both the magnesium- and species-dependent changes in pulse energy can be explained solely by increasing the contour lengths of protofilament curls, without changing their intrinsic flexural rigidity or curvature. The conservation of protofilament flexural rigidity and stored lattice strain suggest that these biophysical properties are crucial to microtubule function in cells.

Results

Measuring outward curling of protofilaments from bovine brain microtubules

We previously measured the mechanical and energetic properties of protofilaments as they curled outward from recombinant yeast-tubulin microtubules [14]. In our wave assay, a laser trap applies force against the curling protofilaments, via beads tethered to the microtubule lattice through a single His6 tag on the C-terminus of β-tubulin [24]. Linkage through a single β-tubulin C-terminal tail creates a strong, flexible tether approximately 36 nm in length, which probably helps to avoid interference between the tethered bead and the curling protofilaments [14]. To extend our approach to untagged mammalian brain tubulin, we modified the assay by introducing anti-His beads pre-decorated sparsely with the recombinant His6-tagged yeast tubulin into chambers containing coverslip-anchored microtubules growing from free bovine brain tubulin. The decoration density of yeast tubulin on the beads was kept very low, around one tubulin per bead, by limiting the amount of anti-His antibody on the beads (see Materials and methods). The bead-linked yeast tubulin was incorporated into the assembling bovine microtubules, resulting in beads tethered to the sides of the filaments ([25]; Figure 1a). As in our previous work [14], the low density of antibody on the beads ensured that most beads were tethered by a single antibody. Continuous tension, directed toward the plus end, was applied to a microtubule-

tethered bead using feedback control. The tension pressed the bead against the microtubule lattice at a secondary contact point and suppressed Brownian motion, which facilitated tracking the bead with high spatiotemporal resolution. The microtubule plus end was then severed with laser scissors to induce disassembly [26]. As the disassembling tip passed the secondary contact point, protofilament curls pushed laterally on the bead, causing it to rotate about its tether. This rotation produced a brief (100–400 ms) pulse of bead movement against the force of the laser trap, which was followed by bead detachment after further disassembly released the tether (Figure 1b). The pulses were parameterized by their amplitude relative to the baseline bead position (Figure 1—figure supplement 1), which is directly related to the lateral height that the protofilament curls project from the surface of the microtubule lattice (Figure 1—figure supplement 2) [14].

At 2 pN of trapping force, 59% of disassembly events yielded measurable pulses, with a mean amplitude of 19.2±2.7 nm. At higher forces, pulse amplitudes became smaller (Figure 1b), consistent with spring-like elasticity of the curling protofilaments, as we previously observed for yeast tubulin protofilament curls [14]. Pulse amplitudes generated by bovine microtubules were smaller than those we measured previously from yeast microtubules at identical force levels (e.g. 19.2±2.7 vs 51±7 nm on average at 2 pN [27]. This observation suggests that bovine protofilament curls might be shorter than yeast curls, consistent with reports that disassembly products released from mammalian brain microtubules are shorter than their yeast-derived counterparts [28]. Nevertheless, our findings confirm that pulses from bovine microtubules can be reliably measured using our modified wave assay.

Adding magnesium enlarges the pulses generated by curling protofilaments

Divalent cations have long been known to affect tubulin self-association [21, 29, 30] and influence microtubule dynamics [21, 31]. These effects occur partly through interactions of magnesium ions with the unstructured C-terminal tails of tubulin [18, 32] and with the exchangeable and non-exchangeable nucleotide binding sites [33]. Early cryo-electron microscopy of disassembling microtubules showed that magnesium lengthens protofilament curls at disassembling tips [17]. Based on these prior observations, we predicted that pulses recorded in our wave assay might become larger and more energetic with added magnesium.

As previously observed [18], we found that adding magnesium accelerated the disassembly of bovine brain tubulin microtubules, increasing their shortening speeds by about threefold, from 380±36 $nm \cdot s^{-1}$ at our initial level of 1 mM magnesium to 1200±40 $nm \cdot s^{-1}$ at 20 mM magnesium (Figure 2a and b). Consistent with our prediction, adding magnesium also increased the amplitudes of pulses measured in the wave assay (Figure 2c). At 2 pN of trapping force, the mean amplitude increased by 50% from 19.2±2.7 nm at 1 mM magnesium up to 29.1±2.8 nm at 20 mM magnesium (Figure 2d). This magnesium-dependent increase in pulse amplitude might be explained simply by lengthening the protofilament curls, as suggested by early cryo-electron microscopy studies. However, it might also reflect increases in the mechanical stiffness or curvature of the protofilaments, or in the number of protofilaments that push against the bead in the wave assay (as discussed below).

Adding magnesium increases work output from protofilament curls

To determine whether adding magnesium affects the mechanochemical work output from curling protofilaments, we measured pulse amplitudes across a variety of trapping forces and magnesium concentrations (Figure 3 and Figure 3—figure supplement 1). Measuring pulse amplitude as a function of force enables estimation of the total capacity for mechanical work output in the assay, which is given by the area under the amplitude vs force curve (Figure 3a; [14]). Based on a line fit to the data, we estimated work output from the bovine brain microtubules in 1 mM magnesium at 107±69 pN·nm (Figure 3b). Adding magnesium increased the work output monotonically, raising it to 177±0.1 pN·nm at 20 mM magnesium (Figure 3b). This magnesium-induced increase was mainly due to enlargement of the pulses measured at low trapping force; extrapolating the line fits to zero force suggested that the unloaded pulse amplitude (i.e. the amplitude that would be measured in the absence of opposing trap force) increased 57% from 23.3±0.9 nm at 1 mM magnesium to 36.6±0.1 nm at 20 mM magnesium (Figure 3c). By contrast, extrapolating the linear fits to higher forces suggested relatively little change in the maximum force at which the pulses were completely suppressed (~9 pN) (Figure 3a). Altogether, these observations show that magnesium increases mechanical work output from curling protofilaments while also increasing the lateral height that they project from the microtubule wall.

Notably, the mechanical work output from bovine microtubules was about threefold less than we measured previously from microtubules composed entirely of recombinant yeast tubulin under similar conditions (~300 pN·nm at 1 mM magnesium) [14]. This difference, like magnesium-dependent differences, could reflect altered contour lengths, bending stiffnesses, average curvatures, numbers of curling protofilaments pushing on the beads, or a combination thereof.

Curl elongation alone explains the magnesium-dependent increase in work output

To develop a deeper understanding of how magnesium increases the mechanical work output from curling protofilaments, we created a simple model of protofilament bending. The model relates structural aspects of protofilament curls, such as their relaxed curvature and the average number of dimers they contain, together with an estimate of their flexural rigidity, to predict the force-deflection behavior of a group of curls projecting radially outward from a microtubule tip. In real protofilaments, elastic bending energy can be distributed throughout the α- and β-tubulin core structures, as well as at both the inter- and intra-dimer interfaces. Rather than modeling this complexity, we placed all the compliance of the model into single bending springs located at the inter-dimer interfaces (Figure 4a). This simplification was important for our analyses, because it allowed data-fitting to provide good constraints on the model parameter values. (A model with more parameters would fit the data just as well or better but would not allow meaningful estimation of parameter values, due to degeneracy.) And while our model cannot address in detail how strain might be distributed across the inter- and intra-dimer interfaces (nor across the α- and β-tubulin core structures), it can describe the overall force-deflection behavior of protofilament curls, and it provides a simple way to estimate stored strain per dimer. In essence, our model convolves all the potential contributions to elastic bending strain together into a single element (an inter-dimer spring) that provides an effective flexural rigidity per dimer.

Contour shapes for the individual protofilaments were solved by balancing the external force applied at their tips with the opposing bending spring torques at each inter-dimer node (Figure 4b, left). To model the force-deflection behavior of a group of protofilaments, single protofilaments were arranged radially, according to a 13-protofilament geometry (Figure 4b, right) [34]. The bead was modeled as a rigid, flat surface since its curvature is negligible compared to that of the microtubule tip. Prior cryo-electron tomography studies of disassembling microtubules found almost all the variation in protofilament shape to occur in the radial direction (i.e. within a plane coincident with both the relaxed

contour and the long axis of the microtubule [35]. Therefore, protofilament bending in our model was limited to the radial direction. Given these assumptions, deflection of individual protofilaments varied according to their orientation relative to the bead surface (Figure 4b, right). A detailed analysis of changes in the force-deflection profile that occur with respect to changes in the average curvature, average dimers per curl, and flexural rigidity is shown in the supplemental material (Figure 4—figure supplement 1).

To fit the behavior of this multi-protofilament model to the measured pulse amplitude versus force data at each magnesium concentration, we adjusted the average number of dimers in each curl (i.e. the curl contour length) and the stiffness of the bending springs. We kept the relaxed angle per dimer fixed at 23° because, in the absence of microtubule-associated proteins, the curvature of protofilaments at microtubule tips disassembling in vitro is consistently between 20 and 25° per dimer (Figure 4—source data 2), and this curvature does not change appreciably with added magnesium (Figure 4—figure supplement 2;[17]) (nor with added calcium, [36]). Because the bead acts as a lever, measured axial displacements of the bead are larger than the lateral deflections of the protofilaments by a leverage factor of approximately twofold (Figure 1—figure supplement 2; [14]). Predicted amplitude vs force curves were roughly linear, but with slight 'ripples' that occurred because movement of the bead toward the microtubule gradually engaged more protofilaments (Figure 4c; Figure 4—figure supplement 3; see Materials and methods for details). Optimal fit parameters are plotted as functions of magnesium in Figure 4d.

The fitted contour lengths of protofilaments increased monotonically with added magnesium, from 2.3±0.5 dimers at 1 mM magnesium to 3.2±0.2 dimers at 20 mM. However, the fitted bending stiffness per dimer, 176±15 pN·nm·rad^{-1}, did not appreciably change with added magnesium (Figure 4d). These results suggest that magnesium increases pulse amplitude and work output by lengthening the protofilament curls, without eliciting any change in their intrinsic stiffness or curvature.

Curl elongation alone explains the larger pulses from yeast microtubules

To understand why yeast microtubules generated larger, more energetic pulses relative to bovine microtubules, we fit our multi-protofilament model to the amplitude versus force data measured from microtubules composed entirely of recombinant yeast tubulin (Figure 4c). As in our analysis of the bovine microtubule data, we allowed both the curl contour length and the stiffness of the bending springs to vary while keeping the relaxed angle per dimer fixed at 23°, consistent with cryo-electron tomograms of kinetochore microtubules in yeast [35]. The contour length that best fit the yeast data, 4.4±0.5 dimers per curl, was 1.9-fold higher than the contour length inferred at identical magnesium concentration (1 mM) from the bovine data, 2.3±0.5 dimers per curl (Figure 4d). The bending stiffness per dimer that best fit the yeast data, 206±44 pN·nm·rad^{-1}, was statistically indistinguishable from that inferred from the bovine data (Figure 4d). These observations suggest that protofilament curls at yeast microtubule tips are longer but have the same intrinsic mechanical rigidity as the curls at bovine microtubule tips.

Removing the β-tubulin tail suppresses magnesium's enhancement of disassembly speed but not of pulse amplitude

Prior studies have suggested that longer protofilament curls might arise simply as a consequence of faster disassembly speeds [22]. Consistent with this view, when we increased magnesium from 1 to 20 mM, we observed a threefold increase in disassembly speed (Figure 2b) concomitant with a 1.6-fold increase in pulse amplitude (Figures 2d and 4c). Likewise, yeast microtubules disassembled fourfold faster than bovine microtubules at 1 mM magnesium (Figure 4—figure supplement 4) and generated threefold larger pulses (Figure 4c). Faster disassembly speeds imply that

GDP-tubulins lose their lateral bonds more quickly, which equivalently can be viewed as an accelerated rate of growth of the protofilament curls at disassembling tips. However, curl size is dictated not only by curl growth but also by curl breakage; the mean steady state curl length will depend on a kinetic balance between the rates of curling and breakage [22]. In principle, both these rates could vary in a magnesium-dependent manner. To distinguish the potential influence of magnesium on curl breakage from its obvious effect on disassembly speed (and therefore on curl growth rate), we sought a method to slow bovine microtubule disassembly at elevated levels of magnesium. A recent discovery pointed to one such method. Fees and Moore found that removing the β-tubulin C-terminal tail, by treating microtubules with the protease subtilisin, suppresses the effect of magnesium on disassembly speed [18]. Thus, at high magnesium concentration, subtilisin-treated microtubules disassemble much more slowly than untreated microtubules. If magnesium lengthens protofilament curls solely because it accelerates disassembly, then subtilisin treatment should suppress the magnesium-dependent enlargement of pulses in the wave assay.

Contrary to this prediction, however, subtilisin treatment did not reduce pulse amplitudes in the wave assay. Consistent with the prior work of Fees and Moore, we found that subtilisin treatment for 10–20 min was sufficient to remove the β-tubulin C-terminal tail (Figure 5a) and to suppress almost completely the magnesium-dependent acceleration of disassembly (Figure 5b). While disassembly of untreated control microtubules was strongly accelerated, from 380±36 to 1200±40 $nm \cdot s^{-1}$, when magnesium was increased from 1 to 20 mM, the disassembly after 10 or more minutes of subtilisin treatment was consistently slower and remained at approximately 300 $nm \cdot s^{-1}$ across the same range of magnesium levels (e.g. 333±24 $nm \cdot s^{-1}$ at 20 mM magnesium). Despite this strikingly slower disassembly, the mean pulse amplitude measured in the wave assay after subtilisin treatment remained at least as large as that measured in controls with untreated tubulin (Figure 5c). At 20 mM magnesium, the mean pulse amplitude generated after 5 and 10 min of subtilisin treatment was 30.7±8.3 and 38.5±9.4 nm (respectively), a size very similar to (or even slightly larger than) the mean amplitude generated by untreated microtubules, which was 29.1±2.8 nm. This observation indicates that magnesium enlarges protofilament curls independently of its acceleration of disassembly and suggests that distinct magnesium-binding sites probably underlie these two effects.

Magnesium weakens the kinetochore's grip on microtubules in a disassembly speed-independent manner, and this effect can be rescued by addition of exogenous Dam1c

To investigate the role of protofilament curls in the attachment and motility of kinetochores, we needed to first isolate increases in protofilament curl size induced by magnesium from changes in disassembly speed, absent any kinetochore attachment. Subtilisin treatment achieves this effect, but many microtubule binding proteins rely on interaction with the c-terminal tails of tubulin for binding to the lattice. Replacement of approximately sixty percent of the GTP in solution with the slowly-hydrolysable GTP analog GmpCpp was sufficient to maintain disassembly speed at a constant level across high magnesium concentrations (figure 6a). To check that protofilament curl properties remained unchanged, we measured pulse amplitudes across a variety of trapping forces for the high magnesium, sixty percent GmpCpp condition. The pulse amplitude-force relationship at sixty percent GmpCpp was indistinguishable from the GTP-only condition, suggesting protofilaments remained large (and mechanically unchanged) with addition of this level of GmpCpp in solution (figure 6b).

To evaluate the role of magnesium-based protofilament curl enlargement in kinetochore attachment, we used a different optical trapping assay. We sparsely decorated beads with immunoprecipitated yeast kinetochores, attached them to dynamic microtubule tips, and increased the force until ruptures were measured [37]. The rupture was measured in the presence of varying levels of magnesium. The decrease

in rupture forces at higher magnesium levels was not able to be rescued by replacement of 60% of the GTP with GmpCpp, suggesting magnesium directly weakens the microtubule-kinetochore interaction regardless of disassembly speed (figure 6c). As the immunoprecipitated kinetochore particles used for this assay likely contain insufficient levels of Dam1c for ring formation [37], we speculated that addition of exogenous recombinant Dam1c could allow for ring formation and harnessing of larger protofilament curls. Addition of 5 nM recombinant Dam1c made no change to rupture forces measured at low levels of magnesium, but fully rescued rupture forces at elevated levels of magnesium, suggesting kinetochore-Dam1 ring coupling can take advantage of enlarged protofilament curls to sustain attachment.

Discussion

Yeast and mammalian microtubules store similar lattice strain energies

Fitting our wave assay data with the multi-protofilament model has allowed us to directly estimate a key biophysical property of curling protofilaments at disassembling microtubule tips: their flexural rigidity. Previously, this property was only inferred indirectly, from static cryo-electron tomograms [35] or from stiffness measurements of intact microtubules [38-40]. Our fitted estimate for bending stiffness, 176±15 pN·nm·rad^{-1}, implies that fully straightening a protofilament from its relaxed curvature into a lattice-compatible state would require approximately 17 kBT of work energy per tubulin dimer, or 10 kcal/mol. This represents a very substantial fraction (~80%) of the free energy available from GTP hydrolysis, ~12.3 kcal/mol [1, 41], consistent with previous suggestions that most of the energy derived from hydrolysis is stored as curvature strain in the microtubule lattice [42], and consistent with our previous lower-bound estimate [14]. Moreover, our analysis suggests that the flexural rigidity of curling protofilaments is conserved between yeast and bovine tubulin, and therefore that the amount of strain energy stored per tubulin dimer in the microtubule lattice is probably also conserved.

The idea that protofilament flexural rigidity and stored lattice strain are conserved, despite a billion years of evolution separating yeast and vertebrates, suggests that these biophysical properties are crucial to microtubule function. Indeed, most current models assume that microtubule dynamic instability arises from the counteracting influences of lateral bonding versus lattice strain, which tend to stabilize and destabilize the polymer, respectively [35, 40, 43, 44]. Given the importance of dynamic instability for cell viability, there may be strong selective pressure to maintain a specific lattice strain energy.

Protofilament curl length can affect mechanical work output

In contrast to their consistent flexural rigidity, the average length of protofilament curls at disassembling microtubule tips can vary widely depending on tubulin species and buffer conditions [35, 45]. By our estimates, the average curl length grew ~50% as magnesium was increased from 1 to 20 mM. And curls at yeast microtubule tips were ~twofold larger than those at bovine microtubule tips. These curl enlargements were associated with greater mechanical work output in the wave assay, as expected, since longer curls store more elastic energy and can push the bead laterally farther away from the microtubule surface. We suggest that longer protofilament curls might similarly enhance microtubule-driven motility in vivo. In budding yeast, where each kinetochore attaches a single microtubule tip [46], and where robust tip-coupling depends on the ring-forming Dam1 [47-50], a minimum curl length might be required for microtubule-encircling Dam1 rings to efficiently harness curl energy via the conformational wave mechanism [51]. In other species whose kinetochores attach numerous microtubule tips and lack any ring-forming complexes, coupling might depend less on the conformational wave mechanism and instead might rely on biased diffusion [8]. An attractive idea is that the larger and more energetic pulses produced by yeast microtubules in the wave assay, as compared to bovine

microtubules, might reflect stronger selective pressure to maintain long protofilament curls, because yeast might depend more heavily on long curls for mitosis.

Another possibility suggested by our work is that cells might actively tune protofilament curl properties in order to enhance microtubule-driven motility. Because free magnesium is generally thought to be buffered around 1 mM inside eukaryotic cells [52, 53], we have viewed magnesium primarily as a biochemical tool, rather than a physiological mechanism for tuning curl properties. Interestingly, however, transient increases in free magnesium have recently been seen during metaphase and anaphase in dividing HeLa cells, where they apparently contribute to chromosome condensation [54]. But the estimated concentrations remain too low (0.3–1 mM) to significantly enlarge pulses in our wave assay. Therefore, we currently favor the idea that plus end-binders (+TIPs) and other microtubule-associated proteins known to alter microtubule tip morphology [55-59] could enlarge or stiffen protofilament curls, potentially enhancing their mechanical work output in a spatiotemporally regulated manner. We hope to investigate the effects of +TIPs on wave assay pulses in the future.

Magnesium directly inhibits the breakage of protofilament curls

Our measurements also reveal new information about the relationship between disassembly speed and protofilament curl length, and about the mechanisms by which magnesium affects these tip properties. Classic work suggested that elongation of protofilament curls by magnesium might be a simple indirect consequence of its acceleration of disassembly [22]. However, in 20 mM magnesium, subtilisin-treated microtubules disassembled threefold more slowly than untreated controls, and yet their pulse amplitudes remained consistently elevated, at well over 30 nm on average. Likewise, we previously showed that microtubules composed of a hyperstable T238V mutant tubulin disassemble sevenfold more slowly, and yet they generated pulses with amplitudes indistinguishable from wild-type [14]. These observations indicate that disassembly speed and curl length are not strictly coupled, and that magnesium-dependent enlargement of protofilament curls is not simply a consequence of accelerated disassembly. Rather, magnesium must directly inhibit the breakage of protofilament curls.

The effects of magnesium on disassembly speed and on curl length appear to be mediated by different interaction sites on tubulin. Magnesium's acceleration of disassembly depends on the β-tubulin C-terminal tail, since this effect is suppressed upon removal of the β-tail by subtilisin [18]. But subtilisin treatment did not suppress the effect of magnesium on pulse amplitudes in the wave assay, indicating that magnesium inhibits curl breakage through another interaction site (or sites), outside the β-tail. The C-terminal tail on α-tubulin is more resistant to subtilisin proteolysis and was left partially intact by our treatment (Figure 5a). Therefore, one possibility is that magnesium stabilizes protofilament curls by interacting with the α-tubulin tail. Alternatively, the effect might depend on an interaction with GDP in the exchangeable nucleotide-binding site, which is located at the inter-dimer interface. The affinity of magnesium for GDP in the exchangeable site is reportedly in the millimolar range [60, 61], which is much weaker than its affinity for GTP, and near the range where we measured increased pulse amplitudes.

Enlarged protofilament curls are associated with higher rupture forces for ring-forming levels of Dam1c

The rupture force of microtubule-kinetochore attachments on disassembling microtubules was weakened by the addition of magnesium. A salt-dependent weakening of the affinity of Ndc80c for the microtubule lattice has been reported for yeast Ndc80c [62], therefore a weakening of the microtubule-kinetochore attachment at elevated cation levels is not surprising. The oligomerization of the Dam1 complex on microtubules is reportedly less sensitive to ionic strength and is expected to form rings at approximately 5 nM [63]. Ring-forming levels of dam1 rescue the low rupture strength caused by

elevated levels of magnesium, suggesting the kinetochore can take advantage of enlarged protofilament curls if Dam1c rings suitable for harnessing such rings are present. To rigorously test this hypothesis, a way to elongate protofilament curls independent of any affinity of the kinetochore for the lattice is needed.

Tuning curl properties could facilitate additional testing of their importance for kinetochore motility

The ability to tune protofilament curl properties by adjusting magnesium levels or tubulin isoforms suggests new approaches for testing the importance of curling protofilaments in kinetochore motility. If curling protofilaments exert force to drive kinetochore movement, as proposed in conformational wave-based models, then elongating the curls could enable protofilaments to push more productively against the kinetochore, potentially changing the processivity, attachment strength, or switching behavior of the kinetochore-microtubule interface. In addition, we anticipate using our wave assay and the analytical tools described here to explore other methods for modifying biophysical properties of protofilament curls. In particular, the ability to tune bending stiffness or intrinsic curvature would provide additional ways to test the importance of protofilament curls in microtubule-based motility.

Materials and methods

Purification of tubulin from bovine brain

Tubulin was purified from bovine brain using two cycles of polymerization and depolymerization to a final concentration of 200 μM [64]. Samples were frozen in liquid N2 and stored at –80°C.

Purification of recombinant His6-tubulin from yeast

Plasmids to express wild-type yeast αβ-tubulin with a His6 tag fused to the C-terminus of β-tubulin were previously described [24, 65, 66]. The integrity of all expression constructs was confirmed by DNA sequencing. Wild-type yeast αβ-tubulin was purified from inducibly overexpressing strains of Saccharomyces cerevisiae using nickel affinity and ion exchange chromatography [24, 65, 66]. Tubulin samples for the laser trap assays were prepared at UT Southwestern, aliquoted, and snap-frozen in storage buffer (10 mM PIPES pH 6.9, 1 mM MgCl2, 1 mM EGTA), containing 50 μM GTP, shipped on dry ice to the University of Washington, and stored at –80°C.

Bead and slide preparation for wave assay

To prepare anti-His beads, ~30 pM of streptavidin-coated polystyrene microspheres (Spherotech Inc, SVP-05–10) was incubated with 30 pM biotinylated anti-penta-His antibodies (R&D Systems Inc, BAM050) for 30 min, washed extensively, and then stored at 4°C for up to several months. For each experiment, a small channel ~1 mm wide was formed by bonding a KOH-cleaned glass coverslip to a clean glass slide using two parallel strips of double-stick tape. Biotinylated bovine serum albumin (Vector Laboratories, B-2007–10) was incubated in the channel for 15 min, then washed out with 80 μL warm BRB80 (80 mM PIPES, 120 mM K+, 1 mM MgCl2, and 1 mM EGTA, pH 6.8). Avidin DN (Vector Laboratories, A-3100–1) was incubated in the channel for 5 min, then washed out with 40 μL warm BRB80. GMPCPP-stabilized, biotinylated microtubule seeds were assembled from bovine brain tubulin (Castoldi and Popov, 2003) and biotinylated porcine brain tubulin (Cytoskeleton, Cat #T333), and incubated in the channel for 5 min before washing with growth buffer (1 mM GTP in BRB80). Just prior to each experiment, a small aliquot of anti-His beads was pre-incubated with a mixture of plain and biotinylated BSA (at 10 and 0.1 mg mL–1, respectively) for 30 min, then decorated with His6-yeast tubulin, and then added to growth buffer containing 10–25 μM bovine tubulin. This reaction mixture was added to the seed-decorated coverslip, the slide was then sealed with nail polish, and mounted on the

optical trap. Pre-incubation of the anti-His beads with biotinylated BSA was important for preventing non-specific attachment of the beads to the microtubules. Control experiments with beads lacking anti-His antibody confirmed that the attachments were specific after the BSA pre-incubation. To ensure that most beads attached via single antibodies, the molar ratio of antibodies to beads was kept very low, ~1:1, such that the fraction of tubulin-decorated beads that would attach to the growing end of a microtubule under manual manipulation was typically less than 10%. Active beads attached readily to growing ends but not to the sides of microtubules. Their exclusive preference for growing ends is expected because the anti-His antibodies on the bead become quickly occupied by individual, unpolymerized tubulin dimers upon initial mixing with the His6-tagged yeast tubulin. Laterally attached beads, which are required for the wave assay, arise by the incorporation of bead-tethered yeast tubulin dimers into the growing ends of microtubules (which can be composed either of bovine or yeast tubulin, depending on the experiment) followed by polymerization of the microtubules past the beads. A detailed protocol for slide preparation is given in our recent publication (Murray et al., 2022).

Trapping instrument

The optical trap instrument used for this assay has been described in previous work (Franck et al., 2010). The instrument was based around a Nikon inverted microscope (TE2000) with a Nikon 100×1.4 NA oil Plan Apo IR CFI objective. A 1064 nm Nd:YVO4 laser (Spectra Physics J20-BL10-106Q) was used as a trapping beam, focused at the center of the field of view. A 473 nm laser (LaserPath Technologies, DPSS-473–100) was used as a microtubule cutting beam, focused into an ellipse at an intermediate distance between the trap center and edge of the field of view. Both lasers were actuated by shutters (Vincent Associates, VS25S2ZMO). Microtubules and beads were visualized by video enhanced differential interference contrast (VE-DIC), with illumination by a mercury arc lamp (X-Cite 120) and accomplished through two standard Wollaston prisms and polarizers (Walker et al., 1988). Motion control and force-feedback were implemented through servo-control of a three-axis piezo stage with internal capacitive position sensors (Physik Instrumente, P-517.3CL) and a piezo controller (Physik Instrumente, E-710). Custom software written in LabVIEW (National Instruments) was used for instrument control and data acquisition. The source code is publicly available at https://github.com/casbury69/laser-trap-control-and-data-acquisition (Asbury, 2021). Briefly, analog signals from the position sensor were sampled at 40 kHz using an analog-to-digital conversion board (National Instruments, PCI-6251). Commands were sent to the piezo stage controller through a GPIB digital interface (National Instruments, GPIB-USB-B). Both the bead and stage positions were downsampled to 200 Hz for file storage.

Measurement of pulses driven by protofilament curling

Suitable beads laterally attached to coverslip-anchored microtubules were identified. Suitable microtubules were firmly anchored by one end to the slide surface, and able to freely rotate about their surface anchor, without other interfering microtubules bundled alongside or crossing along their length. To establish the initial loaded state, the laterally attached bead was trapped, and the microtubule and bead were pulled in the opposite direction of the tether, toward the cutting laser location. The beads were raised slightly above the coverslip surface to ensure the surface did not interfere with measurement. The force clamp was initiated, and microtubule depolymerization was triggered by trimming off the stabilizing cap using the cutting laser. Position signals from the trapped bead were recorded using the force clamp software (described above under Trapping instrument), including the static baseline position and the pulse driven by protofilament curling motion. Candidate pulses were evaluated for inclusion in data analysis on the basis of their amplitude relative to the standard deviation of the baseline noise; a detection threshold of three times the standard deviation was used to accept or reject pulses. For most records this threshold was 6–10 nm, as detailed in our prior publication (Murray

et al., 2022). The fraction of events that yielded measurable pulses in bovine microtubule experiments was lower than in yeast microtubule experiments mainly because the pulses were smaller on average, and therefore more of them fell below our detection threshold.

Average pulse amplitudes are reported in the text as mean ± 95% confidence interval, which was estimated as ± (t·SEM), where t is drawn from Student's t-distribution using ν=N – 1 degrees of freedom. The number of samples per mean ranged from N=9 to 43, as indicated in the legends of Figures 2 and 3. All the individual pulse amplitude values are included in excel spreadsheet format as supplemental source data files. They are also publicly available as a MATLAB (Mathworks) data file at https://github.com/protofilamentdude/Protofilament-Bending-Models (Murray, 2022). Uncertainties in the measured work outputs shown in Figure 3b were estimated by propagating uncertainty in the parameters of the best-fit lines of Figure 3a through the calculation of area under each line. (Uncertainties in the best-fit line parameters were assumed to be uncorrelated.)

Measurement of microtubule disassembly speeds

Slides for measuring disassembly speeds were prepared as described above (in Bead and slide preparation for wave assay) but without the addition of yeast-tubulin decorated beads. Microtubules were visualized by VE-DIC and recorded using a digital video disc recorder (Toshiba, DR430). The stabilizing GTP-caps of microtubules were trimmed off using laser scissors to induce disassembly. Disassembly speeds of individual microtubules were measured using imageJ and mTrackJ (Meijering et al., 2012).

Multi-protofilament model

Single protofilaments were modeled as a series of rigid rods linked by Hookean bending springs with an angular spring constant, κ, a non-zero relaxed angle, θ_i (Figure 4a), and a segment length, r=8.2 nm. A downward force at the protofilament tip was balanced by the torque at each spring node to yield a system of nonlinear equations (see Equations 1–3 below for a 4-node, 3-segment system).

$$\tau_3 = Fr\cos(\theta_1 + \theta_2 + \theta_3) - \kappa(\theta_3 - \theta_i) \qquad \textit{equation 1}$$

$$\tau_2 = Fr[\cos(\theta_1 + \theta_2) + \cos(\theta_1 + \theta_2 + \theta_3)] - \kappa(\theta_2 - \theta_i) \qquad \textit{equation 2}$$

$$\tau_1 = Fr[\cos(\theta_1) + \cos(\theta_1 + \theta_2) + \cos(\theta_1 + \theta_2 + \theta_3)] - \kappa(\theta_1 - \theta_i) \qquad \textit{equation 3}$$

The system of non-linear equations was solved numerically for the angle at each node (θ1, θ2, θ3,...) using a variant of the Powell dogleg method (Powell, 1970), for a range of forces and a given set of parameters κ and θi. Using the angles (θ1, θ2, θ3,...), the deflection of the protofilament tip was calculated at each force. This method was repeated for modeled protofilaments of lengths 1–5 segments. The force-deflection relationship for multiple protofilaments at a microtubule tip interacting with a bead was calculated as follows: the bead was assumed to be an infinitely flat, rigid surface because the 440 nm beads used in experiments were nearly 20-fold larger in diameter than the microtubules. Protofilaments were assumed to be distributed radially about the microtubule axis in a 13-protofilament configuration. Bending was only allowed in the plane traversed by the microtubule axis and the protofilament axis because it has been observed in electron microscopy that such a plane includes most deviations in protofilament position [35]. The position of the bead surface was varied from where it contacted the most apical (upward pointing) protofilaments, down to the microtubule wall.

Accordingly, groups of protofilaments were engaged sequentially based on their distribution around the microtubule tip (Figure 4b, right). This sequential engagement of protofilaments manifested as slight ripples in the force-deflection curve and changed slightly depending on the rotational angle of the microtubule tip (Figure 4—figure supplement 3). To consider a variety of possible rotational angles, the force-deflection curves for the two microtubule tip rotations depicted in Figure 4—figure supplement 3 were averaged together prior to fitting. The model was implemented with custom code written in MATLAB (Mathworks) that is publicly available at https://github.com/protofilamentdude/Protofilament-Bending-Models (Murray, 2022).

Multi-protofilament model fitting

To fit the multi-protofilament model to the pulse amplitude versus force data, the amplitude data was first converted to bead-to-microtubule surface height, assuming a 36 nm tether length (Figure 1—figure supplement 2). The model was fit to the data using a Levenberg-Marquardt nonlinear least-squares algorithm with inverse-variance weights, yielding the fitted force-deflection relationship, and parameters for the stiffness per tubulin dimer and the average contour length. 95% confidence intervals were calculated using the Jacobian for each parameter. Fitting was performed using custom code written in MATLAB (Mathworks) and available publicly at https://github.com/protofilamentdude/Protofilament-Bending-Models [25].

Digestion of tubulin with subtilisin

To cleave the C-terminal tails from tubulin, bovine brain tubulin was thawed quickly, and mixed to a final concentration of 100 µM with 1% subtilisin (Sigma Aldrich P5380) in a buffer containing 1 mM GTP, 8 mg/mL BSA, 80 mM PIPES, pH 6.8, 1 mM $MgCl_2$, 1 mM EGTA, and immediately placed at 30°C. To halt the cleavage reaction, phenylmethylsulfonyl fluoride was added to a final concentration of 1 mM, and the cleavage product placed on ice.

Western blotting

Samples were run on a 7.5% Bis-Tris SDS-PAGE gel and transferred to polyvinylidene difluoride membranes. The membranes were blocked for 1 hr with 1:1 1× PBS and Odyssey Blocking Buffer (Licor Biosciences, 927–40000;). Primary and secondary antibodies were diluted in 1:1 1× PBS and Odyssey Blocking Buffer. The blots were incubated for 1 hr with the following primary antibodies: βTub (Cell Signaling Technology, 9F3) rabbit 1:1000, αTub DM1A:FITC (Sigma, F2168) mouse conjugate 1:1000. The blots were washed 3× with PBST (1× PBS and 0.01% Tween-20). The blots were incubated with secondary antibodies diluted in 1:1 1× PBS and Odyssey Blocking Buffer, IRDye 680RD goat anti-mouse IgG secondary antibody (Licor, 926–68070) 1:5000, IRDye 800CW goat anti-rabbit IgG secondary antibody (Licor, 926–32211) 1:5000. The blots were washed 3× with PBST and 1× with PBS, then imaged with a Licor Odyssey DLx imaging system. Images were adjusted for brightness and contrast with Image-J software.

Data availability

All data generated and analyzed during this study are included in the manuscript and supporting files. Source data files are provided with all the individual wave amplitude values and disassembly speeds for Figures 1–5 and their supplements. A source data file with all the individual wave amplitude values is also publicly available at https://github.com/protofilamentdude/Protofilament-Bending- Models (Murray, 2022), which includes custom MATLAB (Mathworks) code for fitting these data with the multi-protofilament model. The custom LabView (National Instruments) code that we use for control of our laser trapping instruments is publicly available at https://github.com/casbury69/lasertrap-control-and-data-acquisition (Asbury, 2021).

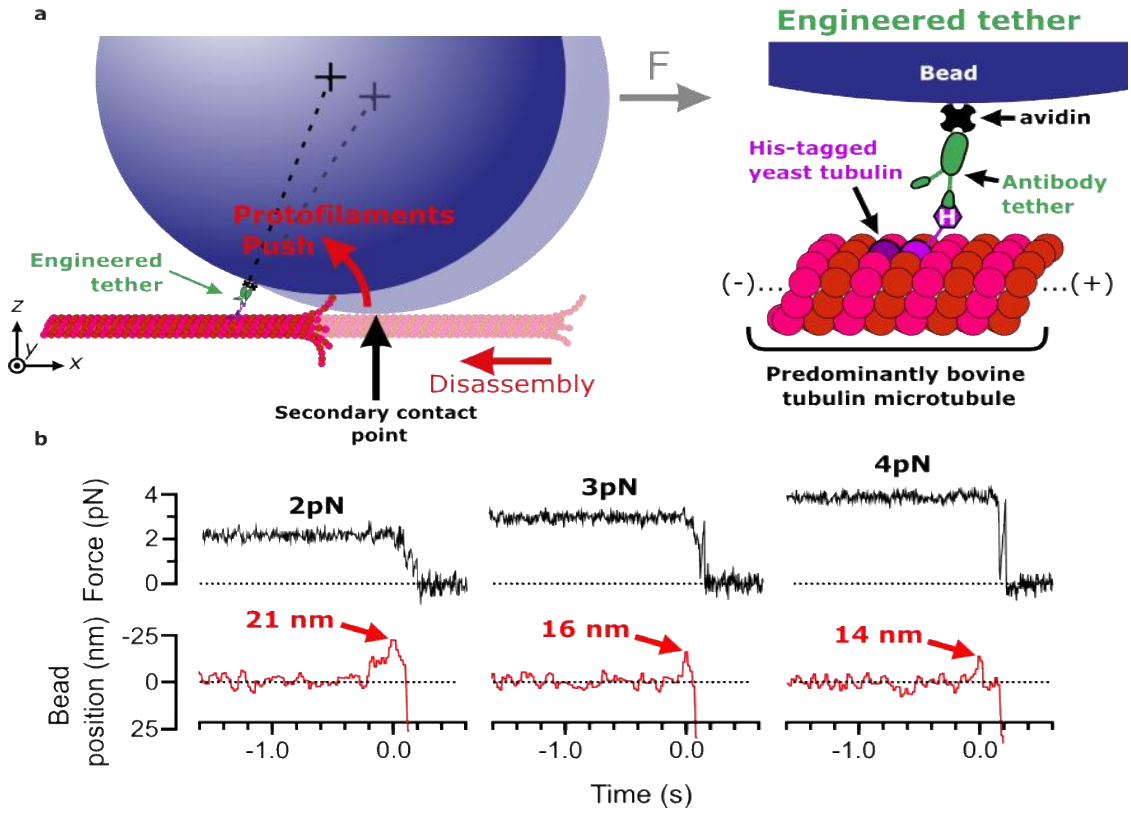

Figure 1: Measuring pulses of movement generated by protofilaments curling outward from the tips of disassembling bovine microtubules. (a) Schematic of the wave assay: a bead is tethered to the microtubule lattice via an engineered tether composed of recombinant His6-tagged yeast tubulin, a biotinylated anti-penta-His antibody, and streptavidin. Tethering by a single anti-penta-His antibody is ensured by keeping the density of antibodies on the beads very low. Using a laser trap, the bead is tensioned toward the (+)-end, pressing it against the microtubule lattice at a secondary contact point. The stabilizing GTP cap is trimmed off the microtubule with laser scissors to initiate disassembly. Curling protofilaments at the disassembling microtubule tip form a conformational wave that pushes laterally on the bead, causing it to rock back about its tether. This rocking action produces a pulse of bead movement against the force of the laser trap. (b) Records of force (black) and bead position (red) versus time for three different bead-microtubule pairs. As the trapping force on the bead was increased, pulse heights decreased, consistent with spring-like behavior of the protofilament curls.

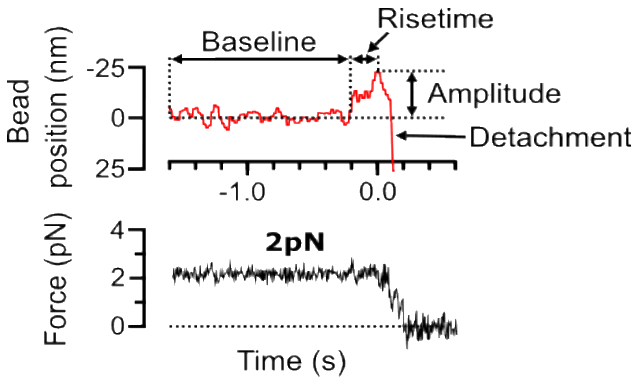

Figure 1—figure supplement 1: Features of the pulses of bead motion generated by curling protofilaments. Example record of bead position and trapping force versus time, measured during disassembly of a bovine brain tubulin microtubule in 1 mM magnesium. The bead position trace (red, top graph) prior to the pulse is characterized by a baseline noise. The pulse is parameterized by a risetime, the duration over which the signal increases from the baseline to the pulse peak. The height of the pulse from the baseline is defined as the pulse amplitude. After the pulse, the bead detaches from the microtubule, and the trap pulls the bead rapidly in the direction of applied force. Corresponding force trace (black, bottom graph) shows that the force is clamped (maintained at a steady level) until bead detachment.

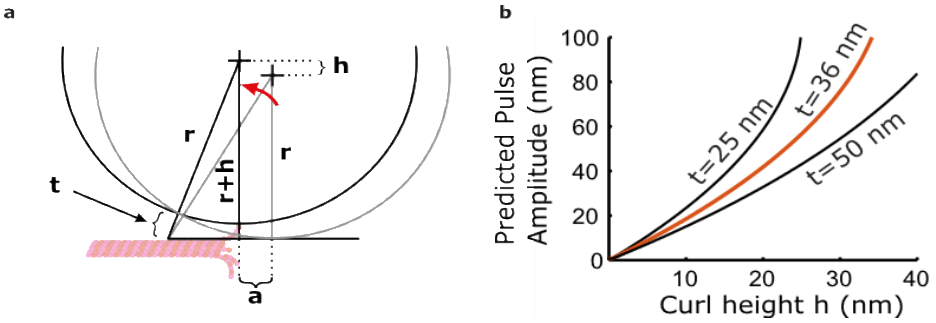

Figure 1—figure supplement 2: The bead and tether form a leverage system that amplifies protofilament curling motion. (a) Leverage given geometric constraints of bead and tether. Protofilament curl height, h, is amplified to a larger horizontal distance, a. (b) Relationship between pulse amplitude and curl height from the lattice given three different tether lengths (t=25, 36, and 50 nm). Based on the composition of the tether, we estimate a length of t=36 nm.

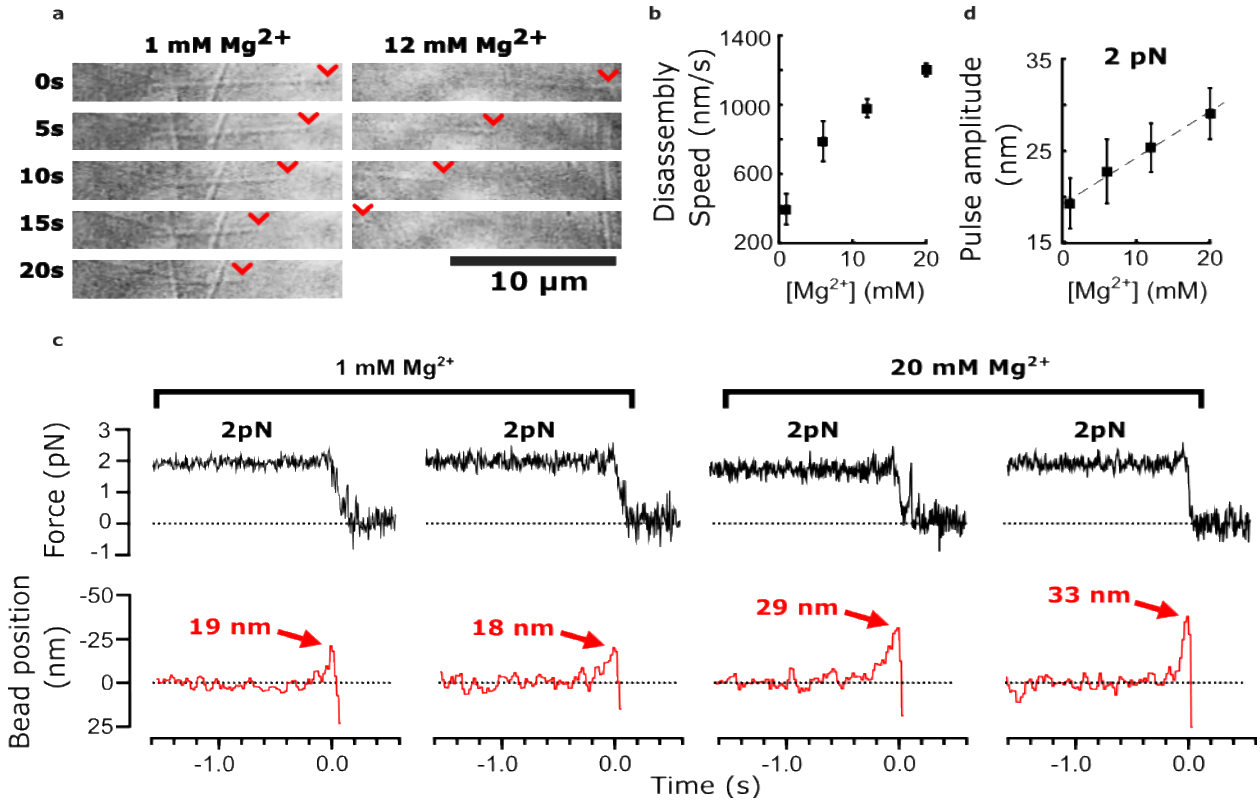

Figure 2: Added magnesium increases disassembly speed and pulse amplitude. (a) Time-lapse differential interference contrast images of individual microtubules disassembling in the presence of 1 or 12 mM magnesium. Arrowheads (red) indicate locations of disassembling tips. (b) Mean disassembly speed plotted against magnesium concentration. Error bars represent 95% confidence intervals, defined as ± (t·SEM), where t is drawn from Student's t-distribution (with ν=N – 1 degrees of freedom and N=34–51 samples per mean). (c) Records of force (black) and bead position (red) versus time for four bead-microtubule pairs, at two different magnesium concentrations. Pulse amplitudes were larger at the higher magnesium level. (d) Mean pulse amplitudes across four different magnesium concentrations, 1, 6, 12, and 20 mM. Error bars represent 95% confidence intervals (defined as in (b), with ν=N – 1 degrees of freedom and N=25–40 samples per mean). Data in (c) and (d) were collected at 2 pN trap force.

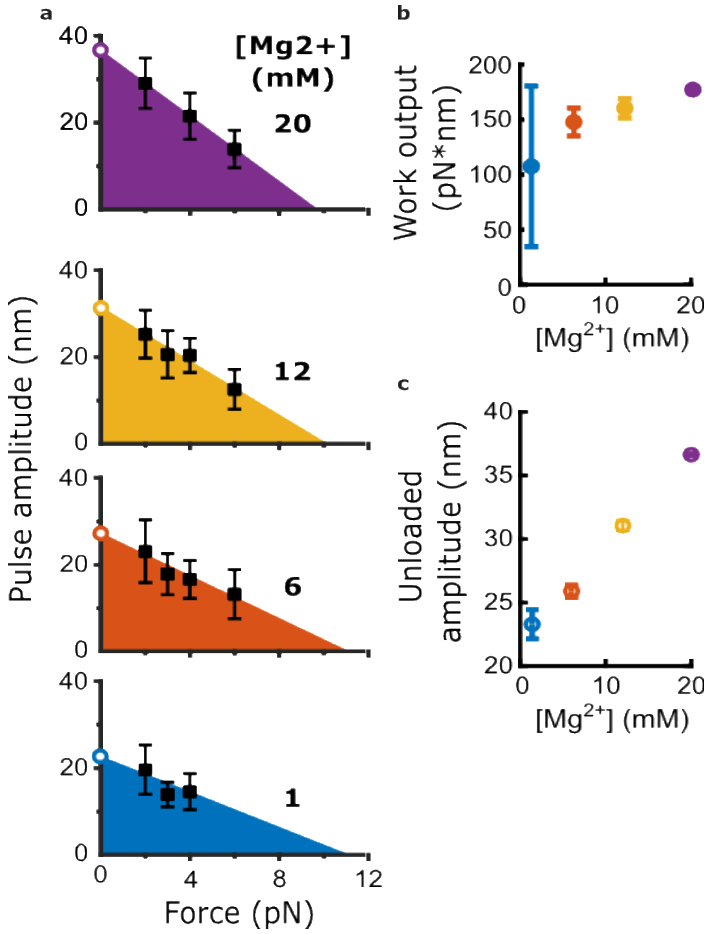

Figure 3: Magnesium increases the mechanical work output harnessed from curling protofilaments. (a) Mean pulse amplitudes (black squares) plotted against trapping force at the four indicated magnesium concentrations. Error bars represent 95% confidence intervals, defined as ± (t·SEM), where t is drawn from Student's t-distribution (with ν=N – 1 degrees of freedom and N=9–43 samples per mean). The capacity of protofilament curls to perform mechanical work in the assay was estimated at each magnesium concentration by fitting the amplitude versus force data with a line and then calculating the area under the line (colored triangular areas). To estimate unloaded pulse amplitudes, the line-fits were extrapolated to the y-intercept (open circles). (b) Mechanical work output, based on the colored areas shown in (a), plotted against magnesium concentration. Error bars represent 95% confidence intervals (estimated from the best-fit parameters, as explained in Materials and methods). (c) Unloaded amplitudes, based on extrapolation of the line-fits in (a), plotted versus magnesium concentration. Error bars represent 95% confidence intervals (estimated as explained in Materials and methods).

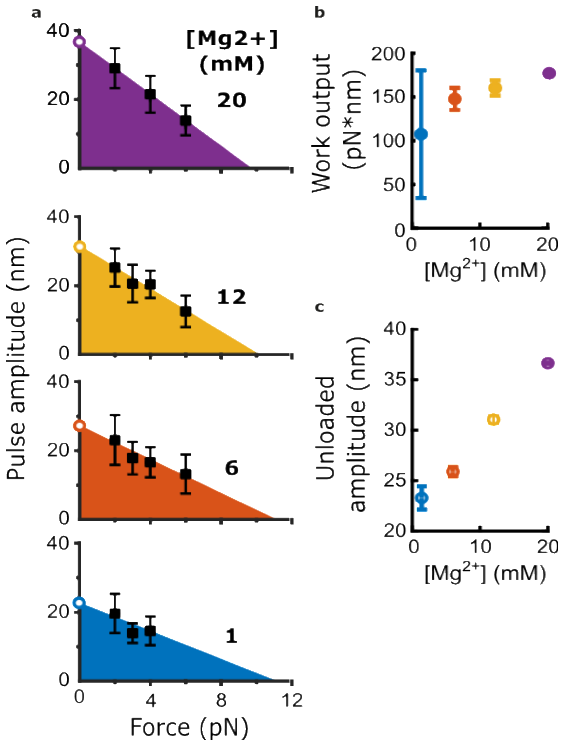

Figure 3—figure supplement 1: Cumulative distributions of pulse amplitude measured with bovine tubulin at different trapping forces and magnesium levels. (a) Cumulative distributions of pulse amplitude grouped together according to the trapping forces at which they were measured. Magnesium concentrations are denoted by color as indicated. (b) Cumulative distributions of pulse amplitude grouped together according to the magnesium concentrations at which they were measured. Trapping forces are denoted by color as indicated.

$[Mg^{2+}]$ (mM)	1	6	12	20
1	1			
6	0.258	1		
12	0.133	0.183	1	
20	0.046	2.95E-04	2.22E-03	1

Figure 3—figure supplement 2: Statistical comparisons of estimated work outputs across different magnesium concentrations. The table provides p-values for all possible comparisons of the work outputs estimated at 1, 6, 12, and 20 mM magnesium (i.e. the four work outputs plotted in Figure 3b), calculated based on Student's t-distribution.

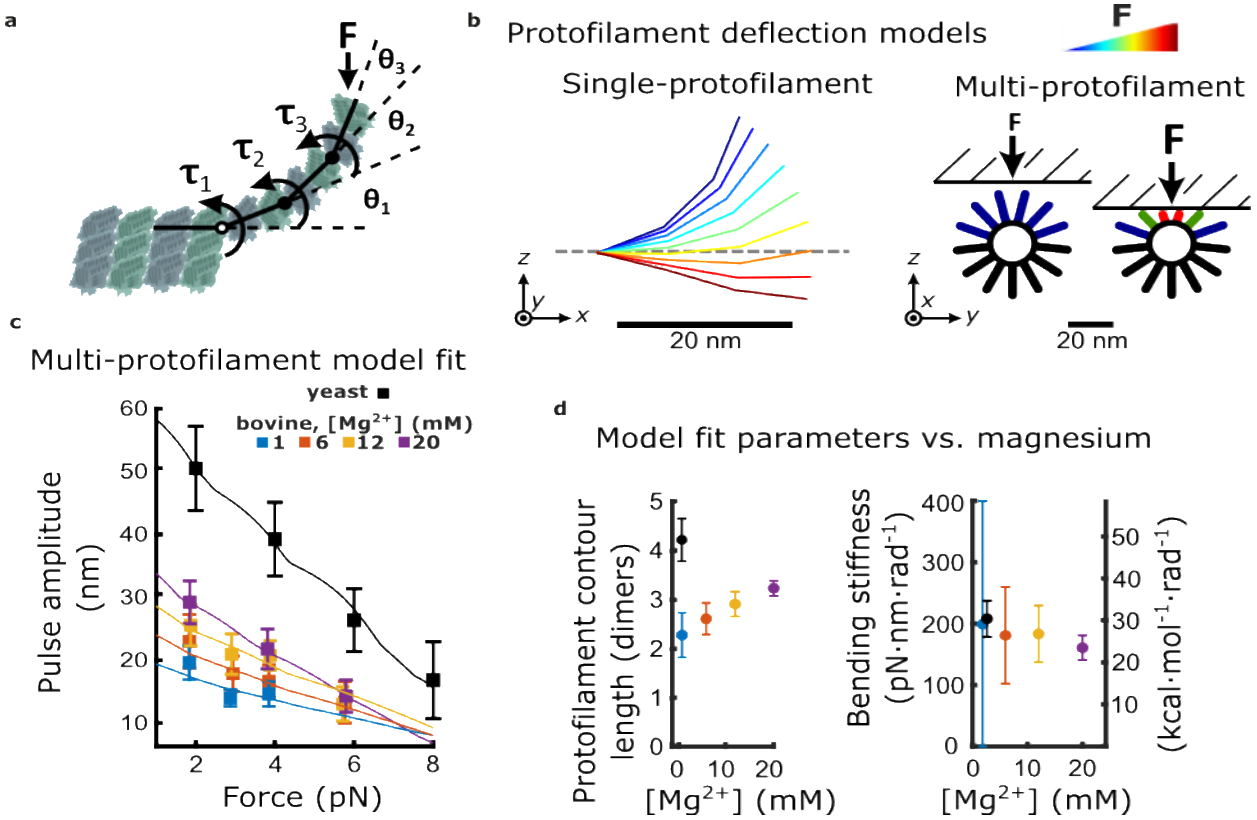

Figure 4: Magnesium- and species-dependent increases in work output can be explained solely by a lengthening of protofilament curls. (a) Model for bending of a single protofilament. Tubulin dimers are represented as rigid rods linked by Hookean torsion springs with relaxed angles of 23°. An external force, F, perpendicular to the microtubule long-axis, is applied at the protofilament tip. The balance between F and the torsion at each bending node, τn, is used to calculate the contour shape of the protofilament (i.e. the angles θn). (b) Calculated shapes for a single protofilament at different levels of external force (indicated by the color legend). Model for deflection of multiple protofilaments at a microtubule tip, seen end-on. Single protofilaments, modeled as in (a), are arranged radially according to the geometry of a 13-protofilament microtubule. The bead is modeled as a flat rigid surface, pushed downward onto the protofilaments to predict a force-deflection relationship. Cartoon at right shows distribution of protofilament deflections for an arbitrary bead height. (c) Amplitude versus force curves predicted by the multi-protofilament model, after fitting to measured pulse data (symbols) at indicated magnesium concentrations. Bovine data are recopied from Figure 3a. Yeast data combine new measurements with data previously published in Driver et al., 2017. (d) Two fitted parameters, the mean contour length and bending stiffness (flexural rigidity) of protofilament curls, plotted versus magnesium concentration. The fitted contour length increases with added magnesium and is larger for yeast microtubules, while the apparent flexural rigidity remains unchanged.

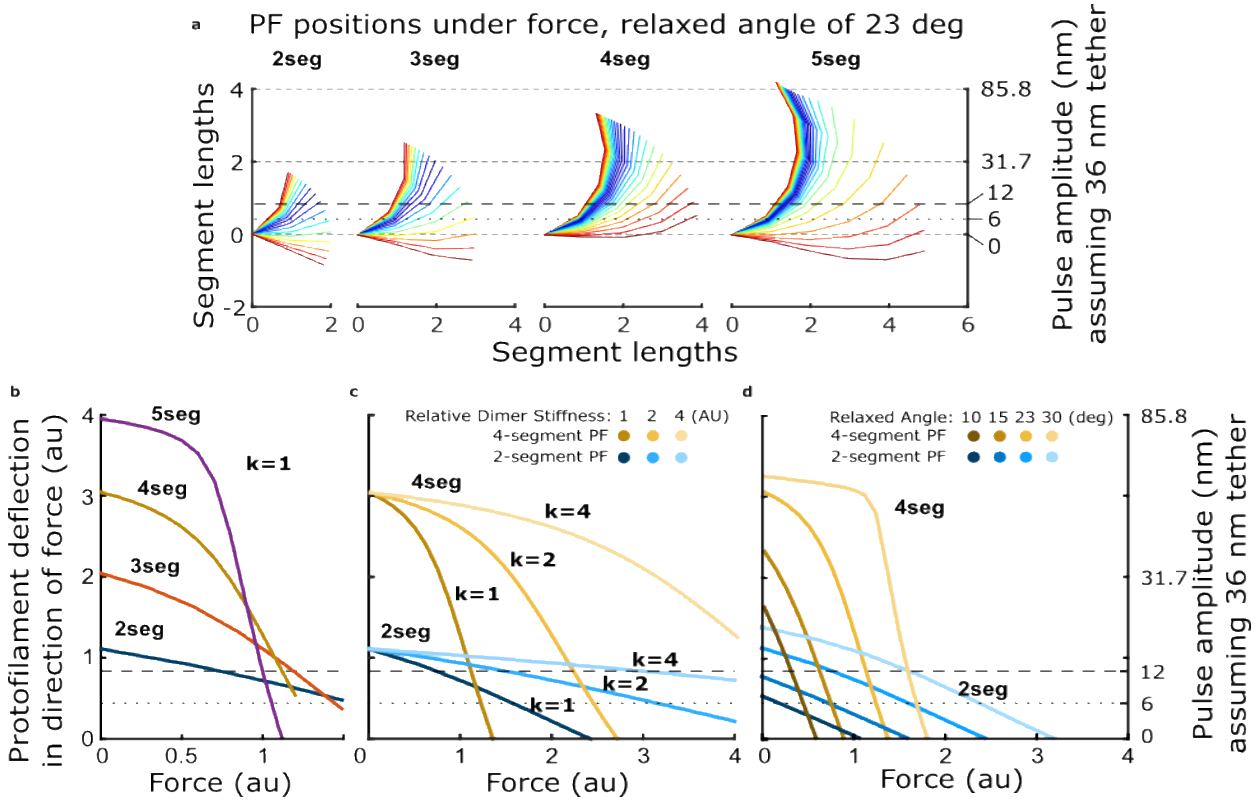

Figure 4—figure supplement 1: How force-deflection behavior of the single protofilament model changes with variation in the number of segments (dimers), the intrinsic bending stiffness, and the relaxed angle per tubulin dimer. (a) Model solutions for protofilament contour lengths of 2–5 segments, under a range of forces. Color indicates magnitude of force. (b) Deflection of the protofilament tip as a function of force for protofilaments of 2–5 segments. (c) Deflection of the tip for protofilaments 2 and 4 segments in length, with the stiffness per dimer varied twofold and fourfold above that used in Figure 4. (d) Deflection of the tip for protofilaments 2 and 4 segments in length, with the relaxed dimer angle varied across 10, 15, 23, and 30°.

Curvature (degrees per dimer)	*SE*	*Mesaured from*	*Ligand(s)*	*Description*	*Reference*
27.8		Cryo 2D	Presumed GDP	Curvature measured from diameter of PF curl 1 mM Mg2+	Mandelkow 1991
24.8		Cryo 2D	Presumed GDP	Curvature measured from diameter of PF curl 20 mM Mg2+	Mandelkow 1991
20.2	12.1	Cryo-ET trace	Presumed GDP	Cytoskeleton porcine tubulin grown from axonemes, with disassembly induced by isothermal dilution, BRB80 (1 mM Mg^{2+}). Average length of 43 ± 16 nm	McIntosh 2018
19.3	13.1	Cryo-ET trace	Presumed GTP	Cytoskeleton porcine tubulin grown from axonemes, BRB80 (1 mM Mg^{2+}). Average length of 36 ± 15 nm	McIntosh 2018
26	N/A	crystal structure	stathmin, GDP, colchicine	Colchicine known to induce curvature, curvature looks very close by eye when aligned by α-tub to structures submitted by Nawrotek et al.	Ravelli 2004
22	N/A	crystal structure	DARPin, GTP	DARPin binds at exposed terminus of β-tub, structure shows GTP bound at both E and N-sites.	Pecquer 2012
19	N/A	crystal structure	stathmin, GTP, GDP, GmpCpp	regardless of ligand at E-site, curvature remains seemingly constant. Stathmin may impose substantial influence on curvature*	Nawrotek 2011
21	13	Cryo-ET trace	Presumed GTP	10 µM Cytoskeleton porcine tubulin, growing MT	Gudimchuck 2020
21	14	Cryo-ET trace	Presumed GTP	20 µM Cytoskeleton porcine tubulin, growing MT	Gudimchuck 2020
18	13	Cryo-ET trace	Presumed GTP	40 µM Cytoskeleton tubulin, growing MT	Gudimchuck 2020
21	11	Cryo-ET trace	Presumed GTP	α1B/βI+βIVb tubulin, growing	Gudimchuck 2020
22.9				Assumed curvature of relaxed tubulin per model proposed (conversion from 0.2 rad)	Gudimchuck 2020
12	12.3	Cryo-ET trace	In vivo	KMT-PTK-meta 51 ± 21 nm length, 1,465 PF traces	McIntosh 2018
13.7	11.8	Cryo-ET trace	In vivo	KMT-PTK-ana 13.7 ± 11.8 nm length, 192 PF traces	McIntosh 2018
17.8	12.8	Cryo-ET trace	In vivo	KMT-Chlamy-meta 42 ± 15 nm length, 700 PF traces	McIntosh 2018
16.3	13.6	Cryo-ET trace	In vivo	KMT-Chlamy-ana 54 ± 14 nm length, 452 PF traces	McIntosh 2018
17.9	14.5	Cryo-ET trace	In vivo	KMT-CEleg-meta 44 ± 17 nm length, 315 PF traces	McIntosh 2018
22.9	19.1	Cryo-ET trace	In vivo	KMT-CEleg-ana 49 ± 18 nm length, 461 PF traces	McIntosh 2018
21.1	17.5	Cryo-ET trace	In vivo	KMT-Cerevis-meta 27 ± 11 nm length, 449 PF traces	McIntosh 2018
24.6	81.9	Cryo-ET trace	In vivo	KMT-Cerevis-ana 31 ± 12 nm length, 539 PF traces	McIntosh 2018
11.5	5.7	Oligomer fit (Cryo 2D)	GTP	Oligomers in early stages of assembly (Drosophila tubulin), GTP	Ayukawa 2021
15.8	5.6	Oligomer fit (Cryo 2D)	GDP	Oligomers in early stages of assembly (Drosophila tubulin), GDP	Ayukawa 2021
9.4		Cryo-ET		Tubulin sheets at MT tips (density is indistinguishable from dark moire fringe that defines MT wall, indicating multiple PF's in gently curving sheet.	Guesdon 2016
1		Cryo 2D		Finds miniscule curvatures from MT groups/sheets nucleated from axonemes (~1 deg/dimer)	Orbach and Howard 2019
25.8	0.21	Cryo 2D	GTP or GDP	measured by ring diameter of curling PF's at tips, did not differentiate between assembling and disassembling	Vemu 2017

Figure 4—Source data 2: Table of estimates of protofilament curvature reported in the literature. Each row is colored to reflect the method used to estimate protofilament curvature.

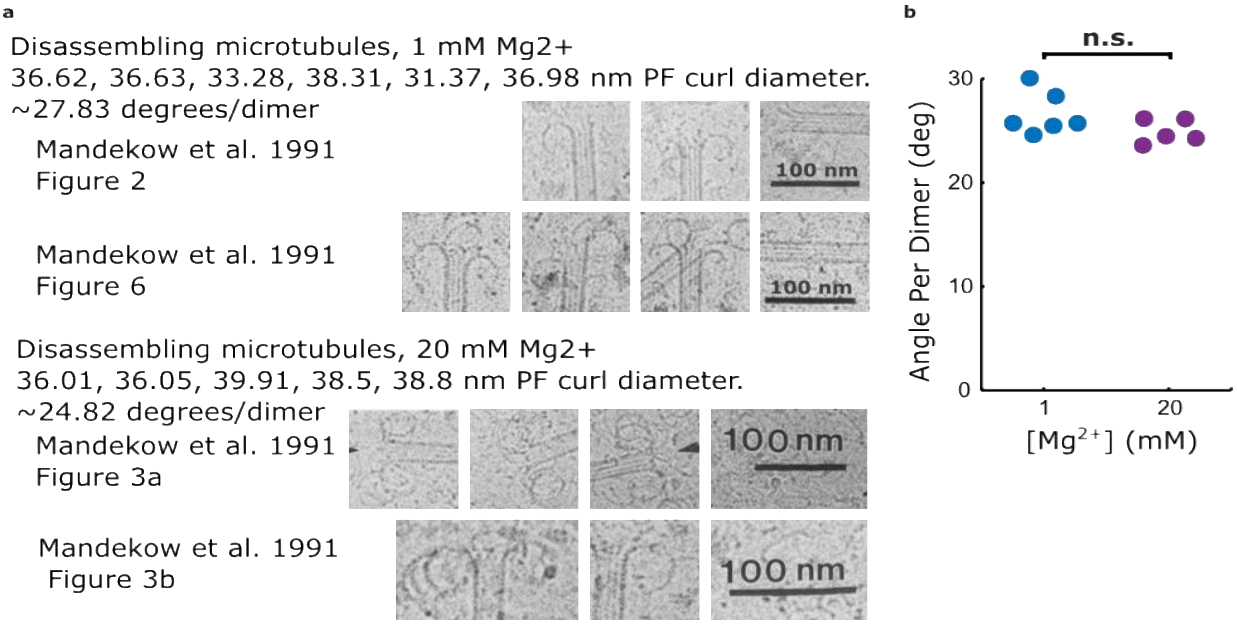

Figure 4—figure supplement 2: Estimates of protofilament curvature from micrographs of disassembling microtubule tips presented in Mandelkow et al., 1991. (a) Cropped two-dimensional cryo-electron microscopy micrographs from Mandelkow et al., 1991, showing curling protofilaments used to estimate curvature for various levels of magnesium. (b) Plot relating quantifications of curvatures from images shown in (a), estimated by measuring the diameter of the curl. Curvature per dimer is plotted for two different magnesium concentrations.

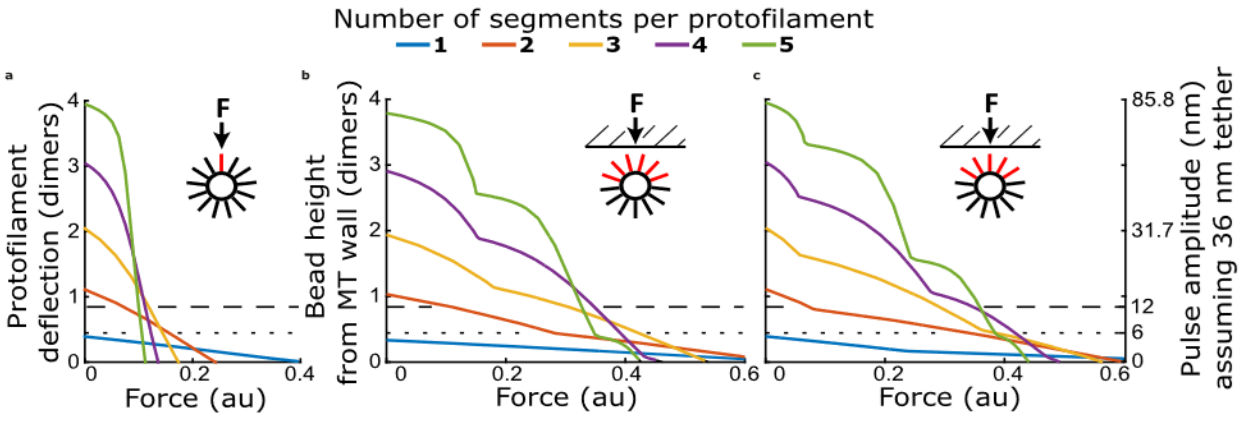

Figure 4—figure supplement 3: Comparison of force-deflection relationship for a single protofilament, and multiple protofilaments arranged to reflect geometry at a microtubule tip. (a) Protofilament tip deflection versus force for a single protofilament, with 1–5 segments. (b) Bead height versus force for a multi-protofilament model with protofilaments arranged in a 13-protofilament configuration, oriented such that two protofilaments initially contact the bead simultaneously. (c) Bead height versus force for a multi-protofilament model with the same arrangement of protofilaments as in (b) but rotated such that a single protofilament establishes bead contact first.

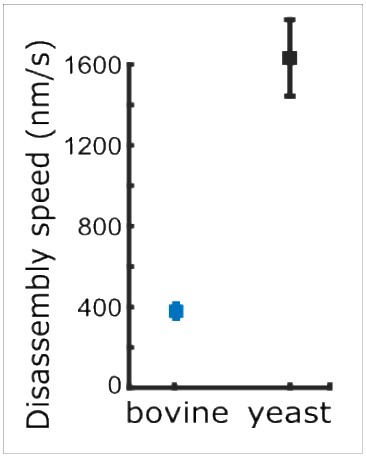

Figure 4—figure supplement 4: Comparison of disassembly speeds for bovine versus yeast microtubules. Yeast tubulin disassembles fourfold faster than bovine tubulin in the presence of 1 mM magnesium. Points are means. Error bars represent 95% confidence interval for the mean (based on Student's t-distribution).

a Contour length p-values

bovine [Mg^{2+}] (mM)	bovine 1	bovine 6	bovine 12	bovine 20	yeast
1	1				
6	0.235	1			
12	0.017	0.148	1		
20	1.29E-04	7.22E-04	0.030	1	
yeast	4.77E-12	2.67E-13	2.26E-12	9.85E-11	1

b Bending stiffness p-values

bovine [Mg^{2+}] (mM)	bovine 1	bovine 6	bovine 12	bovine 20	yeast
1	1				
6	0.867	1			
12	0.880	0.957	1		
20	0.706	0.623	0.375	1	
yeast	0.963	0.590	0.462	0.019	1

Figure 4—figure supplement 5: Statistical comparisons of estimated contour lengths and bending stiffnesses across different magnesium concentrations. (a) Table of p-values for all possible comparisons of protofilament curl contour lengths estimated for bovine microtubules at 1, 6, 12, and 20 mM magnesium and for yeast microtubules at 1 mM magnesium (i.e. the five contour lengths plotted in the left graph of Figure 4d). (b) Table of p-values for all possible comparisons of protofilament bending stiffness estimated for bovine microtubules at 1, 6, 12, and 20 mM magnesium

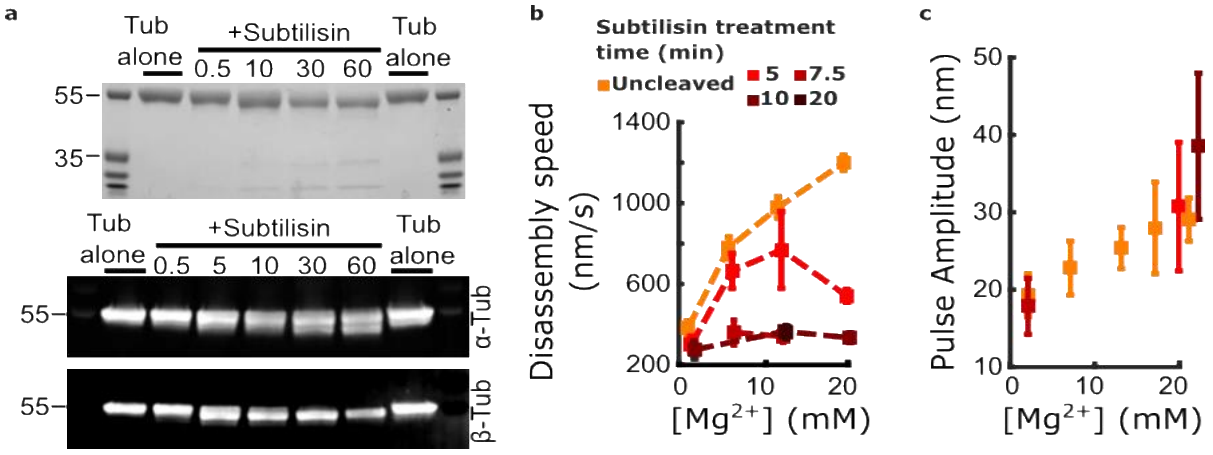

Figure 5: Removing the β-tubulin C-terminal tail suppresses magnesium's acceleration of disassembly speed but not its enhancement of pulse amplitude. (a) Proteolytic products of tubulin treated with subtilisin for the indicated times (in minutes), before quenching with 1 mM phenylmethylsulfonyl fluoride, visualized by Coomassie staining (top image) or Western blotting (bottom image). αTub DM1A:FITC mouse conjugate 1:1000 and βTub CST 9F3 rabbit 1:1000 were used for primary antibody staining. (b) Mean disassembly speeds, measured after treatment of tubulin with subtilisin for the indicated durations and plotted versus magnesium concentration. The large magnesium-dependent acceleration of disassembly seen with untreated tubulin (orange symbols) was suppressed after 10–20 min subtilisin treatment (dark red symbols). Error bars represent 95% confidence intervals, defined as ± (t·SEM), where t is drawn from Student's t-distribution (with v=N – 1 degrees of freedom and N=5–51 samples per mean). Data for untreated tubulin are recopied from Figure 2b. (c) Pulse amplitudes, measured in the wave assay at 2 pN trapping force after treatment of tubulin with subtilisin, plotted versus magnesium concentration. Symbol colors indicate subtilisin treatment times according to the legend of (a). Treatment with subtilisin did not suppress the effect of magnesium on pulse amplitude. Error bars represent 95% confidence intervals, defined as ± (t·SEM), where t is drawn from Student's t-distribution (with v=N – 1 degrees of freedom and N=28–44 samples per mean).

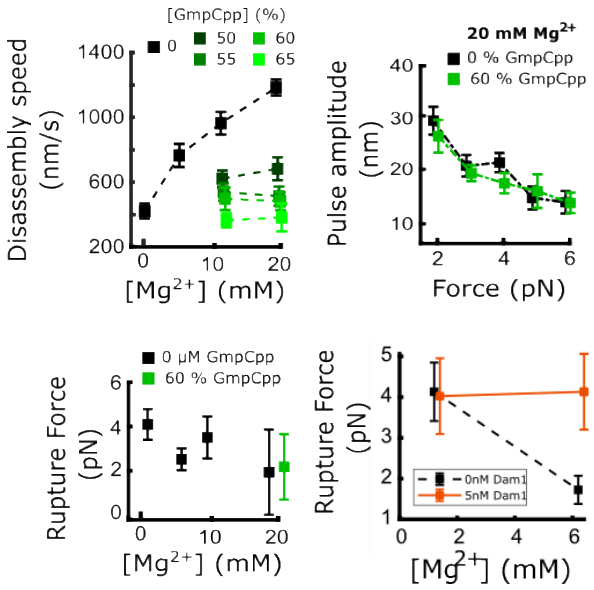

Figure 6: Magnesium weakens the kinetochore's grip on microtubules in a disassembly speed-independent manner, and this effect can be rescued by addition of exogenous dam1c: (a) The disassembly speed of microtubules is plotted versus the magnesium concentration. The fraction of GTP that was replaced by the slowly hydrolysable analog GmpCpp is indicated in the legend. (b) Pulse amplitudes from the wave assay are plotted versus the applied load for the level of GmpCpp that restores disassembly speeds to normal levels in (a). (c) The rupture force of microtubule-kinetochore attachments on disassembling microtubule tips as a function of magnesium concentration is plotted. Restoration of the disassembly speed to normal levels by addition of 60% GmpCpp is insufficient to rescue rupture strengths. (d) The rupture force for microtubule-kinetochore attachments is plotted versus the magnesium concentration. Recombinant dam1c protein was added to 5 nM. Error bars represent 95% confidence intervals, defined as ± (t·SEM), where t is drawn from Student's t-distribution (with ν=N – 1 degrees of freedom and N=18–57 samples per mean).

References

[1] A. Desai and T. J. Mitchison, "Microtubule polymerization dynamics," *Annual Review of Cell and Developmental Biology,* vol. 13, pp. 83-117, 1997.

[2] S. Inoue and E. D. Salmon, "FORCE GENERATION BY MICROTUBULE ASSEMBLY DISASSEMBLY IN MITOSIS AND RELATED MOVEMENTS," *Molecular Biology of the Cell,* vol. 6, pp. 1619-1640, Dec 1995.

[3] J. R. McIntosh, V. Volkov, F. I. Ataullakhanov, and E. L. Grishchuk, "Tubulin depolymerization may be an ancient biological motor," *Journal of Cell Science,* vol. 123, pp. 3425-3434, Oct 2010.

[4] J. L. Carminati and T. Stearns, "Microtubules orient the mitotic spindle in yeast through dynein-dependent interactions with the cell cortex," *Journal of Cell Biology,* vol. 138, pp. 629-641, Aug 1997.

[5] M. Dogterom, J. W. Kerssemakers, G. Romet-Lemonne, and M. E. Janson, "Force generation by dynamic microtubulles," *Current Opinion in Cell Biology,* vol. 17, pp. 67-74, Feb 2005.

[6] C. Kozlowski, M. Srayko, and F. Nedelec, "Cortical microtubule contacts position the spindle in C. elegans embryos," *Cell,* vol. 129, pp. 499-510, May 2007.

[7] T. Nguyen-Ngoc, K. Afshar, and P. Gonczy, "Coupling of cortical dynein and G alpha proteins mediates spindle positioning in Caenorhabditis elegans," *Nature Cell Biology,* vol. 9, pp. 1294-U158, Nov 2007.

[8] C. L. Asbury, J. F. Tien, and T. N. Davis, "Kinetochores' gripping feat: conformational wave or biased diffusion?," *Trends in Cell Biology,* vol. 21, pp. 38-46, Jan 2011.

[9] T. L. Hill, "THEORETICAL PROBLEMS RELATED TO THE ATTACHMENT OF MICROTUBULES TO KINETOCHORES," *Proceedings of the National Academy of Sciences of the United States of America,* vol. 82, pp. 4404-4408, 1985.

[10] A. F. Powers, A. D. Franck, D. R. Gestaut, J. Cooper, B. Gracyzk, R. R. Wei*, et al.*, "The Ndc80 Kinetochore Complex Forms Load-Bearing Attachments to Dynamic Microtubule Tips via Biased Diffusion," *Cell,* vol. 136, pp. 865-875, Mar 2009.

[11] M. W. Kirschner, R. C. Williams, M. Weingarten, and J. C. Gerhart, "MICROTUBULES FROM MAMMALIAN BRAIN - SOME PROPERTIES OF THEIR DEPOLYMERIZATION PRODUCTS AND A PROPOSED MECHANISM OF ASSEMBLY AND DISASSEMBLY," *Proceedings of the National Academy of Sciences of the United States of America,* vol. 71, pp. 1159-1163, 1974.

[12] E. M. Mandelkow and E. Mandelkow, "UNSTAINED MICROTUBULES STUDIES BY CRYO-ELECTRON MICROSCOPY - SUBSTRUCTURE, SUPERTWIST AND DISASSEMBLY," *Journal of Molecular Biology,* vol. 181, pp. 123-135, 1985.

[13] D. E. Koshland, T. J. Mitchison, and M. W. Kirschner, "POLEWARDS CHROMOSOME MOVEMENT DRIVEN BY MICROTUBULE DEPOLYMERIZATION INVITRO," *Nature,* vol. 331, pp. 499-504, Feb 1988.

[14] J. W. Driver, E. A. Geyer, M. E. Bailey, L. M. Rice, and C. L. Asbury, "Direct measurement of conformational strain energy in protofilaments curling outward from disassembling microtubule tips," *Elife,* vol. 6, p. 18, Jun 2017.

[15] E. T. Obrien, E. D. Salmon, R. A. Walker, and H. P. Erickson, "EFFECTS OF MAGNESIUM ON THE DYNAMIC INSTABILITY OF INDIVIDUAL MICROTUBULES," *Biochemistry,* vol. 29, pp. 6648-6656, Jul 1990.

[16] S. R. Martin, F. M. M. Butler, D. C. Clark, J. M. Zhou, and P. M. Bayley, "MAGNESIUM-ION EFFECTS ON MICROTUBULE NUCLEATION INVITRO," *Biochimica Et Biophysica Acta,* vol. 914, pp. 96-100, Jul 1987.

[17] E. M. Mandelkow, E. Mandelkow, and R. A. Milligan, "MICROTUBULE DYNAMICS AND MICROTUBULE CAPS - A TIME-RESOLVED CRYOELECTRON MICROSCOPY STUDY," *Journal of Cell Biology,* vol. 114, pp. 977-991, Sep 1991.

[18] C. P. Fees and J. K. Moore, "Regulation of microtubule dynamic instability by the carboxy-terminal tail of beta-tubulin," *Life Science Alliance,* vol. 1, p. 13, May 2018.

[19] D. L. Sackett, B. Bhattacharyya, and J. Wolff, "TUBULIN SUBUNIT CARBOXYL TERMINI DETERMINE POLYMERIZATION EFFICIENCY," *Journal of Biological Chemistry,* vol. 260, pp. 43-45, 1985.

[20] L. Serrano, J. Avila, and R. B. Maccioni, "LIMITED PROTEOLYSIS OF TUBULIN AND THE LOCALIZATION OF THE BINDING-SITE FOR COLCHICINE," *Journal of Biological Chemistry,* vol. 259, pp. 6607-6611, 1984.

[21] R. C. Weisenberg, "MICROTUBULE FORMATION IN-VITRO IN SOLUTIONS CONTAINING LOW CALCIUM CONCENTRATIONS," *Science,* vol. 177, pp. 1104-+, 1972.

[22] P. T. Tran, P. Joshi, and E. D. Salmon, "How tubulin subunits are lost from the shortening ends of microtubules," *Journal of Structural Biology,* vol. 118, pp. 107-118, Mar 1997.

[23] E. L. Grishchuk, M. I. Molodtsov, F. I. Ataullakhanov, and J. R. McIntosh, "Force production by disassembling microtubules," *Nature,* vol. 438, pp. 384-388, Nov 2005.

[24] V. Johnson, P. Ayaz, P. Huddleston, and L. M. Rice, "Design, Overexpression, and Purification of Polymerization-Blocked Yeast alpha beta-Tubulin Mutants," *Biochemistry,* vol. 50, pp. 8636-8644, Nov 2011.

[25] L. E. Murray, H. Kim, L. M. Rice, and C. L. Asbury, "Catching the conformational wave: measuring the working strokes of protofilaments as they curl outwards from disassembling microtubule tips," *Methods in molecular biology (Clifton, NJ.),* vol. 2478, 2022 2022.

[26] A. D. Franck, A. F. Powers, D. R. Gestaut, T. N. Davis, and C. L. Asbury, "Direct physical study of kinetochore-microtubule interactions by reconstitution and interrogation with an optical force clamp," *Methods,* vol. 51, pp. 242-250, Jun 2010.

[27] J. W. Driver, E. Geyer, L. M. Rice, and C. L. Asbury, "On the Force-Generating Capacity of Disassembling Microtubules," *Biophysical Journal,* vol. 110, pp. 192A-192A, Feb 2016.

[28] S. C. Howes, E. A. Geyer, B. LaFrance, R. Zhang, E. H. Kellogg, S. Westermann*, et al.*, "Structural and functional differences between porcine brain and budding yeast microtubules," *Cell Cycle,* vol. 17, pp. 278-287, 2018.

[29] E. Nogales, F. J. Medrano, G. P. Diakun, G. R. Mant, E. Townsandrews, and J. Bordas, "THE EFFECT OF TEMPERATURE ON THE STRUCTURE OF VINBLASTINE-INDUCED POLYMERS OF PURIFIED TUBULIN - DETECTION OF A REVERSIBLE CONFORMATIONAL CHANGE," *Journal of Molecular Biology,* vol. 254, pp. 416-430, Dec 1995.

[30] J. B. Olmsted and G. G. Borisy, "IONIC AND NUCLEOTIDE REQUIREMENTS FOR MICROTUBULE POLYMERIZATION INVITRO," *Biochemistry,* vol. 14, pp. 2996-3005, 1975.

[31] A. C. Rosenfeld, R. V. Zackroff, and R. C. Weisenberg, "MAGNESIUM STIMULATION OF CALCIUM-BINDING TO TUBULIN AND CALCIUM INDUCED DEPOLYMERIZATION OF MICROTUBULES," *Febs Letters,* vol. 65, pp. 144-147, 1976.

[32] L. Serrano, J. Delatorre, R. B. Maccioni, and J. Avila, "INVOLVEMENT OF THE CARBOXYL-TERMINAL DOMAIN OF TUBULIN IN THE REGULATION OF ITS ASSEMBLY," *Proceedings of the National Academy of Sciences of the United States of America-Biological Sciences,* vol. 81, pp. 5989-5993, 1984.

[33] J. C. Lee and S. N. Timasheff, "RECONSTITUTION OF MICROTUBULES FROM PURIFIED CALF BRAIN TUBULIN," *Biochemistry,* vol. 14, pp. 5183-5187, 1975.

[34] L. A. Amos and A. Klug, "ARRANGEMENT OF SUBUNITS IN FLAGELLAR MICROTUBULES," *Journal of Cell Science,* vol. 14, pp. 523-549, 1974.

[35] J. R. McIntosh, E. O'Toole, G. Morgan, J. Austin, E. Ulyanov, F. Ataullakhanov*, et al.*, "Microtubules grow by the addition of bent guanosine triphosphate tubulin to the tips of curved protofilaments," *Journal of Cell Biology,* vol. 217, pp. 2691-2708, Aug 2018.

[36] T. Muller-Reichert, D. Chretien, F. Severin, and A. A. Hyman, "Structural changes at microtubule ends accompanying GTP hydrolysis: Information from a slowly hydrolyzable analogue of GTP, guanylyl (alpha,beta)methylenediphosphonate," *Proceedings of the National Academy of Sciences of the United States of America,* vol. 95, pp. 3661-3666, Mar 1998.

[37] B. Akiyoshi, K. K. Sarangapani, A. F. Powers, C. R. Nelson, S. L. Reichow, H. Arellano-Santoyo*, et al.*, "Tension directly stabilizes reconstituted kinetochore-microtubule attachments," *Nature,* vol. 468, pp. 576-U255, Nov 2010.

[38] T. Hawkins, M. Mirigian, M. S. Yasar, and J. L. Ross, "Mechanics of microtubules," *Journal of Biomechanics,* vol. 43, pp. 23-30, Jan 2010.

[39] O. Kononova, Y. Kholodov, K. E. Theisen, K. A. Marx, R. I. Dima, F. I. Ataullakhanov*, et al.*, "Tubulin Bond Energies and Microtubule Biomechanics Determined from Nanoindentation in Silico," *Journal of the American Chemical Society,* vol. 136, pp. 17036-17045, Dec 2014.

[40] V. VanBuren, D. J. Odde, and L. Cassimeris, "Estimates of lateral and longitudinal bond energies within the microtubule lattice," *Proceedings of the National Academy of Sciences of the United States of America,* vol. 99, pp. 6035-6040, Apr 2002.

[41] J. Howard, "The movement of kinesin along microtubules," *Annual Review of Physiology,* vol. 58, pp. 703-729, 1996.

[42] M. Caplow, R. L. Ruhlen, and J. Shanks, "THE FREE-ENERGY FOR HYDROLYSIS OF A MICROTUBULE-BOUND NUCLEOTIDE TRIPHOSPHATE IS NEAR ZERO - ALL OF THE FREE-ENERGY FOR HYDROLYSIS IS STORED IN THE MICROTUBULE LATTICE," *Journal of Cell Biology,* vol. 127, pp. 779-788, Nov 1994.

[43] N. B. Gudimchuk, E. V. Ulyanov, E. O'Toole, C. L. Page, D. S. Vinogradov, G. Morgan*, et al.*, "Mechanisms of microtubule dynamics and force generation examined with computational modeling and electron cryotomography," *Nature communications,* vol. 11, p. 3765, 2020 Jul 2020.

[44] V. VanBuren, L. Cassimeris, and D. J. Odde, "Mechanochemical model of microtubule structure and self-assembly kinetics," *Biophysical Journal,* vol. 89, pp. 2911-2926, Nov 2005.

[45] J. R. McIntosh, E. O'Toole, K. Zhudenkov, M. Morphew, C. Schwartz, F. I. Ataullakhanov*, et al.*, "Conserved and divergent features of kinetochores and spindle microtubule ends from five species," *Journal of Cell Biology,* vol. 200, pp. 459-474, Feb 2013.

[46] M. Winey, C. L. Mamay, E. T. Otoole, D. N. Mastronarde, T. H. Giddings, K. L. McDonald*, et al.*, "3-DIMENSIONAL ULTRASTRUCTURAL ANALYSIS OF THE SACCHAROMYCES-CEREVISIAE MITOTIC SPINDLE," *Journal of Cell Biology,* vol. 129, pp. 1601-1615, Jun 1995.

[47] J. J. L. Miranda, P. De Wulf, P. K. Sorger, and S. C. Harrison, "The yeast DASH complex forms closed rings on microtubules," *Nature Structural & Molecular Biology,* vol. 12, pp. 138-143, Feb 2005.

[48] N. T. Umbreit, M. P. Miller, J. F. Tien, J. C. Ortola, L. Gui, K. K. Lee*, et al.*, "Kinetochores require oligomerization of Dam1 complex to maintain microtubule attachments against tension and promote biorientation," *Nature Communications,* vol. 5, p. 11, Sep 2014.

[49] S. Westermann, A. Avila-Sakar, H. W. Wang, H. Niederstrasser, J. Wong, D. G. Drubin*, et al.*, "Formation of a dynamic kinetochore-microtubule interface through assembly of the Dam1 ring complex," *Molecular Cell,* vol. 17, pp. 277-290, Jan 2005.

[50] S. Westermann, H. W. Wang, A. Avila-Sakar, D. G. Drubin, E. Nogales, and G. Barnes, "The Dam1 kinetochore ring complex moves processively on depolymerizing microtubule ends," *Nature,* vol. 440, pp. 565-569, Mar 2006.

[51] M. I. Molodtsov, E. L. Grishchuk, A. K. Efremov, J. R. McIntosh, and F. I. Ataullakhanov, "Force production by depolymerizing microtubules: A theoretical study," *Proceedings of the National Academy of Sciences of the United States of America,* vol. 102, pp. 4353-4358, Mar 2005.
[52] R. Grubbs, "Cellular Mg2+ Regulation: Role of ATP and Growth Factors," *National Science Foundation,* Aug 15 1991.
[53] A. Romani and A. Scarpa, "REGULATION OF CELL MAGNESIUM," *Archives of Biochemistry and Biophysics,* vol. 298, pp. 1-12, Oct 1992.
[54] K. Maeshima, T. Matsuda, Y. Shindo, H. Imamura, S. Tamura, R. Imai*, et al.*, "A Transient Rise in Free Mg2+ Ions Released from ATP-Mg Hydrolysis Contributes to Mitotic Chromosome Condensation," *Current Biology,* vol. 28, pp. 444-+, Feb 2018.
[55] L. Cassimeris, D. Gard, P. T. Tran, and H. P. Erickson, "XMAP215 is a long thin molecule that does not increase microtubule stiffness," *Journal of Cell Science,* vol. 114, pp. 3025-3033, Aug 2001.
[56] A. Desai, S. Verma, T. J. Mitchison, and C. E. Walczak, "Kin I kinesins are microtubule-destabilizing enzymes," *Cell,* vol. 96, pp. 69-78, Jan 1999.
[57] V. Farmer, G. Arpa, S. L. Hall, and M. Zanic, "XMAP215 promotes microtubule catastrophe by disrupting the growing microtubule end," *Journal of Cell Biology,* vol. 220, p. 13, Oct 2021.
[58] H. Girao, N. Okada, T. A. Rodrigues, A. O. Silva, A. C. Figueiredo, Z. Garcia*, et al.*, "CLASP2 binding to curved microtubule tips promotes flux and stabilizes kinetochore attachments," *Journal of Cell Biology,* vol. 219, p. 20, Feb 2020.
[59] J. W. J. Kerssemakers, E. L. Munteanu, L. Laan, T. L. Noetzel, M. E. Janson, and M. Dogterom, "Assembly dynamics of microtubules at molecular resolution," *Nature,* vol. 442, pp. 709-712, Aug 2006.
[60] J. J. Correia, L. T. Baty, and R. C. Williams, "MG-2+ DEPENDENCE OF GUANINE-NUCLEOTIDE BINDING TO TUBULIN," *Journal of Biological Chemistry,* vol. 262, pp. 17278-17284, Dec 1987.
[61] M. R. Mejillano and R. H. Himes, "BINDING OF GUANINE-NUCLEOTIDES AND MG2+ TO TUBULIN WITH A NUCLEOTIDE-DEPLETED EXCHANGEABLE SITE," *Archives of Biochemistry and Biophysics,* vol. 291, pp. 356-362, Dec 1991.
[62] N. T. Umbreit, D. R. Gestaut, J. F. Tien, B. S. Vollmar, T. Gonen, C. L. Asbury*, et al.*, "The Ndc80 kinetochore complex directly modulates microtubule dynamics," *Proceedings of the National Academy of Sciences of the United States of America,* vol. 109, pp. 16113-16118, Oct 2012.
[63] J. F. Tien, N. T. Umbreit, D. R. Gestaut, A. D. Franck, J. Cooper, L. Wordeman*, et al.*, "Cooperation of the Dam1 and Ndc80 kinetochore complexes enhances microtubule coupling and is regulated by aurora B," *Journal of Cell Biology,* vol. 189, pp. 713-723, May 2010.
[64] M. Castoldi and A. V. Popov, "Purification of brain tubulin through two cycles of polymerization-depolymerization in a high-molarity buffer," *Protein Expression and Purification,* vol. 32, pp. 83-88, Nov 2003.
[65] P. Ayaz, S. Munyoki, E. A. Geyer, F. A. Piedra, E. S. Vu, R. Bromberg*, et al.*, "A tethered delivery mechanism explains the catalytic action of a microtubule polymerase," *Elife,* vol. 3, p. 19, Aug 2014.
[66] P. Ayaz, X. C. Ye, P. Huddleston, C. A. Brautigam, and L. M. Rice, "A TOG:alpha beta-tubulin Complex Structure Reveals Conformation-Based Mechanisms for a Microtubule Polymerase," *Science,* vol. 337, pp. 857-860, Aug 2012.

Chapter 4

Kinetochores grip microtubules with directionally asymmetric strength

Manuscript in preparation

Abstract

For accurate mitosis, all chromosomes must achieve 'bi-orientation', with replicated sister chromatids coupled via kinetochores to the plus ends of opposing microtubules. However, kinetochores first bind the sides of microtubules and subsequently find plus ends by directed transport or when side-attached microtubules shorten and bring their ends to the kinetochores. Whether kinetochores possess intrinsic affinity specifically for plus ends has been unclear. We show here that isolated kinetochores bind microtubules with a strong preference for plus ends and that side-attached kinetochores are very sensitive to microtubule polarity, gripping six-fold more strongly when pulled toward plus versus minus ends. This directionally asymmetric grip correlates with changes in the axial arrangement of subcomplexes within the kinetochores, suggesting that internal architecture dictates attachment strength. We propose that the kinetochore's directional grip promotes accuracy specifically during early mitosis, by stabilizing correct attachments even before both sisters have found plus ends.

Introduction

Mitosis is driven by kinetochores, multiprotein complexes that couple chromosomes to the dynamic tips of microtubules. Accurate mitosis requires all chromosomes to become 'bi-oriented', with sister chromatids attached via their kinetochores to the plus ends of microtubules emanating from opposite poles of the mitotic spindle. But kinetochores first bind the sides of spindle microtubules[1-4] and subsequently find plus ends, either when dragged there by their sisters or by plus end-directed motor proteins,[3,5,6] or when side-attached microtubules shorten, bringing their disassembling plus ends to the kinetochore.[3,7] Once kinetochores are attached to plus ends *in vivo*, they track persistently with end growth and shortening.[7] Plus-end tracking powers anaphase, the signature event of mitosis, when sister chromatids are pulled apart.

Kinetochores also sense when they are correctly attached and, if so, they grip the microtubules stably. Conversely, if they are incorrectly attached, they release to give another chance for proper attachments to form.[8-10] When sister kinetochores attach correctly to microtubules from opposite spindle poles, they come under tension, whereas sisters attached incorrectly to microtubules from the same pole lack tension. The selective stabilization of correct, tension-bearing attachments is the fundamental basis for mitotic accuracy. Mechanisms proposed to explain it have focused primarily on plus-end attachments.[9-11] Aurora B kinase is thought to selectively release plus-end attachments that lack tension,[12] whereas the higher tension on correct plus-end attachments is thought to protect them from Aurora B.[13] A catch bond-like behavior can also stabilize tension-bearing plus-end attachments directly, independent of kinase-based regulation.[14] Thus, plus-end attachments are not only key for generating chromosome movements during mitosis, but also for error correction.

Microtubules are protein polymers composed of αβ-tubulin subunits packed together in a head-to-tail fashion, with each subunit oriented identically along the entire length of each filament.[15] Their structural polarity confers directionality to motor proteins, and it makes the two ends of a microtubule different: β-tubulin is exposed at plus ends, and α-tubulin is exposed at minus ends. Plus ends are faster-growing and

more dynamic.[16] The αβ-tubulin subunits adopt a straight configuration when embedded in the wall of a microtubule,[17] but at either end of a growing or shortening microtubule, the subunits are often curved.[18,19] Growing ends are 'capped' by newly added subunits that carry GTP, which is hydrolyzed to GDP after assembly into the microtubule wall.[15] Given how fundamental plus end attachments are for mitosis, kinetochores might possess an intrinsic, preferential affinity specifically for microtubule plus ends. This idea has not been rigorously tested, however, in part because of the difficulty of disentangling the intrinsic properties of kinetochores from other, indirect influences that can affect their behavior *in vivo*.

Kinetochores isolated from budding yeast[14] are ideal for studying the intrinsic behaviors of kinetochores *in vitro*. Their composition and function are well conserved, they are the simplest known (assembling on a single centromeric nucleosome[20,21] and attaching to a single microtubule[22]), and they are amenable to genetic and biochemical manipulation. The kinetochores of *S. cerevisiae* contain three main types of microtubule-binding elements.[23] The primary microtubule binder is the Ndc80 complex (Ndc80c), a flexible protein fibril with a globular 'foot' (calponin-homology) domain that binds with a stereospecific 'footprint' on the outside surface of the microtubule.[24-28] Multiple Ndc80c fibrils decorate the centromeric nucleosome and recruit numerous Dam1 complexes that strengthen their attachment to the microtubule. (The human Ska complex serves an analogous function.[29]) The Dam1 complexes can assemble into rings encircling the microtubule,[30-32] potentially organizing the kinetochore into a cage-like arrangement surrounding the plus end.[33,34] Also recruited to Ndc80c are microtubule-binding TOG-family proteins, such as Stu2[35,36] (chTOG in humans[37]). Ndc80c itself has no special affinity for the microtubule tip.[38] However, some evidence suggests that Dam1c might have a preference for the GTP-containing αβ-tubulin subunits that cap growing tips,[30,39] and Stu2's TOG domains bind curved αβ-tubulin,[40] which is found specifically at microtubule ends. Thus, various potential mechanisms could confer a plus-end preference to the kinetochore. Motors can also interact with kinetochores *in vivo* and actively transport them along the sides of microtubules toward the ends.[3,5,6]

Laser trapping has enabled direct studies of the coupling between isolated kinetochores and dynamic microtubule tips *in vitro*.[13,14,35] Native kinetochore particles are first purified and then linked to polystyrene microbeads. The kinetochores often bind initially to the sides of individual microtubules, and 0.5 to 3 pN of laser trap tension can then be applied to drag them to the plus ends. Once at plus ends, the kinetochores track persistently with plus end growth and shortening, mimicking their behavior *in vivo*. Notably, however, plus end-tracking *in vitro* requires continuous external tension. If tension is removed (e.g., by shuttering the laser trap), a kinetochore-decorated bead usually 'parks' on the microtubule wall, staying attached to a fixed point on the lattice while the plus end grows past it. This requirement for external tension suggests that kinetochores might lack any intrinsic plus end preference and that their persistent plus end tracking *in vivo* might depend strictly on the tension exerted by their sisters on the other side of the bipolar spindle, or on interactions with plus end-directed motors. Alternatively, an intrinsic plus end preference might exist but escape detection, either because an effective test has not yet been devised, or because during kinetochore purification a component required for the preference is inadvertently lost.

Here we show that isolated kinetochores do possess a strong, intrinsic preference for plus ends. Single molecule fluorescence microscopy reveals that individual kinetochores assembled *de novo* in whole cell extracts capture microtubules overwhelmingly by their plus-ends. Laser trap experiments show that native kinetochore particles attach dynamic microtubule tips with a substantially higher strength at plus ends than at minus ends. Strikingly, the kinetochores also grip the sides of microtubules with highly

direction-dependent strength, indicating an intrinsic sensitivity to the structural polarity of the microtubule wall. Sub-diffraction localization of fluorescent-tagged kinetochore subcomplexes indicates that plus end-attached kinetochores are organized with DNA- and microtubule-binding subcomplexes separated along the microtubule axis, matching the physiological arrangement during metaphase. However, side-attached kinetochores adopt a more compact axial arrangement specifically when they are pulled toward a minus end. These observations suggest that both the plus end preference and the directionally asymmetric grip of the kinetochore arise from its asymmetric architecture. The kinetochore's asymmetric grip is similar to the directional binding of actin filaments by vinculin,[41] talin,[42] and α-catenin,[43] behaviors which are thought to stabilize the attachment of appropriately oriented F-actin to focal adhesions.[44,45] We propose that the directionally asymmetric grip of the kinetochore stabilizes its attachment to correctly oriented microtubules specifically during early mitosis, even before both sisters have found plus ends.

Results

Individual kinetochores including outer microtubule-binding subcomplexes assemble *de novo*

We recently showed that assembly of kinetochores *de novo* in yeast cell lysates can be directly observed at the single molecule level using total internal reflection fluorescence (TIRF) microscopy.[46] Our approach revealed molecular requirements for the wrapping of centromeric DNA around the centromere-specific histone H3 variant, Cse4 (Cenp-A), which creates the chromosomal foundation for the kinetochore. However, the extent of recruitment of microtubule-binding kinetochore elements and their functional attachment to microtubules remained unexplored.

To measure the recruitment of microtubule-binding elements onto single centromeric DNAs, we tethered 180-bp Atto565-labeled DNAs sparsely onto passivated coverslip surfaces through avidin-biotin linkages. The surface-tethered centromeric DNAs were then incubated for an hour with lysate from a yeast strain harboring an endogenous GFP tag fused to the C-terminus of Ndc80 (Figure 1A and 1B). After incubation, the lysate was washed away, multi-wavelength TIRF images were collected, and colocalization single molecule spectroscopy (CoSMoS) was performed.[46-49] In addition to the wild type DNA construct, we tested assembly on a negative control mutant DNA (Figure 1s1) containing a three base pair substitution that eliminates centromere function *in vivo*[50-52] and *in vitro*.[53] The fraction of wild type centromeric DNA molecules that were decorated with Ndc80-GFP was 3.8 ± 2.3% (Figure 1C). Analysis of photobleaching suggested that many of these assemblies carried multiple copies of Ndc80-GFP (Figure 1s2). We also imaged assemblies after incubation with lysates from strains harboring the inner-kinetochore proteins, Ndc10-GFP (part of the DNA-binding Cbf3 complex), Cse4-GFP (part of the centromeric nucleosome), and Ctf19-GFP (part of the constitutive centromere-associated network, or CCAN) (Figure 1A and 1B). As we previously reported,[46] *de novo* assembly of the inner kinetochore was highly efficient, with 28 ± 1%, 40 ± 1%, and 12 ± 1% of centromeric DNAs recruiting Ndc10-GFP, Cse4-GFP, and Ctf19-GFP, respectively (Figure 1C). By contrast, no more than 0.1% of the negative control mutant centromeric DNAs colocalized with Ndc10-GFP or Cse4-GFP (Figure1s1). These observations confirm the specificity of our single molecule kinetochore assembly assay and demonstrate that about one in twenty-five assemblies recruits microtubule-binding elements. Considering that many hundreds of individual assemblies can be observed in a single field of view, this level of efficiency was sufficient to enable functional, microtubule-binding behaviors of the individual kinetochore assemblies to be studied.

Assembled kinetochores capture microtubules with a strong preference for plus ends

We tested for microtubule-binding activity by introducing taxol-stabilized Alexa Fluor 647-labeled microtubules after kinetochore assembly in lysate (Figure 1D). The individual assembled kinetochores readily captured single microtubules. Capture was specific to the kinetochores and did not occur in negative controls with non-functional mutant centromeric DNAs (Figure 1s3). The kinetochores often captured microtubules by their tips (Figure 1D, Video s1), which colocalized with the fluorescence from Ndc80-GFP (Figure 1D). In this tip-attached arrangement, the distal ends of the microtubules swiveled freely by Brownian motion, exploring a hemispherical space above the coverslip. Some kinetochores captured microtubules by their sides. The Brownian movement of these side-captured microtubules was more restricted. Rotation occurred mainly in a plane parallel to the coverslip, swiveling in a propeller-like fashion (Figure 1D, Video s2) with Ndc80-GFP located at the axis of rotation (Figure 1D). These observations show that individual *de novo* assembled kinetochores can capture the tips and the sides of microtubules, and they demonstrate flexibility in the tethering of the kinetochores to the coverslip.

To test for preferential plus-end binding, we generated polarity-marked microtubules by growing dimly fluorescent plus-end extensions from brightly fluorescent seeds[54,55] and stabilizing them with taxol. We then assembled surface-tethered kinetochores, incubated them with the polarity-marked microtubules, and quantified the fraction of microtubules that were captured by plus versus minus ends (Figure 2A). For clear viewing, we applied a gentle flow of buffer to keep the kinetochore-attached microtubules parallel to the coverslip and in the plane of focus. More than 82% of tip-bound microtubules (162 out of 196 microtubules examined across eight technical replicates) were captured by their plus ends (Figure 2A). This preference was not an artifact of differential labeling (Figure 2s1). It was observed in the absence of motor proteins,[53] ATP, and microtubule dynamics, implying that kinetochores themselves have a strong intrinsic affinity for features specific to microtubule plus ends.

Plus end attachments support more tension than minus end attachments

Kinetochores *in vivo* sustain tension almost continuously once they are properly end-attached,[56] so their load-bearing capacity is important for function. We therefore wondered whether the plus-end binding preference uncovered in our TIRF experiments would affect a kinetochore's load-bearing capacity. Using a laser trap, we measured the rupture strengths of native kinetochore particles isolated from yeast lysate via FLAG immunoprecipitation.[14] As in our prior work, the native kinetochores were conjugated sparsely to polystyrene microbeads and then attached near the tips of individual dynamic microtubules growing from coverslip-anchored seeds. After an initial preload tension of ~1 pN was used to slide a kinetochore-bead to the end of a microtubule, the pulling force was gradually increased (at 0.25 $pN \cdot s^{-1}$) until the kinetochore detached from the microtubule (Figure 2B). Plus and minus ends were readily identifiable in these experiments because the plus ends grew faster, extending farther from the coverslip anchored seeds than the minus ends. The distribution of rupture strengths measured at plus ends was very similar to our previous measurements,[14,35] with a mean strength of 9.7 ± 1.0 pN (mean ± SEM from N = 43 plus-end attachments) (Figure 2C). Strengths measured at minus ends were substantially weaker, with a three-fold lower mean strength of only 3.3 ± 0.5 pN (N = 26 minus-end attachments; $p = 2\times10^{-5}$, based on a K-S test) (Figure 2C). In many instances, it was possible to sequentially measure the rupture strength of a single kinetochore-decorated bead at both ends of a microtubule. Irrespective of the order of these measurements, minus-end first or plus-end first, the strength was always higher at the plus end (Figure 2C). This control confirms the differential strength and also the reliability of our identification of plus versus minus ends. Altogether, the rupture strength measurements show that attachments of

kinetochores to microtubule plus ends can bear substantially more tension than attachments to minus ends.

Kinetochores grip microtubule sides with direction-dependent strength

Before achieving proper plus end attachments *in vivo*, kinetochores initially bind the sides of microtubules.[1-4] This physiological behavior is also seen in our laser trap assays with isolated kinetochores. Modest amounts of laser trap tension, 0.5 to 3 pN, will cause these side-attached kinetochores to slide toward the ends. Often, it seems easier to detach side-attached kinetochores from microtubules by sliding them toward minus ends. This anecdotal observation, together with the large strength difference between plus versus minus end attachments, led us to hypothesize that side-attachments might exhibit a polarity preference. To test this idea, we used laser trapping to measure the friction between side-attached kinetochores and microtubules.

Microbeads decorated sparsely with native kinetochores were attached to the sides of individual, dynamic microtubules, growing (as described above) from coverslip-anchored seeds. Constant pulling forces between 0.5 and 3 pN were applied parallel to the microtubule axis, and the speeds at which the kinetochore-decorated beads slid along the microtubule were quantified. The direction of force was periodically reversed, to assess friction in both directions relative to microtubule polarity (Figures 2D, 2E, and 2s2). For every bead-microtubule pair examined, sliding toward the plus end was markedly slower than toward the minus end. Under 1 pN of laser trap tension, the average sliding speeds toward plus versus minus ends differed six-fold (109 ± 11 nm·s^{-1} versus 635 ± 79 nm·s^{-1}; mean ± SEM from *N* = 75 and 81 sliding events, respectively, across 24 microtubule-bead pairs) (Figure 2F). Sliding speeds generally increased with force, as expected for protein friction.[57] To compare friction across many bead-microtubule pairs, measured at different forces and on different microtubule extensions, we divided the applied force, F, by the mean sliding speed, v, to compute a frictional drag coefficient, $\gamma = F \cdot v^{-1}$. The frictional drag during plus end-directed sliding was uniformly higher, independent of whether beads were tested on the shorter microtubule extensions (where plus end-directed sliding was toward the coverslip-anchored seeds), or on the longer extensions (where plus end-directed sliding was toward free microtubule ends) (Figure 2G). This control confirms that the speed difference arises from microtubule polarity, rather than from asymmetric anchorage of the microtubule to the coverslip. Altogether, these observations indicate that kinetochores grip the sides of microtubules with a strength that differs markedly depending on the direction of applied force relative to the polarity of the microtubule substrate.

Assembled kinetochores recapitulate *in vivo* architecture when attached to microtubule plus ends

To understand the basis for direction-sensitivity, we sought to examine the architecture of the isolated kinetochores. When kinetochores are properly attached to microtubule plus ends *in vivo*, their molecular components are spatially organized. Fibrillar Ndc80 complexes align with the microtubule axis, DNA-binding 'inner' kinetochore elements are oriented toward plus ends, and 'outer' microtubule-binding elements project toward minus ends and spindle poles.[58-60] To examine the configuration of kinetochores assembled *de novo*, we mapped the relative positions of specific fluorescent-tagged kinetochore components along the microtubule axis by locating their centers of fluorescence. As described above, Ndc80-GFP kinetochores were assembled onto Atto565-labeled DNAs and exposed to taxol-stabilized, Alexa Fluor 647-labeled microtubules. A gentle flow of buffer aligned kinetochore-attached microtubules with the plane of the coverslip (Figure 3A). We oscillated the flow direction, causing the microtubules to flip back and forth, reorienting their long axes by 180° with each reversal of the flow (Figures 3B and 3C).

The attached kinetochores also reoriented together with the microtubules, allowing us to measure distances from specific fluorescent-tagged kinetochore components to the tether point on the coverslip surface with nanometer accuracy. Initially, we focused on kinetochores that had captured microtubules by their ends.

When a kinetochore periodically reoriented with the flow, the fluorescent marker on its centromeric DNA was displaced from the tether point on the coverslip by 16 ± 1 nm on average (Figures 3D and 3E; mean ± SEM from *N* = 74 measurement intervals across 13 end-attached kinetochores). This distance is much shorter than would be expected for a straight B-form DNA helix of 180 bp (~61 nm), presumably because the centromeric DNA, after kinetochore assembly, was tightly wrapped around a centromeric nucleosome. Consistent with this interpretation, the histone H3 variant Cse4-GFP was located 12 ± 1 nm from the tether (mean ± SEM, *N* = 67 intervals, 9 kinetochores), very close to the centromeric DNA marker. The microtubule-binding component Ndc80-GFP was 37 ± 1 nm from the tether (*N* = 116 intervals, 19 kinetochores), implying that its C-terminal GFP tag was located ~25 nm outward from the nucleosome (Figures 3D and 3E). Considering where the GFP tag falls within the structure of the Ndc80 complex,[61-63] this 25-nm distance suggests the Ndc80c fibrils were well aligned with the microtubule axis. Dam1-GFP, a component of the outer, microtubule-binding Dam1 complex, was located 65 ± 2 nm from the tether (*N* = 128 intervals, 22 kinetochores) (Figures 3E and 3s1). This relatively large distance further suggests axial alignment of Ndc80c fibrils because the Dam1 complex binds nearer to the N-terminus of Ndc80.[32,64] The implied intra-kinetochore separation between the C-termini of Ndc80 and Dam1 was 28 nm, a distance indistinguishable from the intra-kinetochore separation measured previously in budding yeast during metaphase.[58] Altogether, these observations show that when *de novo* assembled kinetochores are attached to microtubule plus ends, they are spatially organized in a configuration that closely resembles the molecular arrangement of plus end-attached kinetochores during metaphase *in vivo*, with DNA-binding subcomplexes proximal to the chromatin and microtubule-binding subcomplexes projecting distally, toward minus ends.[58,65,66]

Kinetochore architecture is less organized when attached to the sides of microtubules

The molecular organization of side-attached kinetochores has scarcely been explored. By mapping the relative positions of centromeric DNA and Ndc80-GFP within kinetochores that captured microtubules by their sides, we were able to examine the molecular arrangement of side-attached kinetochores and compare them directly to end-attached kinetochores, often measured simultaneously on the same coverslips. We focused on kinetochores that captured the sides of microtubules in an off-center arrangement (Figures 4A and 4B), where the two microtubule segments extending away from the kinetochore had unequal lengths. The longer segment experienced higher viscous drag forces and therefore oriented reliably downstream in the flow. The axial positions of fluorescent-tagged centromeric DNA and Ndc80-GFP within these side-attached kinetochores was tracked in the same manner as for end-attached kinetochores (Figure 4C). The distance from the centromeric DNA marker to the tether point on the coverslip was indistinguishable from that measured for end-attached kinetochores (Figures 4D and 4E). The distribution of Ndc80-GFP distances, however, was wider in comparison to the end-attached kinetochores and apparently bimodal, including an elongated sub-population with a mean distance of 39 ± 4 nm and a compact sub-population much closer to the tether with a mean distance of only 18 ± 9 nm (± SEM, *N* = 54 and 33 intervals, respectively, 13 side-attached kinetochores) (Figure 4E). This observation shows that the molecular architecture of side-attached kinetochores differs from end-attached kinetochores, with Ndc80 fibrils often less well aligned to the microtubule axis. Depending on which end

of the microtubule was oriented downstream in the flow, the side-attached kinetochores experienced viscous pulling forces directed either toward the minus end or toward the plus end. We hypothesized that the two sub-populations, with elongated or compact Ndc80-GFP, might correspond to these two different pulling directions. To test this idea we repeated the Ndc80-GFP distance measurements using polarity-marked microtubules. As predicted, when side-attached kinetochores were pulled toward minus ends Ndc80-GFP was closer to the tether, at a distance of only 24 ± 3 nm (*N* = 46 intervals, 12 kinetochores), and when they were pulled toward plus ends Ndc80-GFP was farther from the tether, at a distance of 39 ± 4 nm (*N* = 34 intervals, 7 kinetochores). These measurements demonstrate that the direction of external force directly influences kinetochore architecture, with Ndc80 fibrils adopting a more compact arrangement specifically when the kinetochore is pulled toward the minus end.

Discussion

Given the vital importance of plus-end attachments for chromosome segregation, an attractive idea has been that kinetochores possess an intrinsic preference for plus ends over other regions of the microtubule. Various purified kinetochore subcomponents bind preferentially to curved tubulin[40,67,68] or GTP caps.[30] However, whether these behaviors confer a plus end preference to the kinetochore as whole is unclear. Our isolated kinetochores captured microtubules with a strong preference for plus ends and their attachment strength was higher at plus ends than at minus ends. We can exclude a role for active motors in these behaviors because our kinetochores lacked motors[14,53] and ATP was absent from our experiments. Our capture assays used filaments stabilized by taxol and GMPcPP, indicating that preferential plus end capture does not require GTP caps or microtubule dynamics, and probably does not require curved tubulin since the ends of GMPcPP microtubules are usually blunt.[69] Moreover, we found that side-attached kinetochores were sensitive to microtubule polarity even far away from the ends of the filaments. We propose that all three of these intrinsic kinetochore behaviors – their preference for capturing and holding microtubule plus ends, and their directionally asymmetric grip when side-attached – arise from the structural polarity of the microtubule and how it influences kinetochore architecture.

Ndc80c binds microtubules partly through a stereospecific 'footprint', which presumably cannot twist or rotate without breaking its bond to the microtubule. The stalk of Ndc80c emerges from the foot (from the calponin-homology domains) with a tilt toward the microtubule plus end.[27,34,70] This local structural asymmetry could set up the asymmetric mechanical behavior of the whole kinetochore. When a side-attached kinetochore is pulled toward the plus end, its Ndc80c feet might bind more strongly. When pulled toward the minus end, its feet might bind more weakly. After emerging asymmetrically from the foot, the Ndc80c stalk contains a flexible 'hinge',[63,71,72] which should allow the rest of the stalk to align at least partially with the direction of external force. Pulling a kinetochore toward the plus end could align its multiple Ndc80c stalks into a parallel configuration that facilitates interactions with Dam1c oligomers, strengthening the overall grip of the kinetochore on the microtubule. At a plus end, the stalks could all project past the tip of the microtubule and converge onto the centromeric nucleosome,[34] allowing Dam1c oligomers to organize a cage-like arrangement surrounding the tip[33,34] with even higher grip strength. We propose that pulling a kinetochore toward the minus end disrupts this organization, weakening its grip when side-attached, and also precluding strong attachment to the minus end. Consistent with this view, isolated kinetochores attached to plus ends are organized with Ndc80c fibrils oriented along the microtubule axis and projecting toward the minus end, matching the physiological arrangement of tip-attached kinetochores in metaphase cells.[58-60] Side-attached kinetochores are less organized, adopting a more compact axial arrangement specifically when pulled toward minus ends.

Independent of the molecular underpinnings, the directionally asymmetric grip of the kinetochore suggests a mechanism for promoting accuracy early in mitosis. For accurate segregation, sister kinetochores must attach to the plus ends of microtubules emanating from opposite poles; however, they first bind the sides of the filaments and subsequently find plus ends, either through active transport or microtubule disassembly. Side-binding facilitates microtubule capture because a much greater surface area is available to kinetochores along the sides than at the ends of the microtubules. However, the mechanisms proposed to explain the fidelity of sister bi-orientation have focused almost exclusively on plus end-attachments, and how these are selectively released when sisters attach incorrectly to microtubules from the same pole. We propose that the directionally asymmetric grip strength we discovered here promotes bi-orientation even earlier in mitosis, before both sisters have achieved plus end-attachments, in the following manner: In prometaphase, sister kinetochores are exposed to many spindle microtubules emanating from both poles. After a pair of sister kinetochores initially makes side-attachments, one of them will (by chance) become tip-attached before the other, tracking with tip shortening and exerting elastic pulling forces on its side-attached sister. If the pair is attached *incorrectly* to microtubules from the same pole, then the side-attached sister will be pulled toward the minus end. Its grip will therefore be weak, and it will likely detach. Conversely, if the pair is attached *correctly* to microtubules from opposite poles, then the side-attached sister will be pulled toward the plus end. It will therefore have a stronger grip that should allow it to remain attached and achieve proper bi-orientation at the plus end. The greater frictional resistance of the correctly side-attached sister will also cause the end-attached sister to experience higher tensile forces, stabilizing its attachment by the catch bond-like effect we previously discovered,[14] and protecting it from Aurora B kinase-triggered detachment.[13] Thus the asymmetric grip of the side-attached sister can selectively stabilize correct over incorrect arrangements in multiple ways. Notably, the directionally asymmetric grip of the kinetochore is similar to the recently discovered directional binding of F-actin by focal adhesion proteins,[41-43] suggesting that asymmetric gripping might represent a general mechanism for selective retention of filaments with correct orientations at cytoskeletal junctions in many cellular contexts.

Materials and Methods

Yeast strain construction

All strains described in this study are derivatives of SBY3 (W303). Generation of *Saccharomyces cerevisiae* strains harboring GFP tagged kinetochore proteins and a phosphomimetic mutation in Dsn1 (Dsn1-2D) that has been shown to enhance outer kinetochore assembly[53,73] was achieved either by standard genetic crosses and media selection[74] or using standard PCR-based integration at the endogenous loci.[75] All yeast transformants were confirmed by PCR or sequencing. Plasmids and primers used to generate yeast strains are listed in Supp Table X1. All yeast strains used in this study are listed in Supp Table 2.

Preparation of yeast whole cell lysates

Yeast whole cell lysates used for *de novo* kinetochore assembly were prepared as previously described.[46,53] Cells were grown in 2 L of liquid yeast peptone dextrose (YPD) media at room temperature and harvested in log phase by centrifugation. Cell pellets were placed on ice and washed with ice cold dH_20 plus 0.2 mM PMSF and centrifuged. Pellets were washed a second time with ice cold Buffer L (25 mM HEPES pH 7.6, 2 mM MgCl2, 0.1 mM EDTA, 0.5 mM EGTA, 0.1% NP-40, 175 mM K-Glutamate, and 15% Glycerol) plus 2 mM DTT and protease inhibitors (10 µg/mL leupeptin, 10 µg/mL pepstatin, 10 µg/mL chymostatin, and 10 µM PMSF) and centrifuged again. Cells were resuspended in a final volume of Buffer L given by $u = v \cdot o$,

where u represents the volume in µL of added Buffer L, v represents the original volume in mL of the liquid culture, and o represents the optical density of the culture measured at the time of harvest. The cellular resuspension was snap frozen as small spherical pellets by pipetting drops of the suspension directly into liquid nitrogen. Cell lysis was achieved using a Freezer/Mill (SPEX SamplePrep) by alternating milling of the pellets at 10 Hz for 2 minutes followed by a 2-min cooling phase for ten cycles. The resulting lysate powder was then thawed on ice and clarified by centrifugation at 16,100 g for 30 minutes at 4˚C. The protein-containing supernatant was subsequently aliquoted (100 µL) and snap frozen in liquid nitrogen. Aliquots were stored at -80˚C until use.

Preparation of CEN DNAs

180 base pair Atto565 CEN^{WT} and CEN^{mut} DNA were generated by PCR from plasmids pSB963 and pSB972 (Supplemental table X), respectively. CENmut DNA contained a three base pair substitution in the CDEIII region of CEN3 that blocks kinetochore assembly in vivo50-52 and in vitro.53 The forward 5' primer contained a 5' biotin for attachment to the PEG/biotin-PEG passivated coverslip and the reverse primer was labeled with Atto565 (Supplemental table 3). PCR products were purified using a Qiagen PCR Cleanup kit and eluted into dH20.

Preparation of taxol stabilized microtubules

Purified bovine brain tubulin was added to microtubule polymerization buffer [1x BRB80 (80 mM PIPES, 1 mM MgCl2, 1 mM EGTA), 7% DMSO, 4 mM $MgCl_2$, and 1 mM GTP] to a final concentration of 2 mg/mL and incubated at 37˚C for 1 hr. After 1 hour, 3 µL of pre-warmed 1x BRB80 + 10 µM taxol was added for every 1 µL of polymerized microtubules. Taxol stabilized microtubules were then spun for 10 min at 90,000 RPM (TLA100.0, Beckman Optima MAX-XP) at 37°C. The microtubule pellet was resuspended in 150 µL of 1x BRB80 + 10 µM taxol and stored at room temperature. To generate fluorescent or biotinylated microtubules, porcine HyLite 488, HyLite 647, or biotin tubulin (Cytoskeleton) were added (6% w/w) to the polymerization reaction.

Slide passivation for single molecule TIRFM

Slides were prepared as previously described (Crawford et al., 2008). Coverslips and slides were plasma cleaned for 10 min followed by four sequential hour-long sonications in 2% Micro-90, 200 proof ethanol, 1 M KOH, and finally Milli-Q water. Slides and coverslips were then completely dried using ultrapure nitrogen. After drying, slides and coverslips were treated with Vectabond (Vector Laboratories) dissolved in acetone (1% v/v) for 5-10 min. Slide chambers were constructed by sandwiching the coverslip and slide together with double-sided tape. Passivation was achieved by adding a 1:100 Biotinylated mPEG-SVA/mPEG-SVA MW 5000 in 0.1 M sodium bicarbonate (1% w/v). Chambers were incubated with PEG overnight at room temperature.

Kinetochore assembly and microtubule capture assays

Excess mPEG solution was washed out with 400 µL of 1x BRB80 and then blocked with a 0.1 mg/mL BSA solution for 5 min. The chamber was then washed with 200 µL of 1x BRB80. After blocking, a solution of 0.3 mg/mL avidin was added to the chamber for 5 min and washed with an additional 200 uL of 1x BRB80. Following the addition of avidin, 50-200 pM biotinylated Atto565 CEN DNAs were introduced into the chamber and incubated for 5 min. Excess DNA was washed away with 200 µL of 1x BRB80. To assemble surface tethered kinetochores, 100 µl of yeast whole cell lysate was added to chambers with surface

tethered CEN DNAs and incubated for 1 hr. For colocalization assays, the lysate was washed away with 400 µL of 1x BRB80 with glucose oxidase (165 U/mL)/catalase (217 U/mL) and 0.65% glucose (w/v) for scavenging oxygen. For microtubule pulldown assays, taxol-stabilized microtubules were diluted 1:3 in BRB80 + 10 µM taxol and briefly sheared using a vortexer for 25 s before introduction to the slide chamber. After a 15-min incubation, excess microtubules were washed away with 400 µL of 1x BRB80 with glucose oxidase/catalase.

Single molecule colocalization analysis

All images were collected on a custom TIRF microscope built on a standard Nikon TE inverted microscope base.[76] Excitation of fluorescent proteins and organic dyes was achieved using expanded beams from three solid-state lasers at 488 nm (Coherent Sapphire), 561 nm (Coherent Sapphire) and 641 nm (Coherent Cube). Images were acquired with three separate Andor iXon897+ EMCCD cameras. For colocalization assays, 20-60 frames were collected with 0.5 second integrations. Analysis was done using custom Labview (National Instruments) software. Spot picking for each fluorescent channel was achieved using methods detailed in ref [77], and ref [78]. Mapping between color channels was done by creating a linear registration map using blue/green/orange/dark red 500 nm beads (Tetraspec, T7281) as fiducials.

Preparation of polarity marked microtubules

To produce polarity marked microtubules, two seed mixes were prepared on ice: a bright seed mix (13.3 µM unlabeled bovine tubulin, 6.7 µM Hilyte 647 tubulin, 1 mM DTT, 1 mM GMPcPP, 1x BRB80) and a dim seed mix (9 µM unlabeled bovine tubulin, 1 µM HyLite 647 cytoskeletal tubulin, 8 µM NEM-treated bovine tubulin, 1 mM DTT, 1 mM GMPcPP, 1x BRB80). Each seed mix was clarified using an ultra-centrifuge (Beckman Optima MAX-XP, 90,000 RPM, 4°C, 5 min) then snap-frozen in small aliquots and stored at -80°C. Bright seeds were polymerized by diluting an aliquot of bright seed mix 20% (vol/vol) in 1x BRB80 with 1 mM DTT. Diluted bright seed mix was then incubated for 45 min at 37°C to allow for polymerization. To grow dim elongations from the bright seeds, an aliquot of dim seed mix was diluted 17.6% (vol/vol) in 1x BRB80 with 1 mM DTT on ice, then warmed for 20 s at 37°C. Polymerized bright seeds were added 22.7% (vol/vol) to the dim mix and incubated for 1 hr at 37°C. After the second polymerization with the dim seed mix, the microtubules were centrifuged for 5 min at 22,000 RPM (TLA100.0, Beckman Optima MAX-XP) at 37°C. The pellet was then resuspended in 150 µL assembly assay buffer (1xBRB80, 1 mM DTT, 0.025 mg/mL K-casein, 20 µM taxol).

Tracking kinetochore subunit displacements and estimating intra-kinetochore distances

Custom flow chambers with an attached reservoir to hold excess buffer and custom-made fitting were designed to generate a gentle oscillating flow (0.6 mL/min) to orient surface assembled kinetochore/microtubule pairs along the coverslip surface. The fitting was attached to a syringe pump (Kd Scientific, 780210) with a flow rate of 0.6 mL/min. The volume of each oscillation was 0.2 mL. Images were acquired in the same manner used during the colocalization assays with the exception of using 0.2 second integrations instead of 0.5 second integrations. The number of frames collected was determined by the bleach rate of GFP for the individual kinetochores. Particle tracking was done using the MOSAICsuite 2D particle tracker plugin for ImageJ.[79] Analysis of particle displacements was achieved using custom scripts in IgorPro (Wavemetrics).

Rupture force assay

Rupture force assays were carried out as previously described.[14,35] Dynamic microtubules were grown from biotinylated-GMPCPP seeds on biotinylated-BSA passivated coverslips in microtubule growth buffer (BRB80, 1 mM GTP, 250 µg/mL glucose oxidase, 25 mM glucose, 30 µg/mL catalase, 1 mM DTT, 24 µM purified bovine brain tubulin, 0.5 mg/mL κ-casein). Anti-HIS antibody (R&D systems, BAM050) coated polystyrene beads were prepared as previously described.[39] The beads were decorated with native purified Dsn1-6HIS-3Flag kinetochores, and bound to dynamic plus or minus end microtubule tips. A feedback-controlled laser trap was used to apply increasing force to tip bound kinetochore decorated beads in the direction of microtubule assembly. The applied force was increased at a constant rate of 0.25 pN/s until the bead detached from the microtubule tip or the force exceeded the limit of the laser trap. Bead position was recorded using custom LabView software and analyzed to determine the rupture force with custom scripts in IgorPro. The longest extension from the GMPcPP seeds was designated as the plus end, and the shorter extension was designated as the minus end of the microtubule.

Drag force assay

Microtubules were polymerized as described above with the addition of a ten-minute incubation with growth buffer containing 24 µM tubulin to allow for minus end extensions to grow enough for bead binding along the microtubule side. The laser trap was then used to apply a constant force in one direction along the longitudinal axis of the microtubule for a short distance before reversing the direction of the applied force. This was repeated several times at forces varying from 0.5 to 4 pN on both the minus and plus end extension of the microtubules. Velocity analysis was done using custom scripts in IgorPro.

Figures

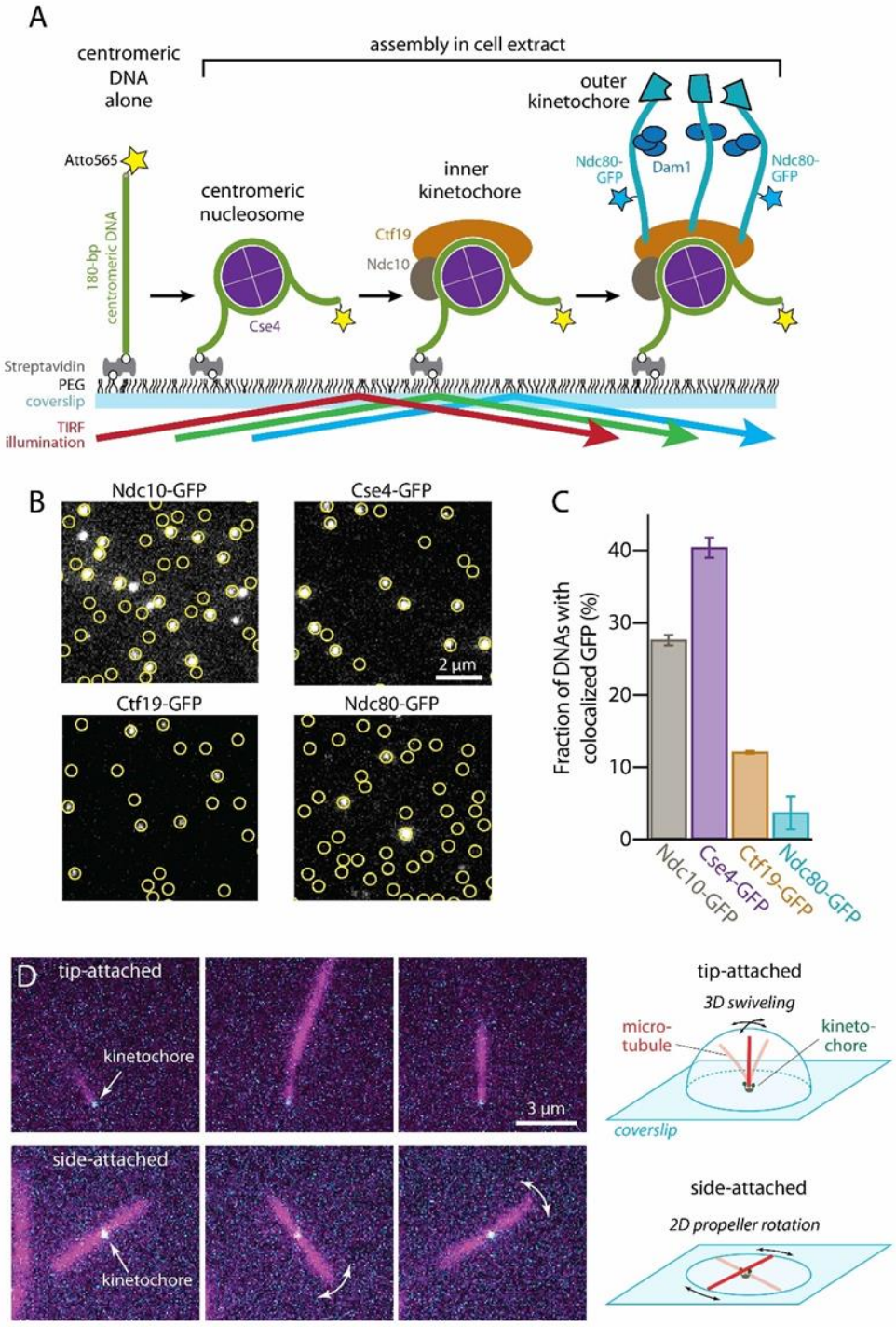
A
centromeric DNA alone
assembly in cell extract
outer kinetochore
Atto565
180-bp centromeric DNA
centromeric nucleosome
inner kinetochore
Ndc80-GFP
Dam1
Ndc80-GFP
Ctf19
Ndc10
Cse4
Streptavidin
PEG
coverslip
TIRF illumination
B
Ndc10-GFP
Cse4-GFP
2 µm
Ctf19-GFP
Ndc80-GFP
C
Fraction of DNAs with colocalized GFP (%)
40
30
20
10
0
Ndc10-GFP
Cse4-GFP
Ctf19-GFP
Ndc80-GFP
D
tip-attached
kinetochore
3 µm
side-attached
kinetochore
tip-attached
3D swiveling
micro-tubule
kineto-chore
coverslip
side-attached
2D propeller rotation

Figure 1. Individual kinetochores assembled *de novo* onto centromeric DNAs capture microtubules. **A)** Schematic of the *in vitro* kinetochore assembly assay. Individual Atto565-labeled centromeric DNAs were tethered sparsely onto a polyethylene glycol (PEG) passivated coverslip surface through biotin-avidin linkages. The surface-tethered DNAs were then incubated for 60 min with yeast whole cell lysate derived from strains with GFP-tagged kinetochore components (Ndc10, Cse4, Ctf19, or Ndc80). Kinetochores assembled spontaneously onto the centromeric DNAs and were then imaged with total internal reflection fluorescence (TIRF) microscopy after washing out the extract. **B)** Kinetochore subcomplexes colocalized with wild type centromeric DNAs. Locations of Atto565-labeled centromeric DNAs (yellow circles) were mapped onto images of GFP-tagged kinetochore subcomplexes (white spots). Scale bar, 2 μm. **C)** Percentages of centromeric DNAs that colocalized with a GFP signal from indicated kinetochore proteins. Bars show average colocalization ± SEM calculated from N > 3,400 DNAs for each kinetochore component from at least 9 fields of view recorded across three independent experiments. **D)** Assembled Ndc80-GFP kinetochores (cyan) readily captured Alexa647 microtubules (magenta) by their tips (top row of images), and sometimes by their sides (bottom row). Tip-captured and side-captured microtubules were easily distinguished by the relative locations of the kinetochore GFP spots and by the Brownian movement of the filaments. The distal ends of tip-captured microtubules swiveled freely in three dimensions (3D), exploring a hemispherical space above the coverslip. Side-captured microtubules mainly rotated in a two-dimensional (2D) plane parallel to the coverslip, in a propeller-like fashion.

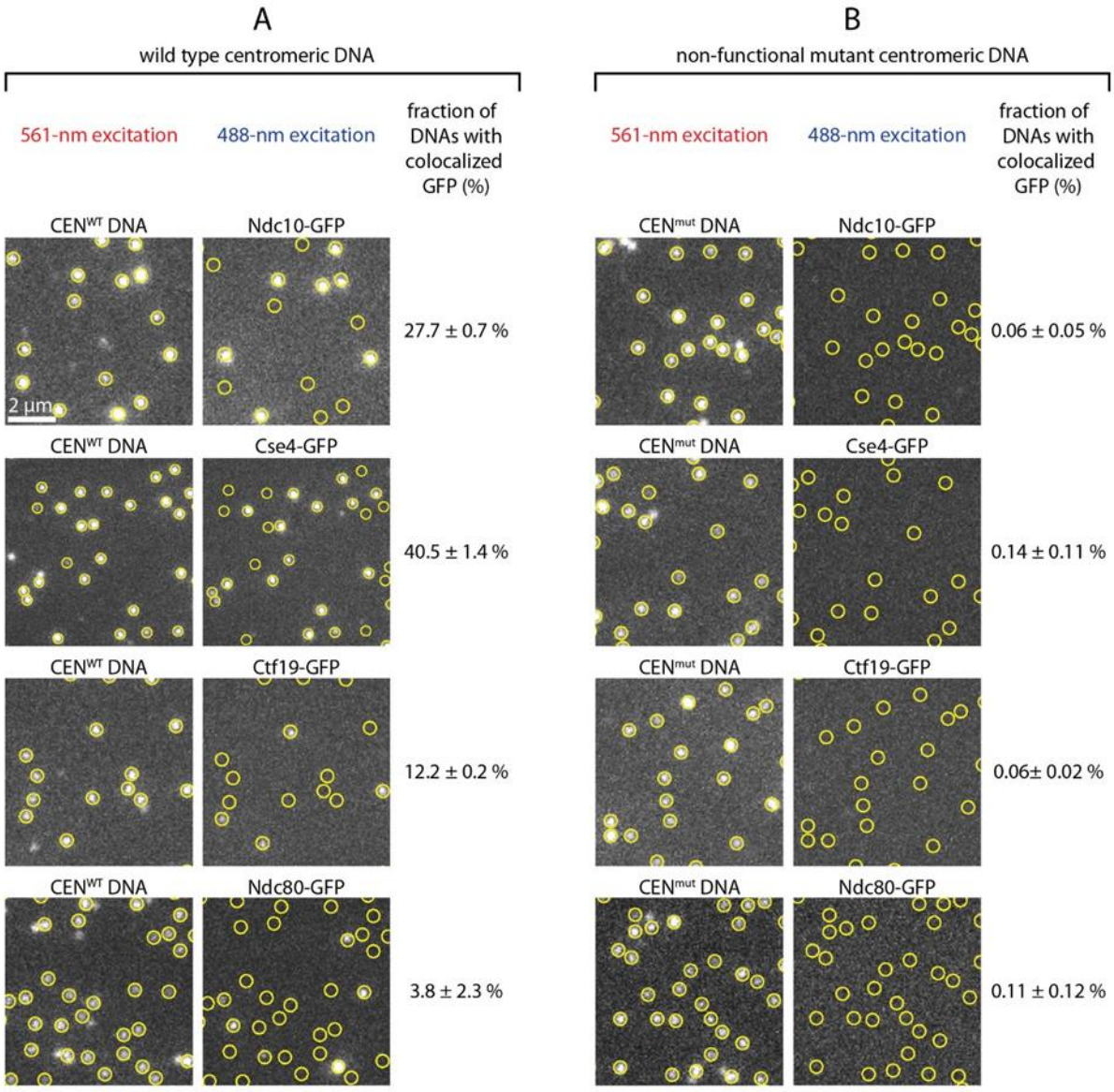

Supplementary Figure 1s1. ***De novo*** **assembly of individual kinetochores occurs specifically on centromeric DNAs. A)** Images of individual Atto565-labeled centromeric DNAs (left) and corresponding images of GFP-tagged kinetochore subcomplexes (right) from the same fields of view. Yellow circles mark locations of individual wild type centromeric DNAs (CEN^{WT}), which contain the complete 117-bp centromere sequence from *S. cerevisiae* chromosome III. **B)** Images from negative control experiments using mutant centromeric DNAs (CEN^{mut}) carrying a 3-bp substitution that prevents kinetochore assembly. The percentages in both A and B represent average fractions (± SEM) of centromeric DNAs that colocalized with a GFP signal from the indicated kinetochore protein, calculated from $N > 3{,}400$ DNAs for each kinetochore component from at least 9 fields of view across three independent experiments.

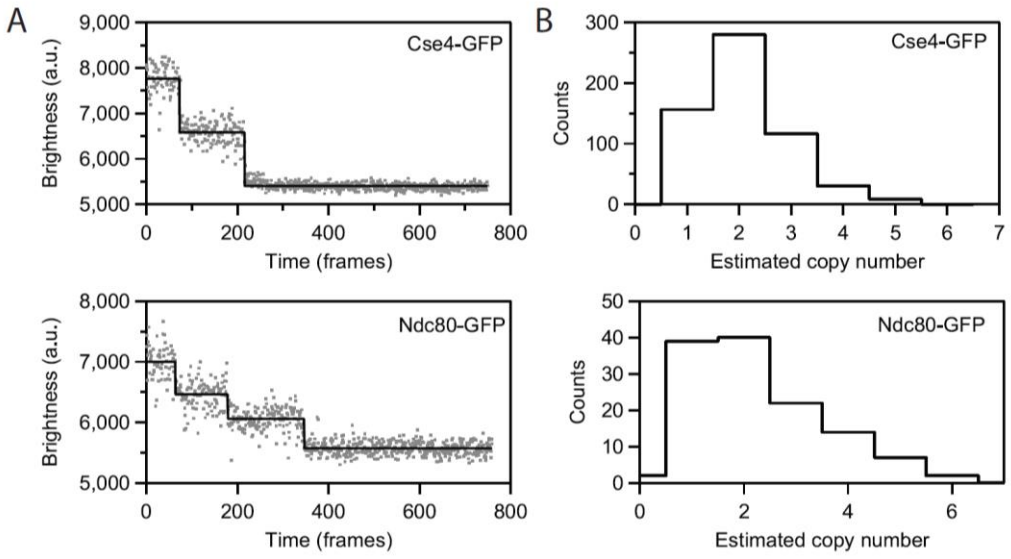

Supplementary Figure 1s2. Photobleach analysis of Cse4- or Ndc80-GFP assembled kinetochores. A) Representative records of fluorescence intensity versus time for individual Cse4-GFP (top) or Ndc80-GFP (bottom) assembled kinetochores. The raw intensity data is represented by gray spots and the estimated bleach steps are represented by the solid black line. Bleach steps were estimated using the Tdetector2 step detection algorithm.[80] **B)** Histograms showing the estimated copy number of Cse4-GFP (top) or Ndc80-GFP (bottom) present in individual assembled kinetochores. *N* = 591 individual Cse4-GFP kinetochores and *N* = 126 individual Ndc80-GFP kinetochores.

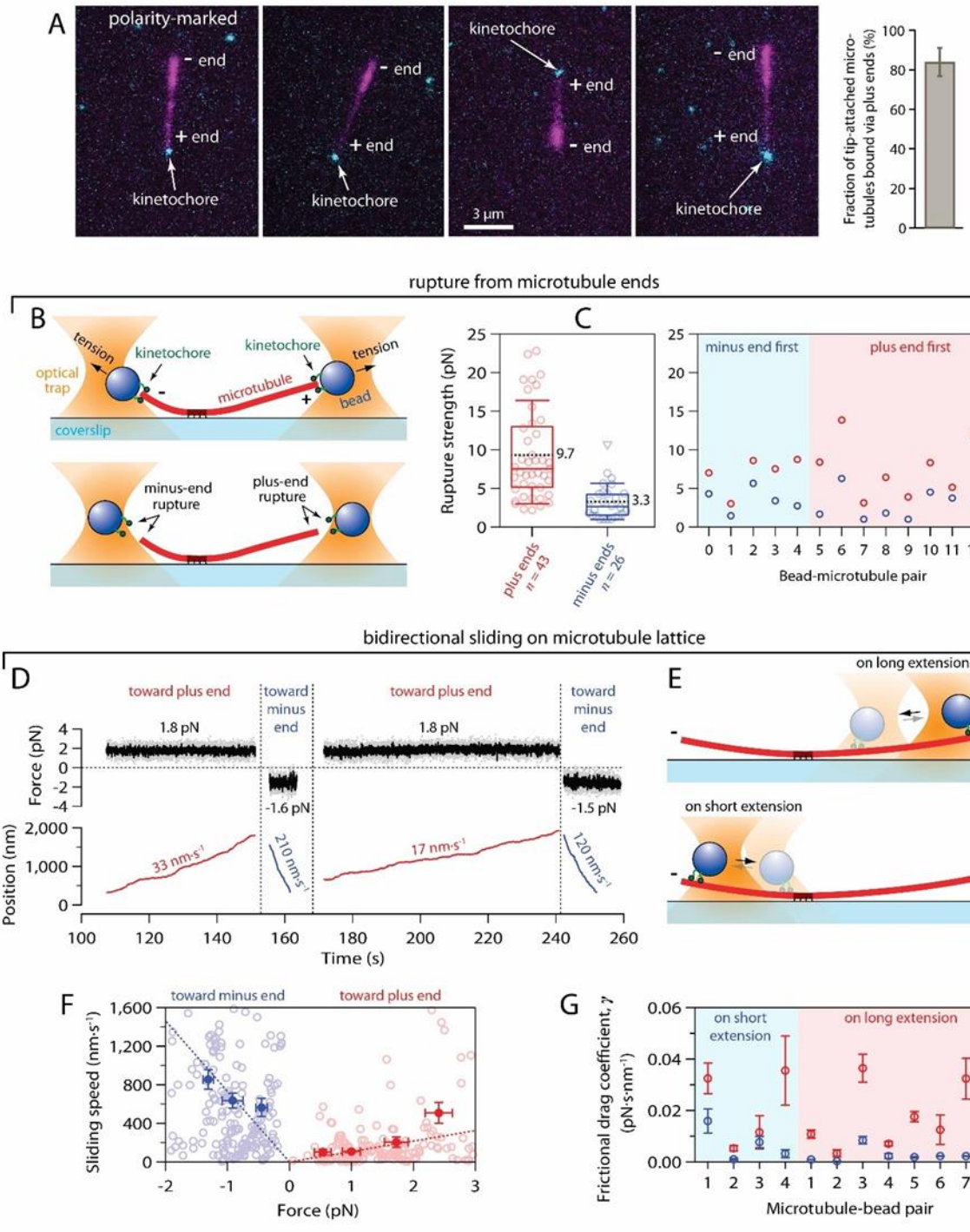
A
polarity-marked
- end
+ end
kinetochore
3 µm
Fraction of tip-attached microtubules bound via plus ends (%)
rupture from microtubule ends
B
tension
kinetochore
optical trap
microtubule
bead
coverslip
minus-end rupture
plus-end rupture
C
Rupture strength (pN)
9.7
3.3
plus ends n = 43
minus ends n = 26
minus end first
plus end first
Bead-microtubule pair
bidirectional sliding on microtubule lattice
D
toward plus end
toward minus end
1.8 pN
-1.6 pN
-1.5 pN
Force (pN)
Position (nm)
33 nm·s⁻¹
210 nm·s⁻¹
17 nm·s⁻¹
120 nm·s⁻¹
Time (s)
E
on long extension
on short extension
F
toward minus end
toward plus end
Sliding speed (nm·s⁻¹)
Force (pN)
G
on short extension
on long extension
Frictional drag coefficient, γ (pN·s·nm⁻¹)
Microtubule-bead pair

Figure 2. Kinetochores specifically capture plus ends and grip more strongly when pulled toward plus ends. A) Kinetochores assembled *de novo* have a strong intrinsic preference for plus ends. Tip-captured, polarity-marked microtubules (magenta), polymerized with dim plus ends and bright minus ends, nearly always bound assembled Ndc80-GFP kinetochores (cyan) by their plus ends. Bar graph shows percentage of tip-attached microtubules that were bound by their plus ends (mean ± SDEV from *N* = 8 experiments examining a total of 196 tip-captured microtubules). **B)** Schematic of the rupture force assay. Native kinetochore particles isolated from yeast were conjugated sparsely to polystyrene microbeads. A laser trap was used to attach a kinetochore-bead to either the plus or minus end of an individual dynamic microtubule and then to measure the rupture strength of the attachment. **C)** *Left:* Distribution of rupture strengths for attachments to plus and minus ends. Open circles represent individual rupture strength measurements. Triangles show censored data, when rupture strength exceeded the maximum force of the trap, or the microtubule broke away from the coverslip surface. Boxes extend from the first to the third quartiles with medians indicated by the central horizontal solid lines. Whiskers extend ± one SDEV from the means, which are indicated by dashed black lines. *Right:* Rupture strengths for individual kinetochore-beads measured sequentially at both ends of the same microtubule, either minus end first or plus end first as indicated. **D)** Measurement of bidirectional sliding friction. Record of force and position versus time for a kinetochore-bead attached to the side of a coverslip-anchored microtubule and pulled alternately toward the plus (red trace) and minus end (blue trace). Additional records are shown in Supplementary Figure 2s2. **E)** Schematic of the sliding assay. Kinetochore-beads were tested on both long and short extensions, to confirm that the speed differential arises from microtubule polarity rather than asymmetric anchorage of the microtubule to the coverslip. **F)** Bidirectional sliding speeds plotted against applied force. Open circles show speeds from individual events. Dotted lines represent fits to these individual speeds. Closed circles represent mean speeds ± SEM after binning by force (*N* = 23 – 81 events per bin). **G)** Frictional drag coefficients for individual kinetochore-beads sliding toward plus (red symbols) and minus ends (blue symbols) on short and long microtubule extensions, as indicated. Beads 1 through 4 were measured sequentially on both extensions of the same microtubule. Symbols represent mean frictional drag coefficient ± SEM (from *N* > 5 events per bead-microtubule pair).

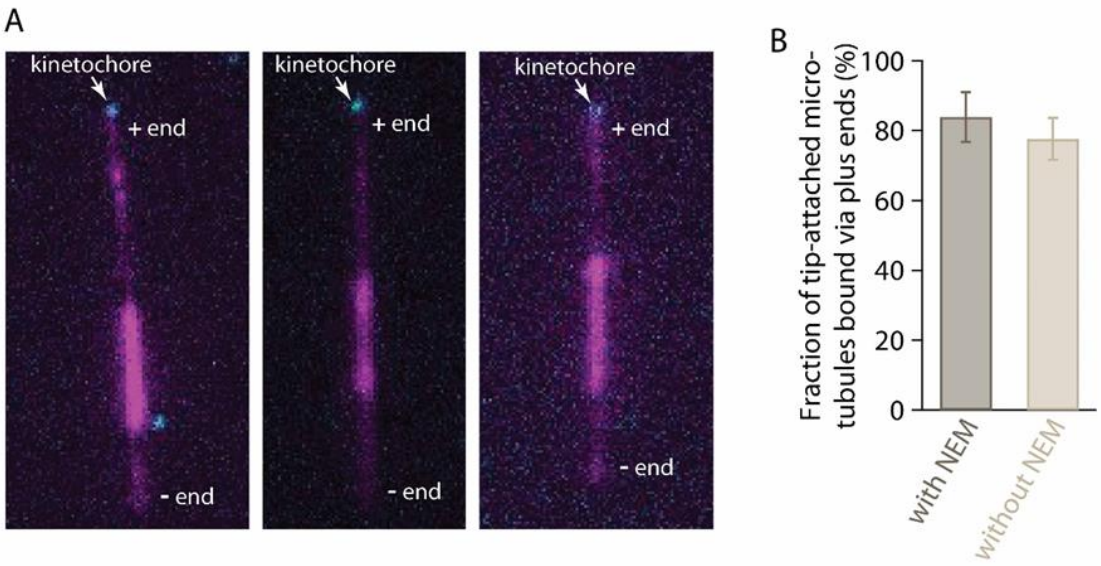

Supplementary Figure 2s1. Plus end preference is not an artifact of differential labeling. A) Polarity-marked microtubules (magenta), polymerized from bright seeds with dim extensions on both plus and minus ends, were nearly always captured via their plus ends by assembled Ndc80-GFP kinetochores (cyan). To polymerize dim extensions from both ends of bright seeds, NEM-treated tubulin was omitted from the polymerization mix (see Materials and Methods). Polymerization at plus ends is faster than at minus ends, so plus ends were distinguishable by their longer lengths relative to minus ends. **B)** Percentages of tip-captured, polarity marked microtubules that bound by their plus ends. A strong preference for plus ends occurred irrespective of whether the minus ends were more brightly labeled, via polymerization with a small amount of NEM-treated tubulin (with NEM, at left), or whether the minus and plus ends were both dimly labeled, via polymerization without NEM-treated tubulin (without NEM, at right). See Materials and Methods for details about how polarity-marked microtubules were generated. Bars represent percentages of polarity-marked microtubules that were bound by their plus ends (mean ± SDEV, from *N* = 4 experiments with NEM and *N* = 4 without NEM, examining a total of 86 and 110 tip-captured microtubules, respectively).

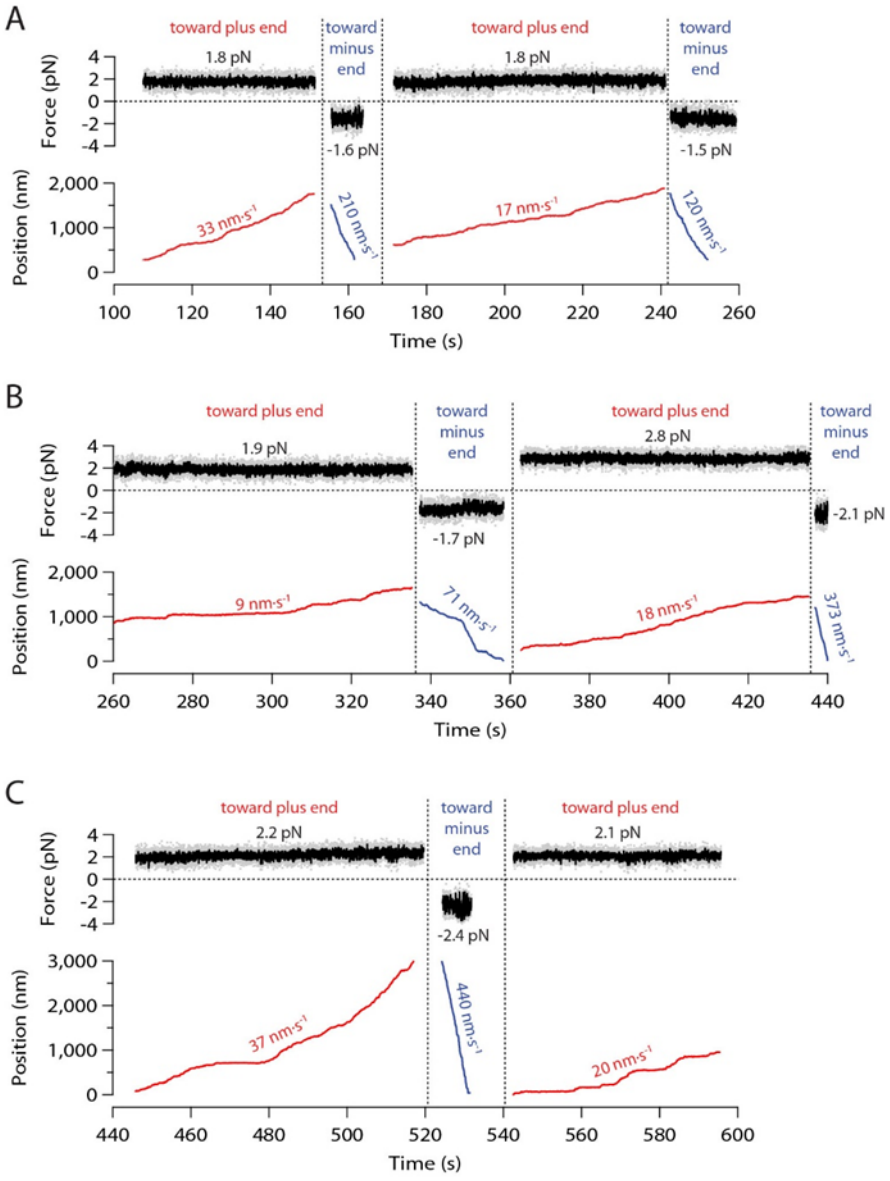

Supplementary Figure 2s2. Example records showing measurement of bidirectional sliding friction. Force and position are plotted against time for a kinetochore-decorated bead attached to the side of a coverslip-anchored microtubule and pulled alternately toward the plus (red traces) and minus end (blue traces). Mean forces and speeds for each sliding event are indicated.

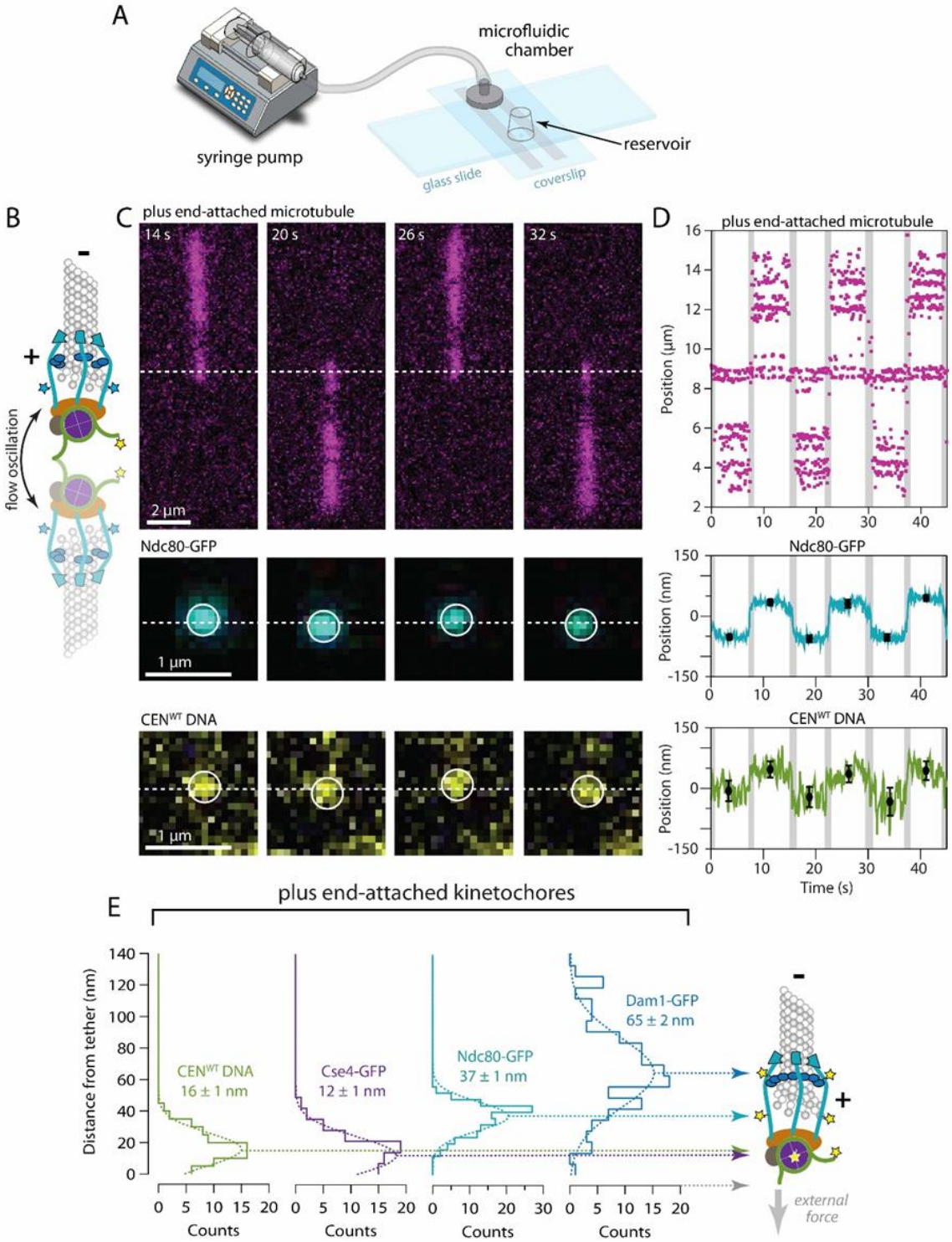
A
microfluidic chamber
syringe pump
reservoir
glass slide
coverslip
B
flow oscillation
C
plus end-attached microtubule
14 s
20 s
26 s
32 s
2 µm
Ndc80-GFP
1 µm
CEN^WT DNA
1 µm
D
plus end-attached microtubule
Position (µm)
Ndc80-GFP
Position (nm)
CEN^WT DNA
Position (nm)
Time (s)
E
plus end-attached kinetochores
Distance from tether (nm)
CEN^WT DNA
16 ± 1 nm
Cse4-GFP
12 ± 1 nm
Ndc80-GFP
37 ± 1 nm
Dam1-GFP
65 ± 2 nm
Counts
external force

Figure 3. Tip-attached kinetochores are well organized along the microtubule axis. A) Kinetochores were assembled in a microfluidic device and then allowed to capture microtubules. A syringe pump enabled imaging of the kinetochores and their captured microtubules while buffer was flowed gently through the assembly chamber. **B)** Schematic of a surface-assembled kinetochore attached to the tip of a microtubule. Oscillating the direction of flow caused the kinetochore and its captured microtubule to flip back and forth, reorienting by 180° with each reversal of the flow. **C)** Time-lapse image series showing flow-induced reorientation of a microtubule (magenta) attached by its end to a surface-assembled kinetochore. Both the Ndc80-GFP kinetochore marker (cyan) and the Atto565 label on the wild type centromeric DNA (yellow, CEN^{WT}) oscillated with the direction of buffer flow. **D)** Example records of position versus time for an Ndc80-GFP spot and the corresponding Atto565-labeled centromeric DNA obtained by tracking the individual spots with sub-pixel accuracy. Displacements of each spot from the tether point were estimated by averaging during the intervals when the microtubule orientation was steady. Black symbols represent mean ± SDEV from $N \approx 60$ tracked positions during each interval. Positions recorded during reorientation of the microtubule were omitted from the averaging and are indicated here by gray shading. Additional records are shown in Supplementary Figure 3s1. **E)** Distributions of displacement for the indicated fluorescent kinetochore components (from $N = 67$ to 128 intervals), fit with single Gaussian functions. The mean ± SEM for each Gaussian is indicated. Displacements for Cse4-GFP, a component of the centromeric nucleosome, are similar to the centromeric DNA (CEN^{WT}), as expected. The larger displacements for outer microtubule-binding components, Ndc80-GFP and Dam1-GFP, are consistent with the *in vivo* arrangement.[58,65]

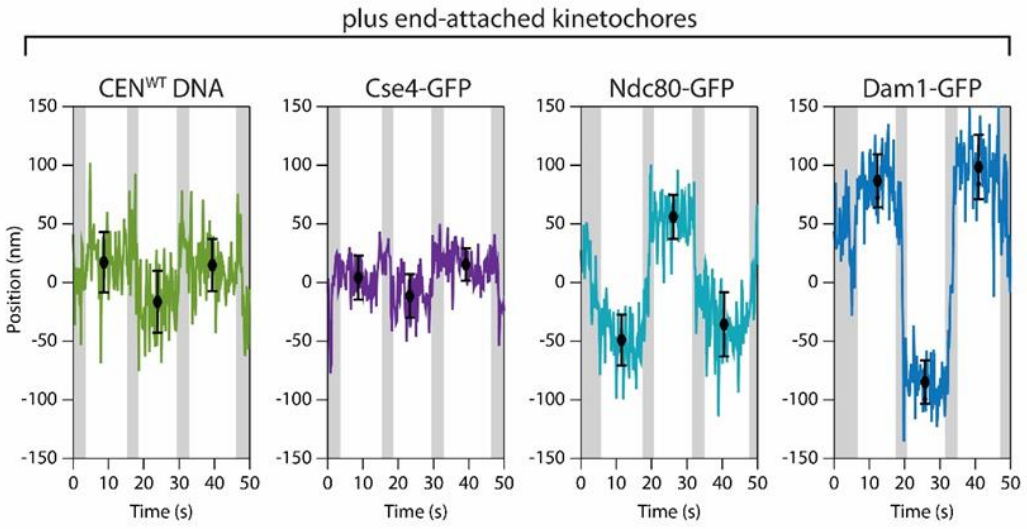

Supplementary Figure 3s1. Nanoscale displacement of fluorescent-tagged components within individual tip-attached kinetochores during periodic flow-induced reorientation. Positions for the indicated GFP-labeled components were tracked with sub-pixel accuracy while the direction of fluid flow was oscillated, causing the kinetochore and its captured microtubule to flip back and forth, reorienting by 180° with each reversal of the flow. Displacements from the tether point were estimated by averaging during the intervals when the microtubule orientation was steady. Black symbols represent mean ± SDEV from $N \approx 60$ tracked positions during each interval. Positions recorded during reorientation of the microtubule were omitted from the averaging and are indicated here by gray shading.

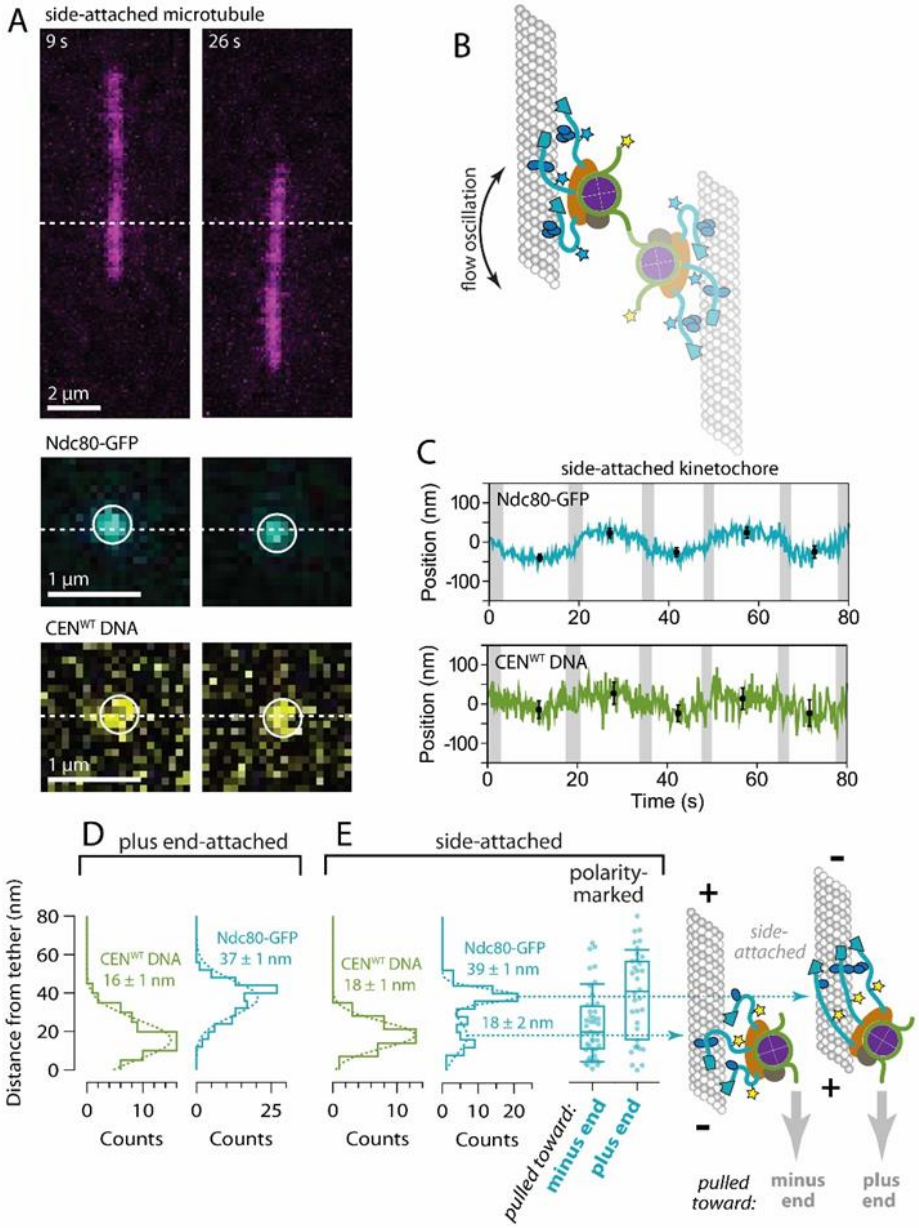
A
side-attached microtubule
9 s
26 s
2 µm
Ndc80-GFP
1 µm
CEN^WT DNA
1 µm
B
flow oscillation
C
side-attached kinetochore
Ndc80-GFP
Position (nm)
100
0
-100
0
20
40
60
80
CEN^WT DNA
Position (nm)
Time (s)
D
plus end-attached
E
side-attached
polarity-marked
Distance from tether (nm)
CEN^WT DNA
16 ± 1 nm
Ndc80-GFP
37 ± 1 nm
Counts
CEN^WT DNA
18 ± 1 nm
Ndc80-GFP
39 ± 1 nm
18 ± 2 nm
pulled toward:
minus end
plus end
side-attached
pulled toward:
minus end
plus end

Figure 4. Side-attached kinetochores are less organized than tip-attached kinetochores. A) Time-lapse images showing flow-induced reorientation of a microtubule (magenta) attached by its side to a surface-assembled kinetochore. Both the Ndc80-GFP kinetochore marker (cyan) and the Atto565 label on the centromeric DNA (yellow) oscillated with the direction of buffer flow. **B)** Schematic of a surface-assembled kinetochore attached to the side of a microtubule. Oscillating the direction of flow caused the kinetochore and its captured microtubule to flip back and forth, reorienting by 180° with each reversal of the flow. **C)** Example records of position versus time for an Ndc80-GFP kinetochore attached to the side of a microtubule. Displacements of both the Ndc80-GFP spot and the Atto565 label on the wild type centromeric DNA (CEN^{WT}) relative to the tether point were estimated by averaging during the intervals when the microtubule orientation was steady. Black symbols represent mean ± SDEV from $N \approx 60$ tracked positions during each interval. Positions recorded during reorientation of the microtubule were omitted from the averaging and are indicated here by gray shading. **D)** Distributions of displacement for the indicated fluorescent components within tip-attached kinetochores (from $N = 74$ to 116 intervals), fit with single Gaussian functions. The mean ± SEM for each Gaussian is indicated. These data and fits are replotted from Figure 4B with an expanded vertical scale. **E)** Distributions of displacement for the indicated fluorescent components within side-attached kinetochores (from $N = 32$ to 87 intervals), fit with either a single Gaussian (CEN^{WT} DNA) or a double Gaussian function (Ndc80-GFP). The mean ± SEM for each Gaussian is indicated. The distribution of Ndc80-GFP displacements for side-attached kinetochores is wider in comparison to the tip-attached kinetochores in panel D, and apparently bimodal, including a sub-population very close to the tether with a mean displacement of only 18 ± 2 nm.

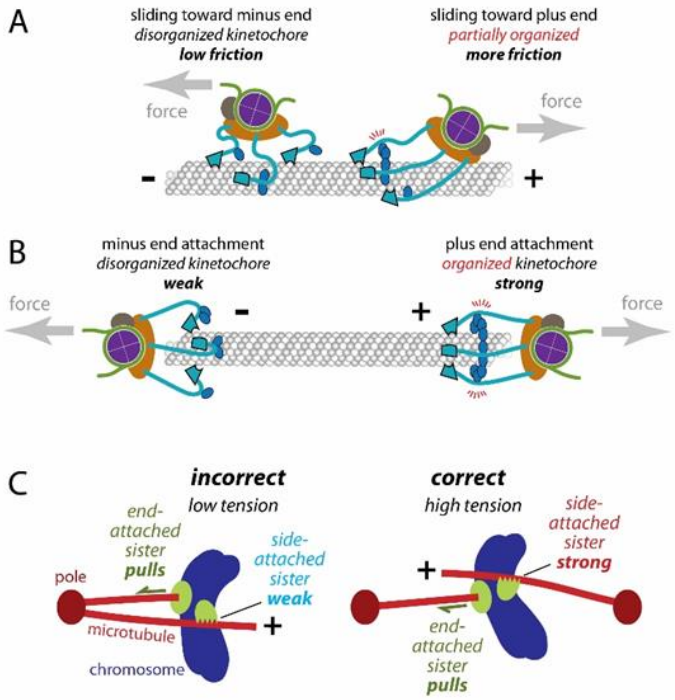

Figure 5. How the directionally asymmetric grip of the kinetochore might arise from microtubule polarity and promote accuracy during early mitosis. A) Each Ndc80c fibril (light blue) has a globular 'foot' (outlined in black), which binds with a stereospecific 'footprint' on the outside surface of the microtubule, and a coiled-coil stalk that emanates from this foot and projects toward the plus end. *Right:* Pulling a kinetochore toward the plus end aligns its multiple Ndc80c stalks into a parallel configuration, facilitating interactions with Dam1c oligomers and strengthening the overall grip on the microtubule. Because the direction of force is aligned with the stalks, torque on the Ndc80c-microtubule bonds is minimized. *Left:* Pulling a kinetochore toward the minus end disrupts this organization, weakening its grip. **B)** *Right:* At a plus end, the Ndc80c stalks can all project in parallel past the tip of the microtubule and converge onto the centromeric nucleosome,[34] potentially allowing Dam1c oligomers to organize a cage-like arrangement surrounding the tip,[31,34] with even higher grip strength. *Left:* At a minus end, parallel convergence of the stalks is impossible, increasing the torque on the Ndc80c-microtubule bonds and potentially reducing lateral interactions via Dam1c. **C)** After a pair of sister kinetochores initially makes side-attachments, one of them will (by chance) become tip-attached before the other, tracking with tip shortening and exerting elastic pulling forces on its side-attached sister. *Left:* If the pair is attached incorrectly to microtubules from the same pole, then the side-attached sister will be pulled toward the minus end. Its grip will therefore be weak, and it will likely detach. *Right:* If the pair is attached correctly to microtubules from opposite poles, then the side-attached sister will be pulled toward the plus end. It will therefore have a stronger grip that should allow it to remain attached and achieve proper bi-orientation at the plus end.

References

1. Hayden, J.H., Bowser, S.S., and Rieder, C.L. (1990). Kinetochores capture astral microtubules during chromosome attachment to the mitotic spindle: direct visualization in live newt lung cells. J Cell Biol *111*, 1039-1045. 10.1083/jcb.111.3.1039.
2. Rieder, C.L., and Alexander, S.P. (1990). Kinetochores are transported poleward along a single astral microtubule during chromosome attachment to the spindle in newt lung cells. J Cell Biol *110*, 81-95. 10.1083/jcb.110.1.81.
3. Tanaka, K., Mukae, N., Dewar, H., van Breugel, M., James, E.K., Prescott, A.R., Antony, C., and Tanaka, T.U. (2005). Molecular mechanisms of kinetochore capture by spindle microtubules. Nature *434*, 987-994. 10.1038/nature03483.
4. Itoh, G., Ikeda, M., Iemura, K., Amin, M.A., Kuriyama, S., Tanaka, M., Mizuno, N., Osakada, H., Haraguchi, T., and Tanaka, K. (2018). Lateral attachment of kinetochores to microtubules is enriched in prometaphase rosette and facilitates chromosome alignment and bi-orientation establishment. Sci Rep *8*, 3888. 10.1038/s41598-018-22164-5.
5. Kapoor, T.M., Lampson, M.A., Hergert, P., Cameron, L., Cimini, D., Salmon, E.D., McEwen, B.F., and Khodjakov, A. (2006). Chromosomes can congress to the metaphase plate before biorientation. Science *311*, 388-391. 10.1126/science.1122142.
6. Torvi, J.R., Wong, J., Serwas, D., Moayed, A., Drubin, D.G., and Barnes, G. (2022). Reconstitution of kinetochore motility and microtubule dynamics reveals a role for a kinesin-8 in establishing end-on attachments. Elife *11*. 10.7554/eLife.78450.
7. Inoue, S., and Salmon, E.D. (1995). Force generation by microtubule assembly/disassembly in mitosis and related movements. Mol Biol Cell *6*, 1619-1640.
8. Nicklas, R.B. (1997). How cells get the right chromosomes. Science *275*, 632-637.
9. Sarangapani, K.K., and Asbury, C.L. (2014). Catch and release: how do kinetochores hook the right microtubules during mitosis? Trends in genetics : TIG *30*, 150-159. 10.1016/j.tig.2014.02.004.
10. Lampson, M.A., and Grishchuk, E.L. (2017). Mechanisms to Avoid and Correct Erroneous Kinetochore-Microtubule Attachments. Biology (Basel) *6*. 10.3390/biology6010001.
11. Funabiki, H. (2019). Correcting aberrant kinetochore microtubule attachments: a hidden regulation of Aurora B on microtubules. Curr Opin Cell Biol *58*, 34-41. 10.1016/j.ceb.2018.12.007.
12. Liu, D., Vader, G., Vromans, M.J., Lampson, M.A., and Lens, S.M. (2009). Sensing chromosome bi-orientation by spatial separation of aurora B kinase from kinetochore substrates. Science *323*, 1350-1353. 10.1126/science.1167000.
13. de Regt, A.K., Clark, C.J., Asbury, C.L., and Biggins, S. (2022). Tension can directly suppress Aurora B kinase-triggered release of kinetochore-microtubule attachments. Nature communications *13*, 2152. 10.1038/s41467-022-29542-8.
14. Akiyoshi, B., Sarangapani, K.K., Powers, A.F., Nelson, C.R., Reichow, S.L., Arellano-Santoyo, H., Gonen, T., Ranish, J.A., Asbury, C.L., and Biggins, S. (2010). Tension directly stabilizes reconstituted kinetochore-microtubule attachments. Nature *468*, 576-579. 10.1038/nature09594.
15. Brouhard, G.J., and Rice, L.M. (2018). Microtubule dynamics: an interplay of biochemistry and mechanics. Nat Rev Mol Cell Biol *19*, 451-463. 10.1038/s41580-018-0009-y.
16. Walker, R.A., O'Brien, E.T., Pryer, N.K., Soboeiro, M.F., Voter, W.A., Erickson, H.P., and Salmon, E.D. (1988). Dynamic instability of individual microtubules analyzed by video light microscopy: rate constants and transition frequencies. J Cell Biol *107*, 1437-1448.

17. Alushin, G.M., Lander, G.C., Kellogg, E.H., Zhang, R., Baker, D., and Nogales, E. (2014). High-resolution microtubule structures reveal the structural transitions in alphabeta-tubulin upon GTP hydrolysis. Cell *157*, 1117-1129. 10.1016/j.cell.2014.03.053.
18. Mandelkow, E.M., Mandelkow, E., and Milligan, R.A. (1991). Microtubule dynamics and microtubule caps: a time-resolved cryo-electron microscopy study. J Cell Biol *114*, 977-991.
19. McIntosh, J.R., O'Toole, E., Morgan, G., Austin, J., Ulyanov, E., Ataullakhanov, F., and Gudimchuk, N. (2018). Microtubules grow by the addition of bent guanosine triphosphate tubulin to the tips of curved protofilaments. J. Cell Biol. *217*, 2691-2708. 10.1083/jcb.201802138.
20. Bloom, K.S., and Carbon, J. (1982). Yeast centromere DNA is in a unique and highly ordered structure in chromosomes and small circular minichromosomes. Cell *29*, 305-317. 10.1016/0092-8674(82)90147-7.
21. Furuyama, S., and Biggins, S. (2007). Centromere identity is specified by a single centromeric nucleosome in budding yeast. Proc Natl Acad Sci U S A *104*, 14706-14711. 10.1073/pnas.0706985104.
22. Winey, M., Mamay, C.L., O'Toole, E.T., Mastronarde, D.N., Giddings, T.H., Jr., McDonald, K.L., and McIntosh, J.R. (1995). Three-dimensional ultrastructural analysis of the Saccharomyces cerevisiae mitotic spindle. J Cell Biol *129*, 1601-1615.
23. Monda, J.K., and Cheeseman, I.M. (2018). The kinetochore-microtubule interface at a glance. J Cell Sci *131*. 10.1242/jcs.214577.
24. Ciferri, C., De Luca, J., Monzani, S., Ferrari, K.J., Ristic, D., Wyman, C., Stark, H., Kilmartin, J., Salmon, E.D., and Musacchio, A. (2005). Architecture of the human ndc80-hec1 complex, a critical constituent of the outer kinetochore. J Biol Chem *280*, 29088-29095. 10.1074/jbc.M504070200.
25. Wei, R.R., Al-Bassam, J., and Harrison, S.C. (2007). The Ndc80/HEC1 complex is a contact point for kinetochore-microtubule attachment. Nat Struct Mol Biol *14*, 54-59. 10.1038/nsmb1186.
26. Wilson-Kubalek, E.M., Cheeseman, I.M., Yoshioka, C., Desai, A., and Milligan, R.A. (2008). Orientation and structure of the Ndc80 complex on the microtubule lattice. J Cell Biol *182*, 1055-1061. 10.1083/jcb.200804170.
27. Alushin, G.M., Ramey, V.H., Pasqualato, S., Ball, D.A., Grigorieff, N., Musacchio, A., and Nogales, E. (2010). The Ndc80 kinetochore complex forms oligomeric arrays along microtubules. Nature *467*, 805-810. 10.1038/nature09423.
28. Wilson-Kubalek, E.M., Cheeseman, I.M., and Milligan, R.A. (2016). Structural comparison of the Caenorhabditis elegans and human Ndc80 complexes bound to microtubules reveals distinct binding behavior. Mol Biol Cell *27*, 1197-1203. 10.1091/mbc.E15-12-0858.
29. van Hooff, J.J.E., Snel, B., and Kops, G. (2017). Unique Phylogenetic Distributions of the Ska and Dam1 Complexes Support Functional Analogy and Suggest Multiple Parallel Displacements of Ska by Dam1. Genome Biol Evol *9*, 1295-1303. 10.1093/gbe/evx088.
30. Westermann, S., Avila-Sakar, A., Wang, H.W., Niederstrasser, H., Wong, J., Drubin, D.G., Nogales, E., and Barnes, G. (2005). Formation of a dynamic kinetochore- microtubule interface through assembly of the Dam1 ring complex. Mol Cell *17*, 277-290. 10.1016/j.molcel.2004.12.019.
31. Miranda, J.J., De Wulf, P., Sorger, P.K., and Harrison, S.C. (2005). The yeast DASH complex forms closed rings on microtubules. Nat Struct Mol Biol *12*, 138-143. 10.1038/nsmb896.
32. Kim, J.O., Zelter, A., Umbreit, N.T., Bollozos, A., Riffle, M., Johnson, R., MacCoss, M.J., Asbury, C.L., and Davis, T.N. (2017). The Ndc80 complex bridges two Dam1 complex rings. Elife *6*. 10.7554/eLife.21069.
33. Jenni, S., and Harrison, S.C. (2018). Structure of the DASH/Dam1 complex shows its role at the yeast kinetochore-microtubule interface. Science *360*, 552-558. 10.1126/science.aar6436.

34. Muir, K.W., Batters, C., Dendooven, T., Yang, J., Zhang, Z., Burt, A., and Barford, D. (2023). Structural mechanism of outer kinetochore Dam1-Ndc80 complex assembly on microtubules. Science *382*, 1184-1190. 10.1126/science.adj8736.
35. Miller, M.P., Asbury, C.L., and Biggins, S. (2016). A TOG Protein Confers Tension Sensitivity to Kinetochore-Microtubule Attachments. Cell *165*, 1428-1439. 10.1016/j.cell.2016.04.030.
36. Zahm, J.A., Stewart, M.G., Carrier, J.S., Harrison, S.C., and Miller, M.P. (2021). Structural basis of Stu2 recruitment to yeast kinetochores. Elife *10*. 10.7554/eLife.65389.
37. Herman, J.A., Miller, M.P., and Biggins, S. (2020). chTOG is a conserved mitotic error correction factor. Elife *9*. 10.7554/eLife.61773.
38. Powers, A.F., Franck, A.D., Gestaut, D.R., Cooper, J., Gracyzk, B., Wei, R.R., Wordeman, L., Davis, T.N., and Asbury, C.L. (2009). The Ndc80 kinetochore complex forms load-bearing attachments to dynamic microtubule tips via biased diffusion. Cell *136*, 865-875. 10.1016/j.cell.2008.12.045.
39. Asbury, C.L., Gestaut, D.R., Powers, A.F., Franck, A.D., and Davis, T.N. (2006). The Dam1 kinetochore complex harnesses microtubule dynamics to produce force and movement. Proc Natl Acad Sci U S A *103*, 9873-9878. 10.1073/pnas.0602249103.
40. Ayaz, P., Ye, X., Huddleston, P., Brautigam, C.A., and Rice, L.M. (2012). A TOG:alphabeta-tubulin complex structure reveals conformation-based mechanisms for a microtubule polymerase. Science *337*, 857-860. 10.1126/science.1221698.
41. Huang, D.L., Bax, N.A., Buckley, C.D., Weis, W.I., and Dunn, A.R. (2017). Vinculin forms a directionally asymmetric catch bond with F-actin. Science *357*, 703-706. 10.1126/science.aan2556.
42. Owen, L.M., Bax, N.A., Weis, W.I., and Dunn, A.R. (2022). The C-terminal actin-binding domain of talin forms an asymmetric catch bond with F-actin. Proc Natl Acad Sci U S A *119*, e2109329119. 10.1073/pnas.2109329119.
43. Arbore, C., Sergides, M., Gardini, L., Bianchi, G., Kashchuk, A.V., Pertici, I., Bianco, P., Pavone, F.S., and Capitanio, M. (2022). alpha-catenin switches between a slip and an asymmetric catch bond with F-actin to cooperatively regulate cell junction fluidity. Nature communications *13*, 1146. 10.1038/s41467-022-28779-7.
44. Swaminathan, V., Alushin, G.M., and Waterman, C.M. (2017). Mechanosensation: A Catch Bond That Only Hooks One Way. Curr Biol *27*, R1158-R1160. 10.1016/j.cub.2017.09.023.
45. Sun, X., and Alushin, G.M. (2023). Cellular force-sensing through actin filaments. The FEBS journal *290*, 2576-2589. 10.1111/febs.16568.
46. Popchock, A.R., Larson, J.D., Dubrulle, J., Asbury, C.L., and Biggins, S. (2023). Direct observation of coordinated assembly of individual native centromeric nucleosomes. EMBO J *42*, e114534. 10.15252/embj.2023114534.
47. Friedman, L.J., and Gelles, J. (2012). Mechanism of transcription initiation at an activator-dependent promoter defined by single-molecule observation. Cell *148*, 679-689. 10.1016/j.cell.2012.01.018.
48. Hoskins, A.A., Friedman, L.J., Gallagher, S.S., Crawford, D.J., Anderson, E.G., Wombacher, R., Ramirez, N., Cornish, V.W., Gelles, J., and Moore, M.J. (2011). Ordered and dynamic assembly of single spliceosomes. Science *331*, 1289-1295. 10.1126/science.1198830.
49. Larson, J.D., and Hoskins, A.A. (2017). Dynamics and consequences of spliceosome E complex formation. Elife *6*. 10.7554/eLife.27592.
50. Lechner, J., and Carbon, J. (1991). A 240 kd multisubunit protein complex, CBF3, is a major component of the budding yeast centromere. Cell *64*, 717-725. 10.1016/0092-8674(91)90501-o.
51. Sorger, P.K., Doheny, K.F., Hieter, P., Kopski, K.M., Huffaker, T.C., and Hyman, A.A. (1995). Two genes required for the binding of an essential Saccharomyces cerevisiae kinetochore complex to DNA. Proc Natl Acad Sci U S A *92*, 12026-12030. 10.1073/pnas.92.26.12026.

52. Sorger, P.K., Severin, F.F., and Hyman, A.A. (1994). Factors required for the binding of reassembled yeast kinetochores to microtubules in vitro. J Cell Biol *127*, 995-1008.
53. Lang, J., Barber, A., and Biggins, S. (2018). An assay for de novo kinetochore assembly reveals a key role for the CENP-T pathway in budding yeast. Elife *7*. 10.7554/eLife.37819.
54. Howard, J., and Hyman, A.A. (1993). Preparation of marked microtubules for the assay of the polarity of microtubule-based motors by fluorescence microscopy. Methods Cell Biol *39*, 105-113. 10.1016/s0091-679x(08)60164-8.
55. Roostalu, J., Hentrich, C., Bieling, P., Telley, I.A., Schiebel, E., and Surrey, T. (2011). Directional switching of the kinesin Cin8 through motor coupling. Science *332*, 94-99. 10.1126/science.1199945.
56. Waters, J.C., Skibbens, R.V., and Salmon, E.D. (1996). Oscillating mitotic newt lung cell kinetochores are, on average, under tension and rarely push. J Cell Sci *109 (Pt 12)*, 2823-2831.
57. Bormuth, V., Varga, V., Howard, J., and Schaffer, E. (2009). Protein friction limits diffusive and directed movements of kinesin motors on microtubules. Science *325*, 870-873. 10.1126/science.1174923.
58. Joglekar, A.P., Bloom, K., and Salmon, E.D. (2009). In vivo protein architecture of the eukaryotic kinetochore with nanometer scale accuracy. Curr Biol *19*, 694-699. 10.1016/j.cub.2009.02.056.
59. Wan, X., O'Quinn, R.P., Pierce, H.L., Joglekar, A.P., Gall, W.E., DeLuca, J.G., Carroll, C.W., Liu, S.T., Yen, T.J., McEwen, B.F., et al. (2009). Protein architecture of the human kinetochore microtubule attachment site. Cell *137*, 672-684. 10.1016/j.cell.2009.03.035.
60. Dumont, S., Salmon, E.D., and Mitchison, T.J. (2012). Deformations within moving kinetochores reveal different sites of active and passive force generation. Science *337*, 355-358. 10.1126/science.1221886.
61. Ciferri, C., Pasqualato, S., Screpanti, E., Varetti, G., Santaguida, S., Dos Reis, G., Maiolica, A., Polka, J., De Luca, J.G., De Wulf, P., et al. (2008). Implications for kinetochore-microtubule attachment from the structure of an engineered Ndc80 complex. Cell *133*, 427-439. 10.1016/j.cell.2008.03.020.
62. Wei, R.R., Sorger, P.K., and Harrison, S.C. (2005). Molecular organization of the Ndc80 complex, an essential kinetochore component. Proc Natl Acad Sci U S A *102*, 5363-5367. 10.1073/pnas.0501168102.
63. Zahm, J.A., Jenni, S., and Harrison, S.C. (2023). Structure of the Ndc80 complex and its interactions at the yeast kinetochore-microtubule interface. Open biology *13*, 220378. 10.1098/rsob.220378.
64. Flores, R.L., Peterson, Z.E., Zelter, A., Riffle, M., Asbury, C.L., and Davis, T.N. (2022). Three interacting regions of the Ndc80 and Dam1 complexes support microtubule tip-coupling under load. J Cell Biol *221*. 10.1083/jcb.202107016.
65. Cieslinski, K., Wu, Y.L., Nechyporenko, L., Horner, S.J., Conti, D., Skruzny, M., and Ries, J. (2023). Nanoscale structural organization and stoichiometry of the budding yeast kinetochore. J Cell Biol *222*. 10.1083/jcb.202209094.
66. Virant, D., Vojnovic, I., Winkelmeier, J., Endesfelder, M., Turkowyd, B., Lando, D., and Endesfelder, U. (2023). Unraveling the kinetochore nanostructure in Schizosaccharomyces pombe using multi-color SMLM imaging. J Cell Biol *222*. 10.1083/jcb.202209096.
67. Schmidt, J.C., Arthanari, H., Boeszoermenyi, A., Dashkevich, N.M., Wilson-Kubalek, E.M., Monnier, N., Markus, M., Oberer, M., Milligan, R.A., Bathe, M., et al. (2012). The kinetochore-bound Ska1 complex tracks depolymerizing microtubules and binds to curved protofilaments. Dev Cell *23*, 968-980. 10.1016/j.devcel.2012.09.012.
68. Volkov, V.A., Grissom, P.M., Arzhanik, V.K., Zaytsev, A.V., Renganathan, K., McClure-Begley, T., Old, W.M., Ahn, N., and McIntosh, J.R. (2015). Centromere protein F includes two sites that

couple efficiently to depolymerizing microtubules. J Cell Biol *209*, 813-828. 10.1083/jcb.201408083.
69. Wieczorek, M., Bechstedt, S., Chaaban, S., and Brouhard, G.J. (2015). Microtubule-associated proteins control the kinetics of microtubule nucleation. Nat Cell Biol *17*, 907-916. 10.1038/ncb3188.
70. Cheeseman, I.M., Chappie, J.S., Wilson-Kubalek, E.M., and Desai, A. (2006). The conserved KMN network constitutes the core microtubule-binding site of the kinetochore. Cell *127*, 983-997. 10.1016/j.cell.2006.09.039.
71. Wang, H.W., Long, S., Ciferri, C., Westermann, S., Drubin, D., Barnes, G., and Nogales, E. (2008). Architecture and flexibility of the yeast Ndc80 kinetochore complex. J Mol Biol *383*, 894-903. 10.1016/j.jmb.2008.08.077.
72. Polley, S., Muschenborn, H., Terbeck, M., De Antoni, A., Vetter, I.R., Dogterom, M., Musacchio, A., Volkov, V.A., and Huis In 't Veld, P.J. (2023). Stable kinetochore-microtubule attachment requires loop-dependent Ndc80-Ndc80 binding. EMBO J *42*, e112504. 10.15252/embj.2022112504.
73. Akiyoshi, B., Nelson, C.R., and Biggins, S. (2013). The aurora B kinase promotes inner and outer kinetochore interactions in budding yeast. Genetics *194*, 785-789. 10.1534/genetics.113.150839.
74. Amberg, D.C., Burke, D., Strathern, J.N., Burke, D., and Cold Spring Harbor Laboratory. (2005). Methods in yeast genetics : a Cold Spring Harbor Laboratory course manual, 2005 Edition (Cold Spring Harbor Laboratory Press).
75. Longtine, M.S., McKenzie, A., 3rd, Demarini, D.J., Shah, N.G., Wach, A., Brachat, A., Philippsen, P., and Pringle, J.R. (1998). Additional modules for versatile and economical PCR-based gene deletion and modification in Saccharomyces cerevisiae. Yeast *14*, 953-961. 10.1002/(SICI)1097-0061(199807)14:10<953::AID-YEA293>3.0.CO;2-U.
76. Deng, Y., and Asbury, C.L. (2017). Simultaneous Manipulation and Super-Resolution Fluorescence Imaging of Individual Kinetochores Coupled to Microtubule Tips. Methods Mol Biol *1486*, 437-467. 10.1007/978-1-4939-6421-5_17.
77. Crocker, J.C., and Grier, D.G. (1996). Methods of digital video microscopy for colloidal studies. J Colloid Interf Sci *179*, 298-310. DOI 10.1006/jcis.1996.0217.
78. Friedman, L.J., and Gelles, J. (2015). Multi-wavelength single-molecule fluorescence analysis of transcription mechanisms. Methods *86*, 27-36. 10.1016/j.ymeth.2015.05.026.
79. Sbalzarini, I.F., and Koumoutsakos, P. (2005). Feature point tracking and trajectory analysis for video imaging in cell biology. J Struct Biol *151*, 182-195. 10.1016/j.jsb.2005.06.002.
80. Chen, Y., Deffenbaugh, N.C., Anderson, C.T., and Hancock, W.O. (2014). Molecular counting by photobleaching in protein complexes with many subunits: best practices and application to the cellulose synthesis complex. Mol Biol Cell *25*, 3630-3642. 10.1091/mbc.E14-06-1146.

Chapter 5

Biased diffusion can explain kinetochore attachment to both assembling and disassembling microtubule tips

Introduction

Robust, long-lived microtubule-kinetochore attachments are required for proper segregation of chromosomes during mitosis. These connections must reasonably persist during both microtubule assembly and disassembly. Kinetochores purified from yeast attached to tips of dynamic microtubules in-vitro form dynamic bonds that detach with rates that vary from 10^{-4} s^{-1} to 10^{2} s^{-1} across a range of 1 to 15 pN [1, 2]. Though much progress has been made in our understanding of how individual proteins in the kinetochore interact with dynamic microtubules, it remains unclear how these proteins work together to maintain attachments to microtubule substrates that are growing and crumbling underneath their grip.

One model that has been proposed to account for kinetochore-microtubule attachment is the biased diffusion model. This model posits that a kinetochore is composed of many low-affinity microtubule binders that diffuse along the lattice in a thermally driven random walk. It is more energetically favorable to have a larger number of diffusors bound to the lattice, and so even under external load, a biased diffusion coupler can sustain attachment to an assembling or disassembling microtubule tip. Many of the proteins that are known to directly mediate the microtubule-kinetochore attachment such as Ndc80c, Stu2, Dam1c, and Ska, have been shown to associate with the microtubule lattice and diffuse along its length, a hallmark of the biased diffusion mechanism [3-6]. Furthermore, kinetochores are known to be composed of many copies of such proteins [7, 8].

However, models of biased diffusion have yet to recapitulate the load-bearing behavior of intact immunoprecipitated kinetochores from the experimentally measured biophysical properties of the individual proteins in the complex [9, 10]. In particular, biased diffusion models tend to perform poorly when forces are raised to physiological ranges [9], and they also tend to produce detachment rates that are far more force-sensitive than those measured for in-vitro kinetochore-microtubule attachments [11]. If biased diffusion models are an accurate representation of how kinetochore-microtubule attachments are sustained, these deficiencies suggest there are some features of the bond that are not represented in current models. This “missing link” could come in the form of an assisting force by a conformational wave—like coupler (hybrid model), or in the form of a biophysical property of kinetochore components that has not been incorporated into models before.

The first model of biased diffusion was posed by Terell Hill in 1985, and demonstrated that a simulated kinetochore composed of many low-affinity binders could maintain a persistent attachment to both assembling and disassembling microtubules [12]. Early biased diffusion models such as Hill’s assumed microtubule binding elements were rigidly linked together, reflecting low-resolution electron microscopy images of kinetochore plates in mammalian cells available at the time [12, 13]. The parameters in these models that describe single-molecule dynamics were deduced from the movements of chromosomes in living cells, not measured from single-molecule studies of individual kinetochore proteins. Models that explain chromosome oscillation and biorientation have been built from Hill’s original biased diffusion model [10, 13]. However, these models are characterized by several fundamental deficiencies. The models predict reasonable detachment rates for either microtubule assembly or disassembly, but not both. i.e., the differences in lifetimes for a Hill-like biased diffusion

model are many orders of magnitude different for an assembling vs. disassembling microtubule, a phenomenon not observed for MT-KT attachments in vivo or in vitro [1]. Furthermore, these models are largely insensitive to the underlying affinities of the biomolecules for the microtubule lattice, precluding phosphorylation-mediated weakening of the MT-KT attachment from playing a role in destabilizing KT-MT attachments, a phenomenon we know is fundamental to regulation of such attachments during mitosis [9]. Lastly, canonical hill-like biased diffusion models are extremely force-sensitive and persistently fail to sustain attachments at higher loads. Newer biased diffusion models have changed assumptions regarding flexibility of the kinetochore and incorporated other biophysical features in an attempt to remedy these known model defects [9, 14, 15].

A more modern view of kinetochores has emerged with the availability of higher-resolution structural information: kinetochores are composed of many non-rigid, flexible components [16]. Therefore, a fundamental assumption of the Hill model, that the microtubule binding elements are rigidly linked together, does not represent firm grounds for simulating kinetochore-microtubule interactions. Indeed, more recent models of microtubule-kinetochore attachment assume flexibility as a key feature of the underlying properties required for coupling [9, 15, 17]. Zaytsev et al. assumed the kinetochore could be modeled as independently diffusing microtubule binders, linked together by flexible elements. These microtubule binding elements were assigned a tunable cooperativity-mediated inhibition of unbinding from the lattice [9]. With these changes, the detachment rate of the complex was shown to exhibit sensitivity to both the affinity of the microtubule binders as well as the cooperativity factor, providing a mechanism for phosphorylation-mediated weakening of KT-MT attachments, an improvement over the original Hill model. Other similar models suggest an ideal coupler stiffness to maximize the load-bearing ability of the kinetochore [15]. Unfortunately, neither of these studies examined the relationship between detachment rate and applied load, precluding any assessment of the sensitivity of the predicted detachment rates to force, and the ability of the simulated couplers to sustain attachment at high loads. Such an investigation is needed to determine if accounting for flexibility produces more realistic models of microtubule-kinetochore attachment.

The assembly and disassembly speeds of microtubules are dramatically affected by the presence of a tip-attached kinetochore. Though the mean disassembly and assembly speeds of kinetochore-attached microtubules known from in-vivo data were incorporated into early models [10, 12, 13], it was not known at the time that tension exerted through a tip-attached kinetochore can accelerate growth up to 5-fold and decelerate disassembly up to 7-fold [1]. More recent models of attachment invoke a conformational wave mechanism to achieve tension-mediated changes in growth and shortening [15, 18, 19]. The most recent models of biased diffusion alone do not predict any effect of tension on growth or shortening rates [9, 20]. However, the presence of Ndc80 complexes alone on microtubules has been shown to decelerate microtubule shortening in a concentration-dependent manner [3], and artificial coupling of Ndc80 complexes reproduces this effect [20]. This is striking as the Ndc80 complex is thought to be a highly diffusive microtubule binder, not expected to exhibit behavior of a conformational wave-like coupler. All models of biased diffusion exhibit increases in the detachment rate for higher disassembly speeds or lower assembly speeds, therefore accounting for attachment-mediated changes in the growth or shortening rates is likely to improve the performance of biased diffusion couplers, especially at higher tension.

Recently, it was discovered that intact immunoprecipitated kinetochores exhibit strong asymmetry in sliding friction depending on the direction they are pulled along the side of a microtubule

(the lattice). While it is unknown how we can experimentally modify elements of the kinetochore to change this asymmetry, we can use modeling to investigate the role of this grip-strength asymmetry in tip-attachment. In biased diffusion models, the sensitivity of the stepping rate of individual diffusors to force is a primary determinant of the detachment rate [12]. It is likely that incorporating asymmetry into the stepping rates in biased diffusion models will change the predicted relationships between applied load and detachment rate of the overall complex.

While biased diffusion models have been shown to account for attachments to both assembling and disassembling tips, these models have yet to explain the behavior exhibited by intact kinetochore complexes attached to microtubule tips in vitro. Common deficiencies of these models include high force sensitivity, poor performance at higher forces, a lack of sensitivity to the affinity of the individual diffusive proteins in the complex, and a lack of feedback on microtubule dynamic rates. Some of these deficiencies have been remediated by inclusion of experimentally observed phenomena into recent models. Here, we explore how including flexibility, lattice sliding asymmetry, and feedback on microtubule dynamic rates affect biased diffusion models, with development of these models for comparison to experimental data. Rather than extrapolate from bulk data or measurements of kinetochore movements, the parameters used to constrain kinetochore component behavior here are derived from a wealth of single-molecule data that has become available for kinetochore components in the past decade. We focus on developing models to describe the behavior of yeast kinetochore-microtubule interactions, because the most biophysical data has been captured for both the complex as well as its protein constituents.

Results

Criteria for developing and evaluating models of biased diffusion

The models developed here are compared to quantitative data captured from optical trapping experiments. In these experiments, single yeast kinetochores were attached to beads. These beads were placed on the tips of dynamic microtubules; the optical trap was then used to exert continuous tension on the attachment, and the lifetimes of the attachments were quantified [1]. Criteria to evaluate our models can be developed from these experiments. First, the detachment rate (inverse of lifetime) should be sensitive to force and should change 2-3 orders of magnitude across a range of 1-15 pN. Second, the difference between lifetimes for assembling and disassembling microtubules should be within 2-3 orders of magnitude. Third, the detachment rate should exhibit moderate, but not drastic sensitivity to the number of microtubule binders or their individual affinities for the lattice. Kinetochores in vitro (and likely in vivo as well) are inherently low-copy number complexes. Therefore, to exhibit robust attachment behavior, the exact number or quality of microtubule binders in the complex should not be crucial to the function of the overall unit. Said another way, the kinetochore should not have its function lost if one of its many microtubule-binding domains mis-folds or loses function. To compare model results to these criteria, we will predict the detachment rate for several applied loads and several microtubule binder copy numbers for each model.

The first model to show biased diffusion could account for attachment to both assembling and disassembling microtubule tips was published by Terell Hill in 1985 [12]. This model was developed to describe the attachment of mammalian kinetochores to spindle microtubules, and was extended by Joglekar and Hunt later to incorporate updated biophysical data to constrain the model parameters [13].

These models rest on several key assumptions: the kinetochore is assumed to be composed of many binders of microtubules, and these binders are rigidly linked such that they move along the microtubule lattice (and off the tip) together. The bonds between the simulated kinetochore and microtubule are force-sensitive interactions modeled with Arrhenius kinetics to describe transitions between states.

To develop this model to simulate attachment properties of yeast kinetochores, we estimate the parameters from known single-molecule data that describes yeast Ndc80 complex and Dam1c diffusion. Table 1 shows the values of these parameters and expected range given data from the literature. There are several different microtubule lattice binding proteins in the kinetochore including Ndc80, Dam1, and Stu2. However, the Ndc80 complex is known to be the primary mediator of microtubule binding. Table 2 gives a range of experimentally measured values for the diffusion coefficient of Ndc80c and Dam1c on the microtubule lattice, ranging from $1.5 \cdot 10^4$ to $5 \cdot 10^4$ $nm^2 \cdot s^{-1}$ [3, 4, 21]. These values were measured from diffusion of single fluorescently labelled proteins on intact microtubules in-vitro. The parameters κ (the stepping rate of a single diffusor without force) and the diffusion coefficient D can be calculated directly from this data. The parameter s (the kinetic parameter for a diffusor leaving the lattice tip) can be calculated from fluorescence measurements of k_{off} and the parameters κ and r. A Kramer's rate theory was used to estimate the energy landscape roughness parameter r from the same single-molecule fluorescence data. Importantly, our calculation of the energy landscape roughness parameter $r = 4.5 \cdot 10^{-5}$ differs substantially from assumptions by Hill [12] and Joglekar and Hunt [13], where $0.8 < r < 0.96$.

A molecular roughness factor of $r \sim 10^{-5}$ is much smaller than Hill's or Joglekar and Hunt's choices of r~ 0.8 or 0.96, indicating the energy landscape roughness is likely significantly higher than assumed by Hill or Joglekar. This suggests that for each additional lattice binder simulated in the kinetochore, the stepping rate of the complex decreases by a multiple of 10^{-5}. This large barrier for movement makes the simulated kinetochore extremely sensitive to the number of lattice binders in the kinetochore, in conflict with the requirement for robustness to compositional heterogeneity we established at the beginning of this modeling effort. We obviate this defect here by choosing relatively small numbers the lattice binders for the simulated kinetochore (2-5), which may anyway be an accurate portrayal of the number of Ndc80 complexes in the immunoprecipitated yeast kinetochores for which we have biophysical data [1]. That the data-informed molecular roughness estimate is so low suggests that a key assumption of the Hill model, that the diffusors are rigidly linked, may be a poor assumption. If the couplers are flexibly linked, there is no need for them to transit the corrugated landscape in simultaneous steps, and the stepping rate would not depend on the roughness parameter r raised to the power of M.

Modelling of sliding asymmetry

We can model asymmetry in the sliding friction of biomolecules on a polymer by assuming the diffusor steps on a corrugated energy landscape with slanted peaks, rather than symmetric peaks [22]. In this asymmetric periodic energy landscape, the stepping rate in the absence of force is required to be equal, so as not to violate the first law of thermodynamics. Therefore, any changes to the rate constants as a result of the landscape tilt are captured within the term describing the effect of force on kinetic rate constants. In a symmetric energy landscape, the distance to the transition state is the same in either direction, and therefore the work done in either direction under the same force is identical, and the rate constant for the effect of force is identical regardless of direction. However, in an asymmetric corrugated

energy landscape, the distance to the transition state is different depending on the direction traversed. We can describe this difference with a parameter δ, where the modified rate constant is $f = e^{f(\ell/2 \pm \delta)/k_B T}$.

To obtain reasonable estimates for asymmetry parameter δ, we can directly fit optical trapping data. This data was gathered by attaching immunoprecipitated yeast kinetochores to polystyrene beads, attaching them to microtubules tethered to a slide surface, and then dragging the beads along the length of the microtubule back and forth at fixed forces (figure 1a). The velocity-force relationship can be fit by an expression for force-induced drag of a Hill-like coupler along a lattice (equation 2, figure 1b). The prefactor κr^M corresponds to a kinetochore composed of M couplers that if alone, would diffuse along the lattice with step size ℓ at rate κ. The first exponential represents the rate for the forward step, and the second exponential represents the rate for the reverse step, both a function of the applied force. Given a known step size, the term κr^M is fit as a single parameter (M is not known), and δ is the second free parameter. For a step size of 8.2 nm, the average fitted asymmetry parameter was found to be δ = -3.3 nm (figure 1d-g). We can non-dimensionalize the parameter δ by dividing by the step size, to yield $\delta^* = -0.40$. This suggests the peak in the corrugated energy landscape is offset by 40% of the step distance towards the minus-end of the microtuble, a significant asymmetry.

$$v = \ell \kappa r^M \left(e^{F\left(\frac{\ell}{2}+\delta\right)/k_B T} - e^{-F\left(\frac{\ell}{2}-\delta\right)/k_B T} \right) \qquad \text{Equation 1}$$

Given we have so far obtained estimates for κ, r, and we can test a variety of values for ℓ, it is tempting to estimate the number of binders M in a kinetochore given our fitted value for κr^M (figure 1c). For step sizes of 4.1 and 0.615 nm, values of M are predicted to be 1.2 and 1.3 respectively. We certainly expect more than one Ndc80 per kinetochore particle in our experiments, as single Ndc80 complexes are poor couplers to microtubule tips [23]. The most reasonable conclusion is that the Ndc80 couplers in the kinetochore do not all transit the corrugated energy landscape of the microtubule simultaneously, as a rigidly linked Hill-like coupler would.

A Hill model for microtubule-kinetochore detachment with parameters defined by single-molecule data

The rate constants described above can be used to generate a linear Markov chain model that simulates kinetochore movement along the lattice and off the tip under the influence of external force. The combinations of rate constants for each forwards and backwards step are shown in figure 2a, and follow the convention of Hill et al. 1985 [12]. We can use the method of Barhim and Klafter to analytically determine the first passage time (time to detachment) [24], and also calculate the first passage time numerically by Monte-Carlo simulation.

The numerical solution yields single-kinetochore position versus time traces, shown in figure 3a. For a kinetochore with three diffusors on an assembling microtubule tip experiencing forces of 10 and 15 pN, a negative asymmetry factor produces longer lifetimes than a symmetric energy landscape. To compare predicted detachment rates to experimental data, we can plot the analytical solution for detachment rate as a function of force for the assembling (figure 4a) and disassembling (figure 4b) tip. Overlayed onto these plots are single-exponential fits to the force clamp data gathered in Akiyoshi et al. 2010 for immunoprecipitated kinetochores attached to dynamic microtubule tips. For the Hill model with parameters informed by single-molecule data, the detachment rate is highly sensitive to force, and for

assembling tips transits a range of 20 orders of magnitude between 2.5 and 15 pN, far larger than the range spanned by the experimental data. Additionally, the predicted detachment rates are many orders of magnitude lower than the real data for forces lower than 7 pN. The predicted detachment rates for disassembling tips are constrained in a narrower range across all forces tested, but still span a larger range than the experimental data.

Likewise, the detachment rate is predicted to be highly sensitive to the number of simulated diffusors in the kinetochore for assembling microtubules (figure 5a). The detachment rate for disassembling tips is less sensitive to the number of binders, especially for negative asymmetry values. In summary, a Hill model constructed using parameters informed by single-molecule biophysical data exhibits strong sensitivity to both the applied load and the number of binders in the simulated kinetochore, making it a poor fit for the known behavior of kinetochore-microtubule attachments in vitro.

While the predicted detachment rates are sensitive to variations in the asymmetry factor, no value of the asymmetry factor improves performance of the models for both assembling and disassembling tips. However, negative values of the asymmetry factor desensitize the detachment rate to the number of binders in the kinetochore (figure 5b), remediating performance of the Hill model in this narrow aspect. Finally, local parameter variations for the assembling (figure 5, figure supplement 1), and disassembling (figure 5, figure supplement 2) tip Hill models, confirm the broad insensitivity of the Hill model to many of the underlying parameters [9, 10]. Exceptions to this sensitivity include the step size (constrained by lattice spacing), and to a lesser degree the molecular roughness factor *r*.

For comparison, we produced analytical solutions for the Hill model with parameters chosen by Joglekar and Hunt [13]. This model exhibits many of the same defects as the Hill model informed by single-molecule biophysical parameters discussed earlier. The detachment rate exhibits high sensitivity to force for both assembling and disassembling tips, transiting 60, and 6 orders of magnitude respectively as the force was varied between 1 and 20 pN (figure 6a,b). Likewise, the detachment rate is highly sensitive to the number of binders in the kinetochore, especially for assembling tips. We can conclude that the sensitivity of the detachment rate to force and the number of binders in the simulated kinetochore is likely intrinsic to the Hill model, independent of choices for parameters, a finding substantiated by the literature [9, 13].

An analytically tractable, more flexible Hill model variant

To simulate a more flexible kinetochore, we can assume that the individual subunits in the kinetochore have sufficient flexibility to step independently of their neighbors. To retain analytical tractability, we restrict these steps to a “millipede-like” motion, depicted in figure 2b. Individual traces for such a coupler, under various loads and simulated for several asymmetry factors are shown in figure 3b-c. Like the original Hill model, negative asymmetry factors produce longer lifetimes for assembling attachments (figure 3b) than a model with a symmetric landscape (figure 3c). As our model remains analytically tractable, we can use the analytical solutions to describe the behavior of the detachment rate as a function of force for assembling (figure 4e), and disassembling (figure 4f) microtubule tips. For the assembling tip, the “millipede Hill” model produces detachment rates that closely match the in-vivo rates for forces above 6 pN. However, the predicted detachment rate remains far below experimentally determined rates for forces below 6 pN. For disassembling tips, the “millipede Hill” coupler is not nearly

as sensitive to force but predicts detachment rates three orders of magnitude higher than the experimentally determined rates.

The detachment rates predicted by the “millipede Hill” model remain highly sensitive to the number of couplers in the simulated kinetochore for assembling tips, albeit slightly less than the original Hill model. During disassembly, the “millipede Hill” predicts detachment rates that are insensitive to the number of couplers in the disassembling tip, but persistently elevated many orders of magnitude above experimentally measured rates. In summary, while the “millipede Hill” model remedies some of the sensitivity of the detachment rate to force that is characteristic of the original Hill model, the model still produces large differences in predicted vs. experimentally measured detachment rates for the assembling tip and persistently higher than experimental detachment rates for disassembling tips.

Modelling of force-feedback on microtubule dynamic rates

Kinetochores attached to microtubule tips dramatically alter the rate of assembly and disassembly based on the amount of tension exerted through the attachment [1]. Though the magnitude of this behavior exhibited by intact kinetochores has yet to be fully explained, binding of Ndc80 alone [23], and Dam1c alone [4] to microtubules can slow or halt disassembly respectively. We can account for this effect in our models in two ways: we can reduce the disassembly rate parameter as force is increased, based on experimentally measured values. Alternatively, we can assume that when a kinetochore subunit is bound at the terminal tubulin, this tubulin is prevented from leaving the lattice, changing the series of rate constants that make up our model (figure 2c). We move forward with the latter method as this is mode of force-feedback on the dynamic rates is driven directly from behavior of the individual components in the complex rather than measurements from the whole complex. The relationship between the detachment rate and force are shown for both the Hill model modified with this assumption (figure 4c, d), and the “millipede Hill” modified with this assumption (figure 4g, h). For the original Hill model, this change transfers the depressed detachment rate at lower forces observed for the assembling tip to the disassembling tip, with few alterations. The same behavior is observed for the “millipede Hill” model. Though this modelling choice does bring predictions of detachment rates closer together for assembling and disassembling tips, a change needed to match experimental data, the assumption that no disassembly occurs with a terminally bound kinetochore is drastic. If this phenomenon occurs for real attachments, it is possible that the departure of terminal tubulins in the lattice is only partially suppressed by the presence of a bound kinetochore component. However, modeling such a partial suppression remains an effort for future work.

A model with flexible, independently diffusing elements and sliding asymmetry fits experimentally determined detachment rates for assembling tips

Our semi-flexible “millipede Hill” model remedied some of the deficiencies of the original Hill model. The assumptions for this model formulation conferred a limited flexibility to the kinetochore. We can model additional, tunable flexibility in the kinetochore as well. To do this we develop two models. The first model we call the “diffusors in a box” model. There, individual lattice binders are confined to a box of width $2w$ along the microtubule (figure 7a). At each time step, the box position is updated to the mean position of the couplers, so long as leading or lagging couplers are not left behind. By varying the box width, we vary the simulated flexibility in the kinetochore. In the second model, we couple each diffusor to the mean position with a simulated spring with spring constant k (figure 7b). By varying the

spring constant, we vary the flexibility of the kinetochore. Neither of these models are analytically tractable with the tools we relied on earlier, and we turn to Monte-Carlo simulation to predict detachment rates as a function of force and number of binders in the kinetochore.

The box width of the flexible coupler does not appear to have a large impact on detachment rates, suggesting the specific flexibility of the coupler is not critical (figure 8). However, the detachment rates predicted by the diffusor in a box model differ from the Hill and "millipede Hill" models described earlier and better match experimental data. The drop in detachment rates (far below that observed experimentally) for assembling tips at low forces is no longer observed, bringing the predicted detachment rate for assembling tips in close agreement with experimental data. Sliding asymmetry also appears to be important for reducing the sensitivity of the detachment rate to force for the assembling tip; With higher friction towards the tip, the 'diffusors in a box' model achieves a close match to experimental data during microtubule assembly (figure 8a,b). However, the predicted detachment rates for disassembling tips for this model remain elevated above experimentally observed rates.

Slowing the disassembly rate as force is increased confers agreement to experimental data for disassembling tips

For the 'diffusors in a box' model results shown in figure 8, the disassembly and assembly speeds were held constant across all forces as they were in previous models whose predictions are shown here (figure 9a). However, in-vitro experiments with immunoprecipitated kinetochore particles show the disassembly speed of microtubules is reduced up to seven-fold with increasing load (figure 9c) [1]. For the same 'diffusors in a box' model, if the disassembly speed is reduced as force is increased according to experimentally measured data, the predicted detachment rates fall well within the range of experimentally measured detachment rates (figure 9d). Apart from a different number of diffusing elements in the kinetochore, this model achieves excellent agreement to experimental data for assembling tips across the range of forces tested experimentally (1-15 pN), and predicts detachment rates in the same order of magnitude of experimentally measured values for disassembling tips. It is reasonable to assume that small changes to the model, perhaps consideration of other experimentally measured properties of individual kinetochore subunits, could fit the experimental data closely.

Discussion

In this modeling effort, we explored how including flexibility, drag asymmetry, and feedback on microtubule dynamic rates change predictions of biased diffusion models. The flexibility of the simulated kinetochore was varied by generating a series of model variants, from the original Hill model (least flexible), to the "millipede Hill" (more flexible), to the "diffusor in box" and "diffusors coupled by springs" models (most flexible). The asymmetry in the sliding of kinetochores on microtubules was simulated by changing the force sensitivity of the stepping rates of individual lattice binders in a direction-dependent manner. Finally, tension-based feedback on microtubule dynamic rates was incorporated indirectly by suppressing disassembly when a kinetochore was localized to a terminal tubulin in the lattice or directly by changing the disassembly speed as a function of force according to experimental data.

Incorporation of sliding asymmetry into biased diffusion models markedly changed predicted detachment rates. In most cases, a negative asymmetry factor (higher friction when pulling towards a microtubule plus-end) was associated with lower detachment rates, suggesting this biophysical feature could be important for playing a role in attachment stability. In some models, a more negative

asymmetry factor increased detachment rates for disassembling tips, but this effect was ameliorated by preventing microtubule disassembly when a kinetochore was bound to the terminal tubulin. In nearly all the models, a more negative asymmetry factor was correlated with a lower sensitivity of the detachment rate to force, increasing agreement between detachment rates predicted by the biased diffusion models shown here and experimentally measured detachment rates. The reduction in detachment rate sensitivity conferred by a negative asymmetry factor was key to the close fit to experimentally determined detachment rates for assembling tips achieved by the final model shown here (figure 8a,b).

Inhibiting microtubule disassembly when a kinetochore subunit was bound at the terminal tubulin did not affect detachment rates predicted for assembling tips (as expected) but led detachment rates for disassembling tips to mimic those predicted for assembling tips. For biased diffusion models without this assumption, microtubule disassembly increases the detachment rate by ejecting kinetochores at the tip of the microtubule at a rate higher than they would normally detach on their own. Eliminating this path to detachment eliminates most of the effects of disassembly on detachment rate. As assembly is relatively slow to disassembly, a markedly slowed disassembling tip is similar to an assembling tip. The actual rate of disassembly with this assumption is likely well below that specified by the parameter β. It is probably more realistic to assume that the presence of the kinetochore reduces rather than eliminates the departure of tubulin subunits from the tip during disassembly. In future versions of these models, a tunable parameter that describes a likelihood of terminal tubulin departure with an attached kinetochore could be added. The disassembly rate could also be reported. Overall, incorporating tension-based feedback on the disassembly rate brings the predicted detachment rates for assembling and disassembling tips closer together, a change needed for biased diffusion models to fit real data.

Increasing flexibility of the simulated kinetochore in all cases decreased differences between predicted detachment rates and detachment rates observed experimentally. Broadly, more flexibility appears to be correlated with less sensitivity to force, an essential feature of the experimental data relative to the high sensitivity of the original Hill model. Also of note, negative sliding asymmetry (that is harder to pull a kinetochore towards the plus-end of a microtubule) increases agreement between model and experimental data in the most flexible model. This suggests sliding asymmetry, a previously unknown biophysical characteristic of kinetochore proteins, might play a critical role in preventing detachment from microtubule tips at higher forces during microtubule assembly.

In each case, incorporating more flexibility, sliding asymmetry, and feedback on disassembly rate, improved the performance of biased diffusion models as benchmarked against in-vitro detachment rates for intact kinetochores. Additionally, incorporation of each of these biophysical features led to relatively large changes in predicted detachment rates, suggesting biased diffusion as a mechanism for microtubule-kinetochore attachment is likely to benefit greatly from a more careful consideration of the single molecule properties of the proteins that make up the kinetochore. Furthermore, this work suggests that a biased diffusion model with the aforementioned biophysical features could explain detachment rates across different loads for both assembling and disassembling microtubule tips.

Several challenges remain for future modeling efforts. We have chosen to model the Ndc80 complex and Dam1 complex as diffusing elements in a simulated kinetochore. This assumption was based on evidence from TIRF microscopy, showing that both protein complexes bind to and diffuse across microtubule lattices [4, 23]. However, there are other proteins in the kinetochore that have a

significant impact on the detachment rate, whose mechanistic role remains unclear. Stu2 is a TOG-domain ortholog of mammalian XMAP215 that normally acts as a microtubule polymerase at microtubule tips [6]. It binds to and is essential to the catch-bond behavior of the kinetochore, but does not act as a polymerase in this context [2]. A mechanistic understanding of this phenomenon will be needed before the role of Stu2 can be defined in models such as those developed here. Additional features that could be incorporated into these models include a more realistic view of bridging interactions amongst kinetochore subunits, such as that explored by Zaytsev et al [9], tension-mediated acceleration of the assembly rate, or a conformational wave and biased diffusion hybrid model.

Methods

Parameter Selection:

Hill argued that the mean step size was a result of a rotationally symmetric coupler transiting along the microtubule; accordingly, the step size for such a coupler would be the lattice spacing divided by the number of protofilaments (8/13 nm), or 0.615 nm. The lattice spacing could also be interpreted to be the tubulin monomer or dimer spacing, depending on the lattice binder in question. Structural studies suggest Ndc80c binds at the monomer interface, therefore 4nm was chosen as a lattice spacing for the yeast kinetochore model here.

The energy landscape for a diffusor on the microtubule lattice can be described as corrugated, with a characteristic trough-to-peak height "b". The rate of barrier crossing can be described with Arrhenius kinetics, where the rate of crossing is proportional to the exponential of the ratio of the barrier height to the mean thermal energy, $r = \mathrm{e}^{-b/k_BT}$. Because the Hill model assumes these diffusors are rigidly linked together, they must transit peaks in the corrugated energy landscape simultaneously. The rate of stepping for the whole complex is therefore r^M, where M is the number of diffusors engaged with the lattice. For values of $b \gg k_BT$, the overall stepping rate is dramatically reduced as the number of couplers grows, quickly locking the coupler onto the lattice and halting diffusion. For this reason, Hill assumed the molecular roughness factor was moderate, $r = 0.8$; Joglekar and Hunt chose an even more moderate molecular roughness factor $r = 0.96$. With new single-molecule data for the diffusion of Ndc80c on microtubules, we can directly estimate the energy barrier height b and molecular roughness factor r. We use a formulation of Kramer's rate theory for the first-passage time of an overdamped diffusor in a potential well over a potential barrier, borrowing an approach used to calculate energy barrier height of lattice corrugations for the kinesin Kip3p (Equation 1) [22, 25]. This formulation calculates the energy barrier height by comparing the time the diffusor takes to travel the step distance in the periodic landscape to the time the diffusor takes to travel the same distance without any barriers. We assume the free diffusion coefficient of Ndc80c in solution is approximately the same as that of the motor Kip3p as they are both elongated structures with globular domains near their ends and have similar molecular weights (187 vs. 180 kDa). The free diffusion of Kip3p has been evaluated by fluorescence-correlation spectroscopy to be 20 ±2 μm2·s-1 [22]. The drag coefficients γ_{TIRF} (for the microtubule-bound protein) and γ_{FCS} (for the free protein) can be directly estimated from the diffusion coefficient by the Einstein relation $\gamma = k_BT/D$. To account for surface interaction effects that increase the observed friction of a diffusor near a surface, a parameter λ is introduced. We use a range of $\lambda = (1, 3, 15)$ to account for any differences in surface effects. A $\lambda = 3$ corresponds to a Faxen's law approximation for a sphere near a surface. A numerical solution to equation 1 gives energy barrier

heights b of 10 – 12 kBT for the diffusion of a single Ndc80c along the microtubule lattice, and a corresponding landscape roughness factor r of 6.1·10-6 to 4.5·10-5.

$$\frac{\gamma_{TIRF}}{\gamma_{FCS}\lambda} = \frac{\sqrt{\pi}}{16}\left(\frac{k_B T}{b}\right)^{3/2} \exp\left(\frac{b}{k_B T}\right) \qquad \text{Supplemental Equation 1}$$

As the simulated kinetochore complex slides off the microtubule tip, individual bonds between the lattice and the proteins in the kinetochore are broken. We again model the rate of this transition with Arrhenius kinetics, where the rate of crossing a barrier of height w is given by the exponential of the ratio of the barrier height to thermal energy, $s = e^{-w/k_B T}$. The off-rate of a single lattice diffusor can be used to calculate s, with the relation $k_{off} = \kappa r s$, where r and κ are known quantities. The off-rate of a single lattice binder from the side of the lattice can be determined from single-molecule fluorescence data. We choose the single-molecule off-rate for Ndc80 in the presence of Dam1c, as this most likely corresponds to the off-rate of Ndc80 in the kinetochore complex, 6.2·10-2 s-1. This is not so different from the choice made by Hill or Joglekar and Hunt, s = 7.9·10-2 s-1 and s = 9.7·10-2 s-1 respectively.

The number of lattice binders in a yeast kinetochore is much smaller than that in the human kinetochore. Unlike the human kinetochore, the yeast kinetochore only binds a single microtubule. Estimates of the number of Ndc80c copies per kinetochore range from as low as three to a maximum of twenty-four [7]. We choose to run our models for a small number of Ndc80c copies (2-5) as that number reflects what has been measured using single-molecule fluorescence for our immunoprecipitated kinetochores [1], (unpublished data).

To account for microtubule assembly and disassembly, we introduce two parameters, α and β. These parameters are non-dimensionalized by dividing by the step size ℓ. The assembly rate of a microtubule with a tip-attached kinetochore ranges from 5 to 22 nm·s-1, depending on the level of tension [1]. We chose an intermediate value of 12 nm·s-1. The disassembly speed of microtubules ranges from 25 to 175 nm·s-1, depending on the level of tension [1]. We chose an intermediate level of 150 nm·s-1.

Crucial to the predictive power of these models is the ability to forecast the detachment rate as a function of force. Force in molecular bonds exponentiates the off-rate [26]. We can account for the effect of force by discounting the bond energy keeping the coupler in its current position by the amount of work done at the current level of force F to move the coupler one half-step, $W = F \cdot \ell/2$, with rate constant $f = e^{F \cdot \ell/2k_B T}$.

Methods for model solution

The combinations of rate constants for each forwards and backwards step are shown in figure 2a, and . We wish to calculate the time to coupler detachment, or the first passage time. For a linear Markov chain without position-dependent rate parameters, we can use the method of Barhim and Klafter to analytically determine the first passage time [24]. We also calculate the first passage time numerically by Monte-Carlo simulation. In the numerical simulation, a random variable is generated that determines which state to move to next, based on the known rate constants. The time between each step is dynamic, varied to match the expected rate of any given step, and exponentially distributed through time: $\tau = \frac{1}{\sum_i \nu_i} e^{\xi}$, where vi are the rates for each of the steps, and ξ is a continuous random variable. The

numerical solution can be computationally costly for slow couplers, or for simulations where the individual steps are fast, but the detachment of the coupler is slow. Therefore, if the analytical solutions match the numerical solutions, it is preferable to use the analytical solution for parameter variation, especially for simulations where the parameters yield a model with slow detachment. The numerical solutions match the analytical solutions well in all cases tested, so we show the analytical solutions unless the model assumptions make analytical solution intractable with the tools at our disposal.

Diffusion Coefficient ($nm^2 \cdot s^{-1}$)	Source	Description	Drag coefficient ($pN \cdot s \cdot nm^{-1}$)
1.50E+04	Umbreit 2012	Ndc80 on lattice	2.74E-04
5.00E+04	Tien 2010	Ndc80 on lattice	8.23E-05
1.50E+04	Tien 2010	Ndc80 + Dam1c on lattice	2.74E-04
2.10E+04	Umbreit 2014	WT Dam1c on lattice	1.96E-04
1.70E+04	Umbreit 2014	Oligomerization deficient dam1c on lattice	2.42E-04
4.30E+03	Bormuth 2009	kip3p on lattice (smTIRF)	9.57E-04
2.00E+07	Bormuth 2009	kip3p free in solution (by FCS)	2.06E-07

Table 1: List of relevant diffusion coefficients for biomolecules on microtubule lattices or free in solution (kip3p). The drag coefficients were calculated using the einstein relation.

Parameter	Description	Value	Units	Range	Sources
M	Number of diffusors in the kinetochore	4	unitless	6-9	Joglekar 2008, Joglekar 2009, Johnston 2010
mp	Number of lattice positions minus the number of diffusors in the kinetochore, "sleeve penetration sites" by Hill model	35	unitless	5-65	Hill 1985
ℓ	lattice spacing	4	nm	0.615 - 8	Hill 1985
alpha	tubulin addition rate, normalized to the lattice spacing	25/ℓ	1/s	25/ℓ	Akiyoshi 2010
beta	tubulin loss rate, normalized to the lattice spacing	170/ℓ	1/s	25/ℓ - 170/ℓ	Akiyoshi 2010
r	molecular roughness factor, accounts for energy barrier between lattice sites	4.5e-5	unitless	4.5e-5 - 0.98	Hill 1985, this work
D	Single lattice binder diffusion coefficient	12000	nm^2/s	1.5E4 - 5E4	Umbreit 2012, Tien 2010, Umbreit 2014
koff	single-molecule off-rate	0.062	1/s	0062 - 1.2	Umbreit 2012, Tien 2010
F	Force applied to simulated kinetochore	3	pN	0.5 - 20	Akiyoshi 2010
trj	number of trajectories to average in numerical simulations	20	unitless	5-20	Thesis, A. Franck
tmax	Maximum time for numerical simulations	1E6	s	1e6 - 1e7	Thesis, A. Franck
delta	drag asymmetry factor	-1.65/l*4	nm	+/- ℓ	This work
q	Dimensionless flexibility factor	1,M	unitless	1 or M	This work
flex	for diffusor in box model, number of lattice spaces the diffusors are allowed to venture from the mean diffusor position.	5	unitless	1 - 7	This work
stiff	for diffusor in flex well model, stiffness of spring coupler between diffusors and mean diffusor position	5	pN/nm	0.5 - 10	This work

Table 2: Parameters for biased diffusion models informed by single-molecule biophysical data

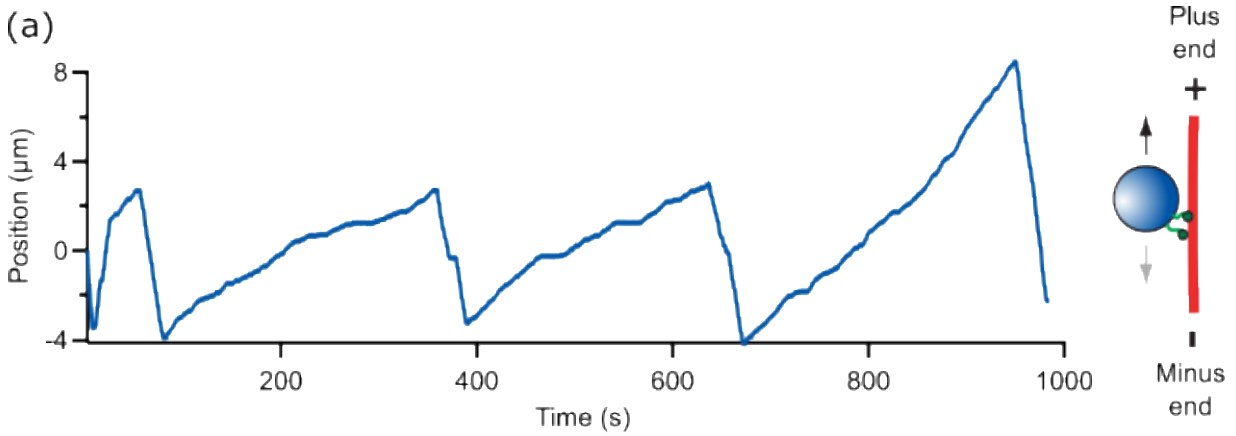

(b)

$$v = \ell \kappa r^M \left(e^{F\left(\frac{\ell}{2}+\delta\right)/k_B T} - e^{-F\left(\frac{\ell}{2}-\delta\right)/k_B T} \right)$$

$$\ell = 8.2\ nm$$

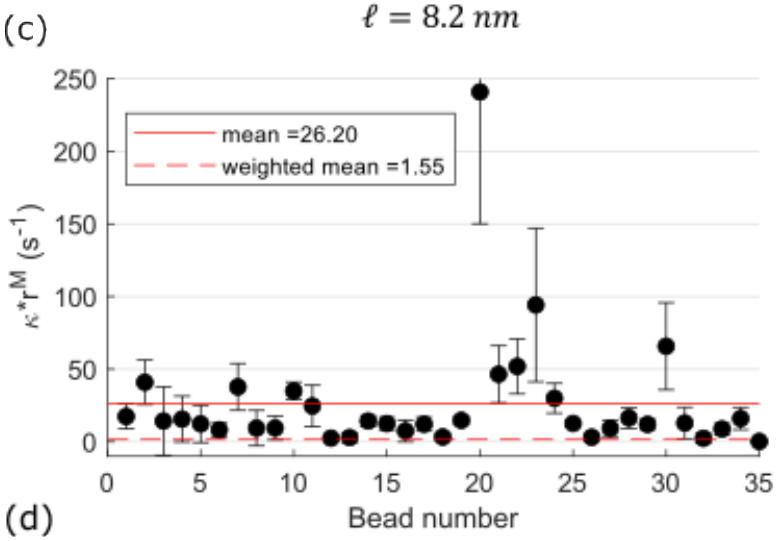

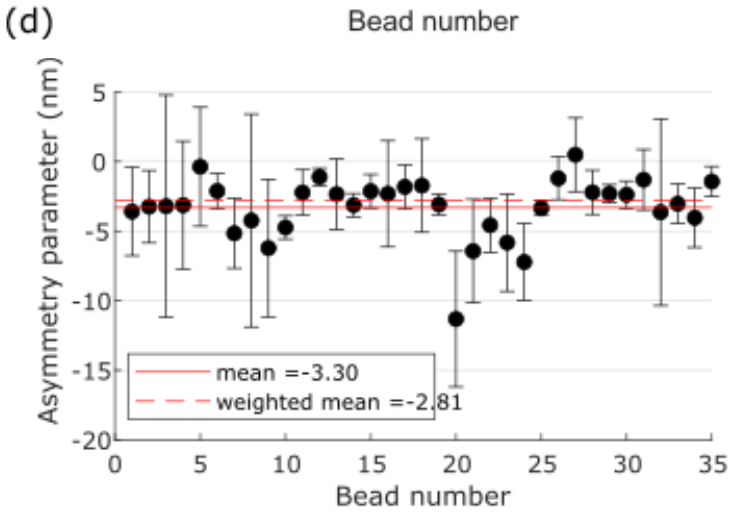

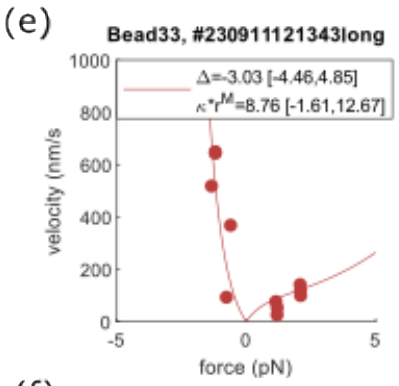

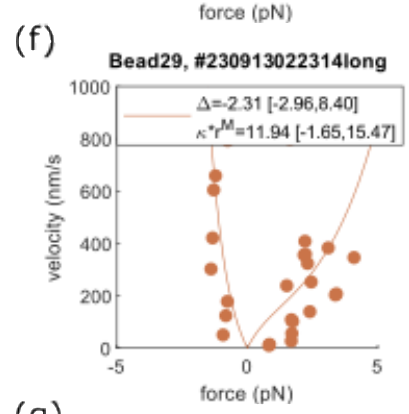

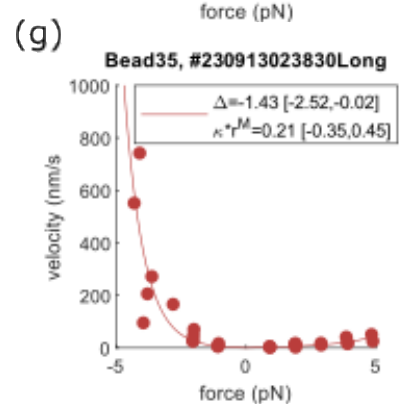

Figure 1: (a) Position versus time trace for a single bead dragged back and forth along a microtubule at a constant force of 1 pN. (b) A Hill model for friction of a multi-element microtubule binder, modified to account for binder asymmetry was fitted to velocity-force data for each bead. ℓ is the step size (8.2 nm), κ is the rate constant for stepping without force, r accounts for barrier to movement across the lattice, M is the number of diffusers within the modeled kinetochore, F is the applied load, and δ is the energy landscape asymmetry factor. Two free parameters are fitted from the model, the grouped set of parameters κr^M, and an asymmetry factor δ. (c) The fitted value for κr^M is plotted with a 95% confidence interval for each bead. The arithmetic mean is plotted as a solid red line, and the inverse-variance weighted mean is plotted as a dashed red line. (d) The fitted value for δ is plotted with a 95% confidence interval for each bead. The arithmetic mean is plotted as a solid red line, and the inverse-variance weighted mean is plotted as a dashed red line. (e-g) velocity vs. force for selected single beads, fitted with the drag model. Both fitted parameters are shown in the legend with associated 95% confidence intervals.

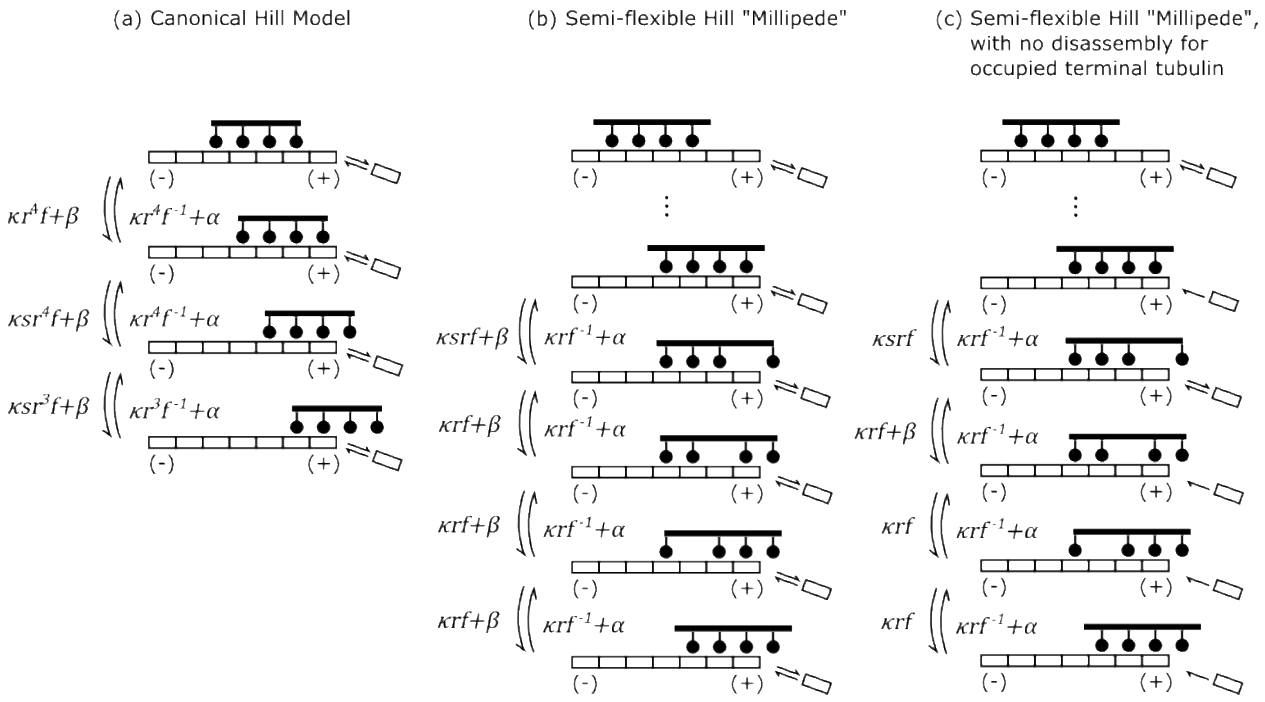

Figure 2: Three models for kinetochore detachment, with the rate constants show for each forwards and backwards step. (a) A canonical model by Terell Hill posits that the kinetochore is a set of binders rigidly linked together. Stepping involves all of the lattice binders stepping simultaneously. Tubulin dimers may leave or add to the tip during all states. (b) A variant of the Hill model where each lattice binder may move independently of the others. For analytical tractability, motion is restricted to a “millipede-like” stepping motion, depicted in the sequence of steps above. (c) The same “millipede” model as in (b), but accounting for attachment-based slowing of microtubule disassembly by preventing a terminal tubulin from leaving the lattice when a kinetochore subunit is bound.

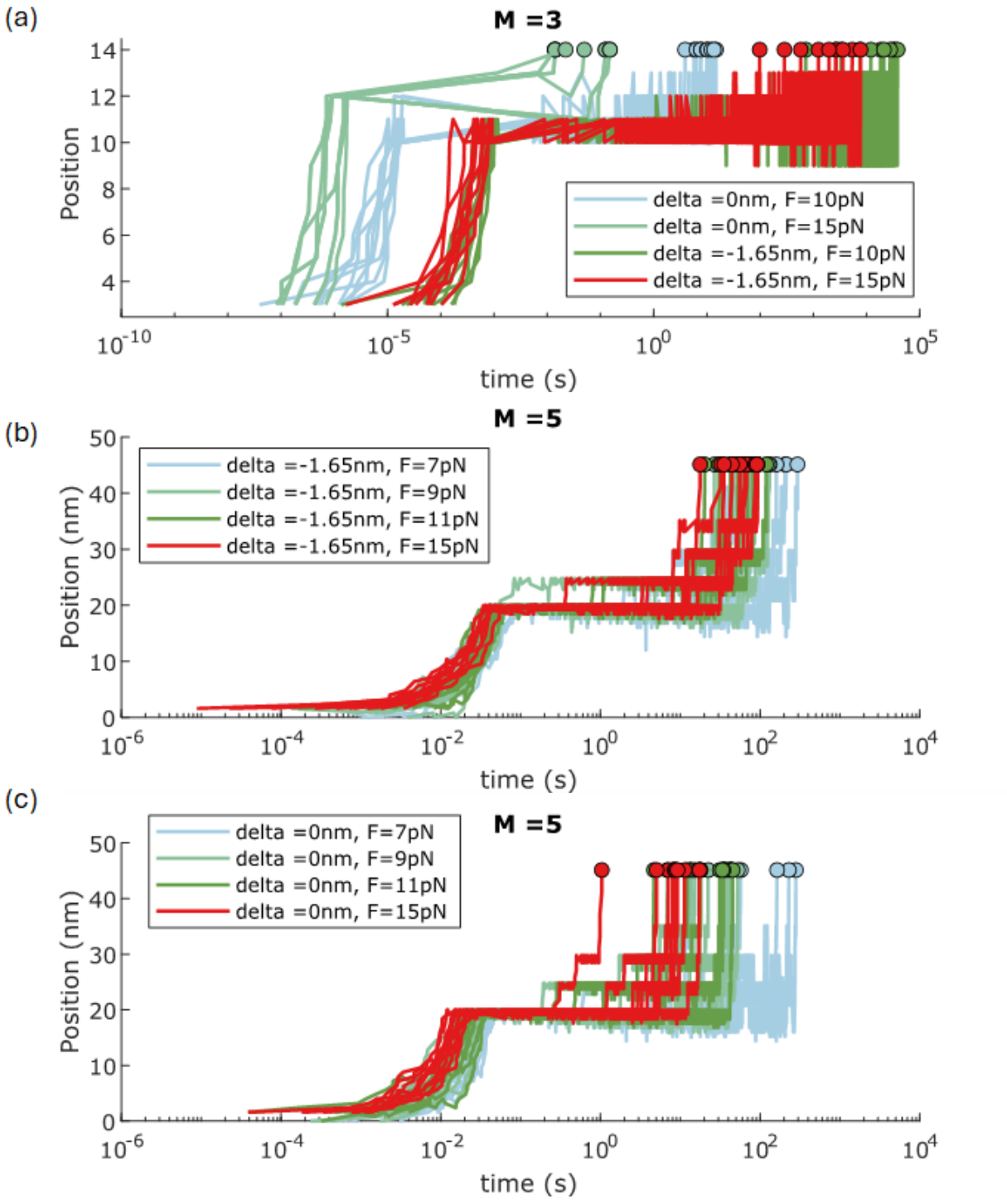

Figure 3: Simulated individual traces of detaching kinetochores for several models during microtubule assembly. (a) Position vs. time for a canonical Hill model with, and without asymmetry, for two different forces. (b-c) “millipede” Hill model for kinetochore detachment, showing position vs. time, with and without asymmetry. In both model types, a negative asymmetry factor increases time to detachment.

Figure 4: Analytical solutions for the detachment rate of simulated kinetochores from microtubule tips as a function of applied force. The detachment rates for immunoprecipitated kinetochores attached to real microtubule tips as measured in Akiyoshi et al. 2010 are overlayed on each plot for assembling (red) and disassembling (blue) microtubules. (a) Detachment rates for a canonical Hill model for an assembling tip. (b) Detachment rates for a canonical Hill model for disassembling tips. (c) Detachment rates for a canonical Hill model where presence of the kinetochore at the microtubule tip prevents disassembly, for an assembling tip. (d) Detachment rates for a canonical Hill model where presence of the kinetochore at the microtubule tip prevents disassembly, for a disassembling tip. (e) Detachment rate for a semi-flexible version of the f Hill model “millipede hill”, for an assembling tip. (f) Detachment rate for a semi-flexible version of the f Hill model “millipede hill”, for an disassembling tip. (g) Detachment rate for a semi-flexible version of the f Hill model “millipede hill”, where presence of the kinetochore at the microtubule tip prevents disassembly, for an assembling tip. (h) Detachment rate for a semi-flexible version of the f Hill model “millipede hill”, where presence of the kinetochore at the microtubule tip prevents disassembly, for a disassembling tip.

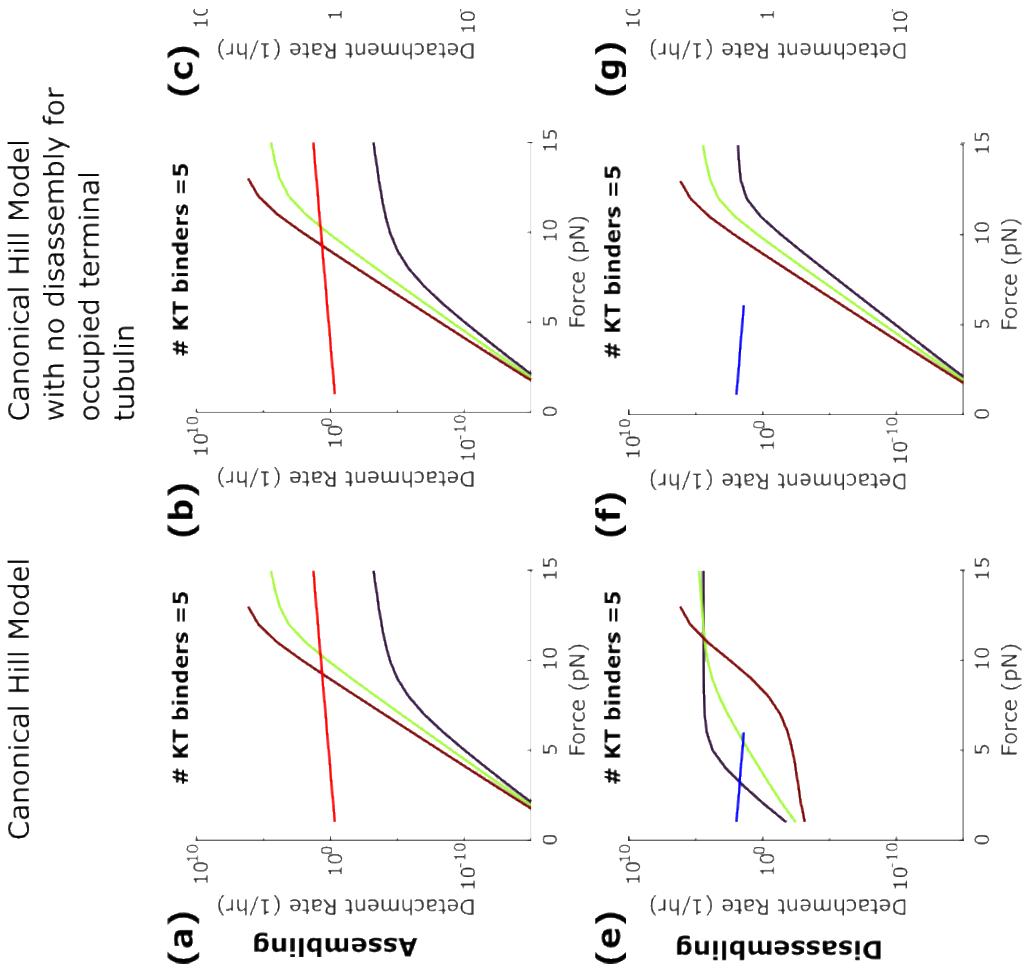

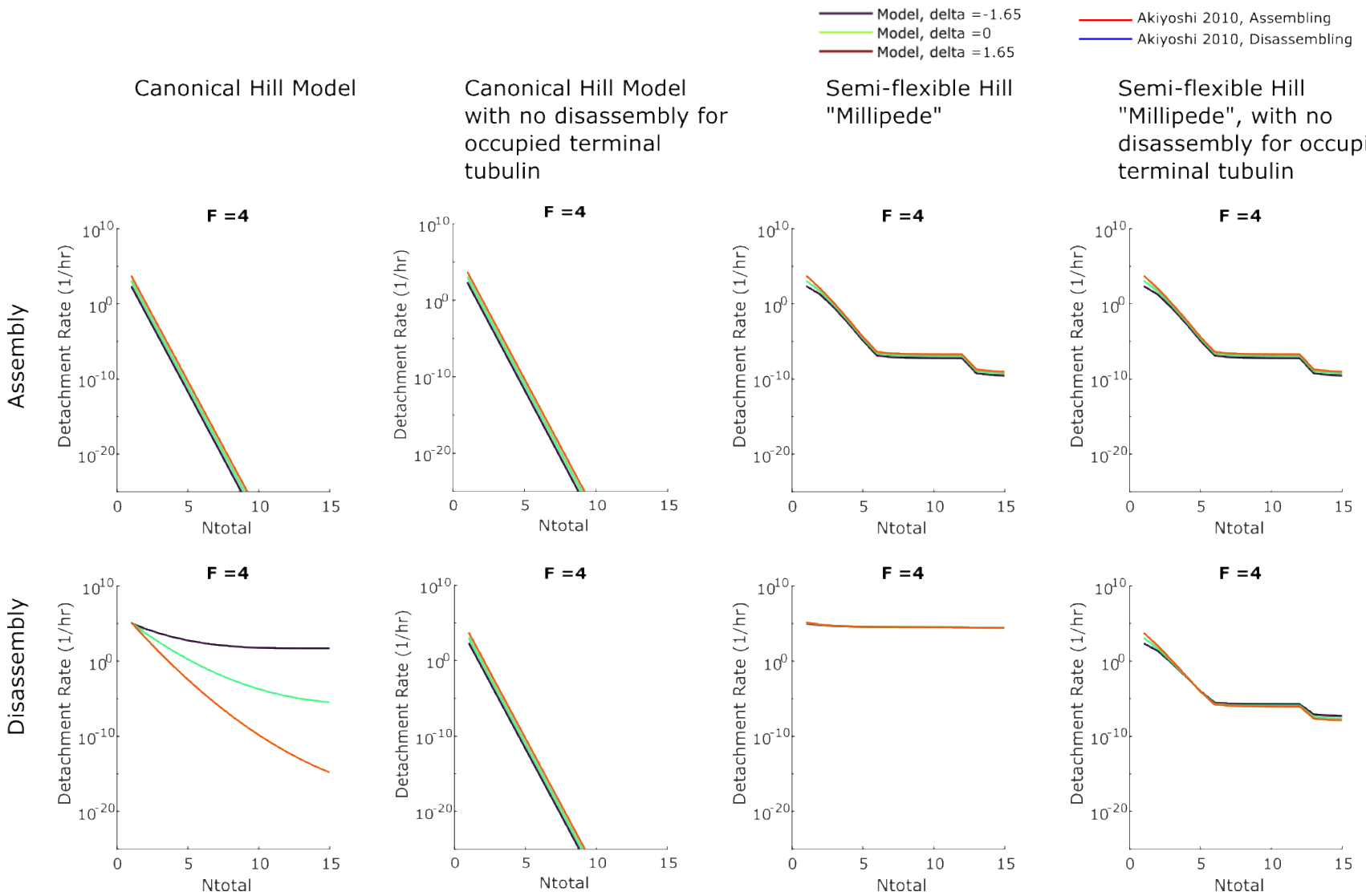
Model, delta =-1.65
Model, delta =0
Model, delta =1.65
Akiyoshi 2010, Assembling
Akiyoshi 2010, Disassembling
Canonical Hill Model
Canonical Hill Model with no disassembly for occupied terminal tubulin
Semi-flexible Hill "Millipede"
Semi-flexible Hill "Millipede", with no disassembly for occupied terminal tubulin
Assembly
Disassembly
F =4
Detachment Rate (1/hr)
Ntotal

Figure 5: Analytical solutions for the detachment rate of simulated kinetochores from microtubule tips as a function of number of binders in the kinetochore. (a) Detachment rates for a canonical Hill model for an assembling tip. (b) Detachment rates for a canonical Hill model for disassembling tips. (c) Detachment rates for a canonical Hill model where presence of the kinetochore at the microtubule tip prevents disassembly, for an assembling tip. (d) Detachment rates for a canonical Hill model where presence of the kinetochore at the microtubule tip prevents disassembly, for a disassembling tip. (e) Detachment rate for a semi-flexible version of the Hill model "millipede hill", for an assembling tip. (f) Detachment rate for a semi-flexible version of the f Hill model "millipede hill", for a disassembling tip. (g) Detachment rate for a semi-flexible version of the Hill model "millipede hill", where presence of the kinetochore at the microtubule tip prevents disassembly, for an assembling tip. (h) Detachment rate for a semi-flexible version of the Hill model "millipede hill", where presence of the kinetochore at the microtubule tip prevents disassembly, for a disassembling tip.

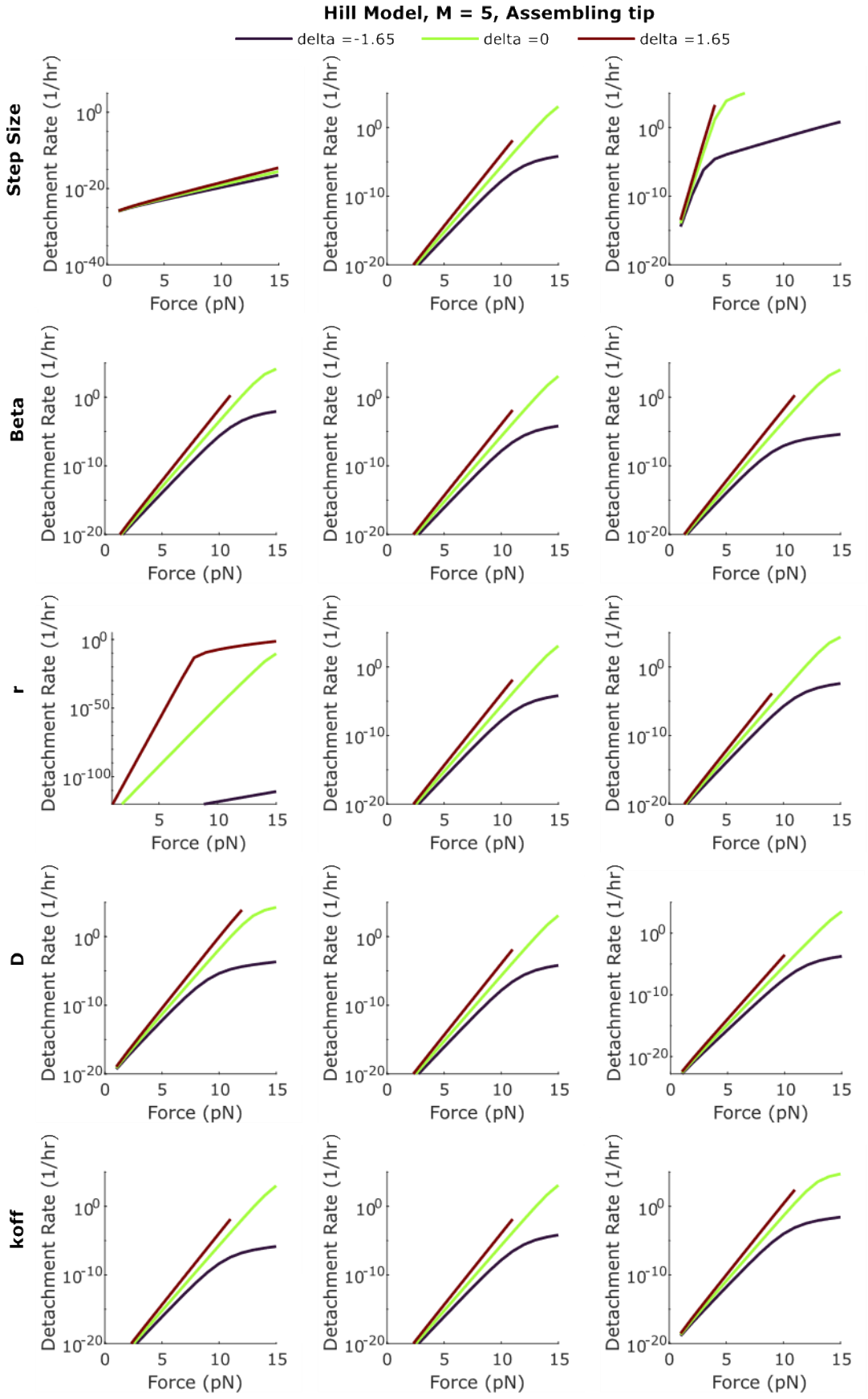
Hill Model, M = 5, Assembling tip
delta =-1.65
delta =0
delta =1.65
Step Size
Beta
r
D
koff
Detachment Rate (1/hr)
Force (pN)

Figure 5, figure supplement 1: Parameter variation for Hill Model, with an assembling tip. Plots of detachment rate as a function of force were generated. Each row contains plots for variation of a single parameter. The center-plot corresponds to the default parameter set, the left-most plot corresponds to an e-fold reduction in the parameter, the right-most plots correspond to an e-fold increase in the parameter. The Hill Model remains largely insensitive to all parameters but the step size and molecular roughness factor r.

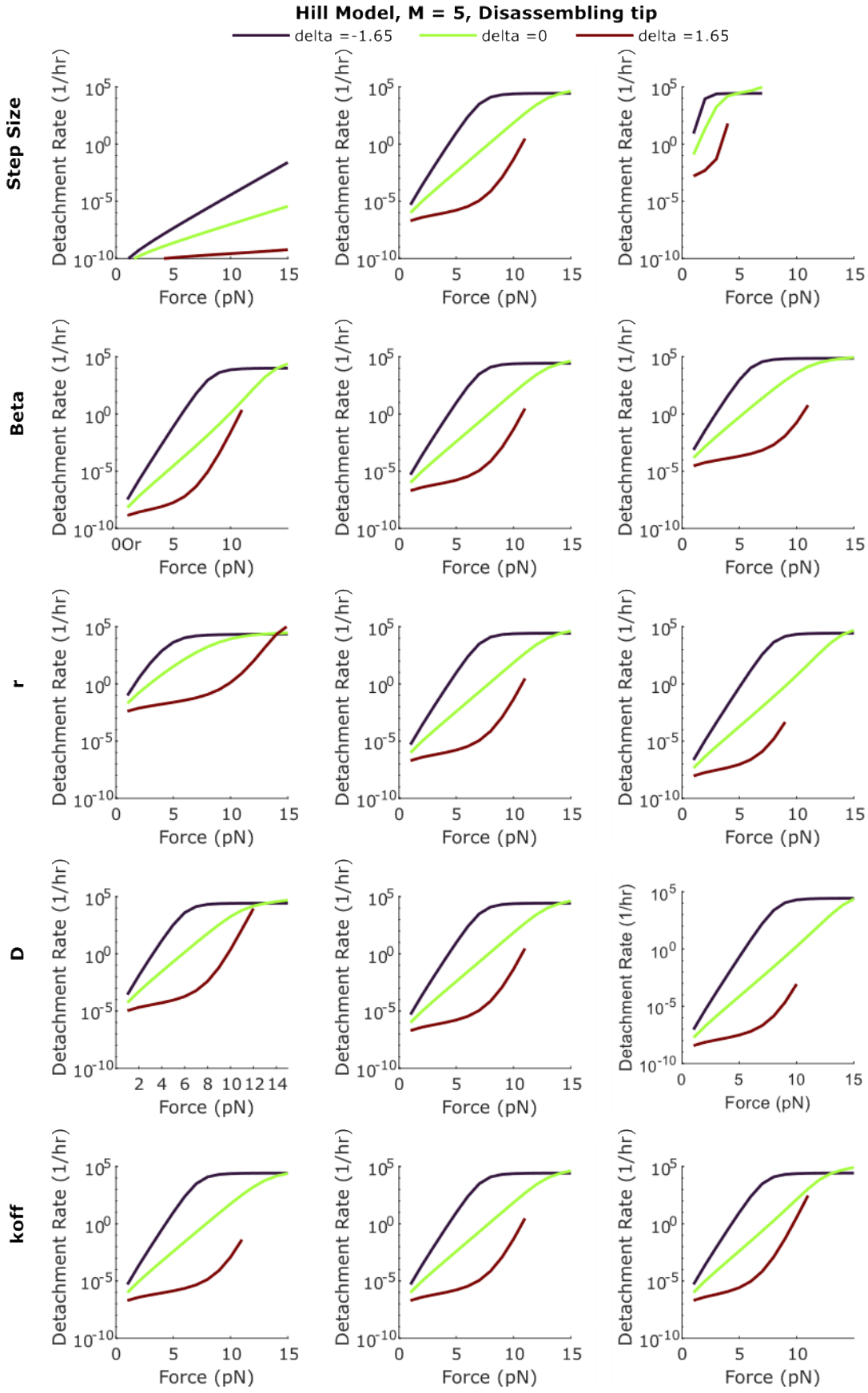
Hill Model, M = 5, Disassembling tip
delta =-1.65
delta =0
delta =1.65
Step Size
Beta
r
D
koff
Detachment Rate (1/hr)
Force (pN)

Figure 5, figure supplement 2: Parameter variation for Hill Model, with a disassembling tip. Plots of detachment rate as a function of force were generated. Each row contains plots for variation of a single parameter. The center-plot corresponds to the default parameter set, the left-most plot corresponds to an e-fold reduction in the parameter, the right-most plots correspond to an e-fold increase in the parameter. The Hill Model remains largely insensitive to all parameters but the step size and molecular roughness factor r.

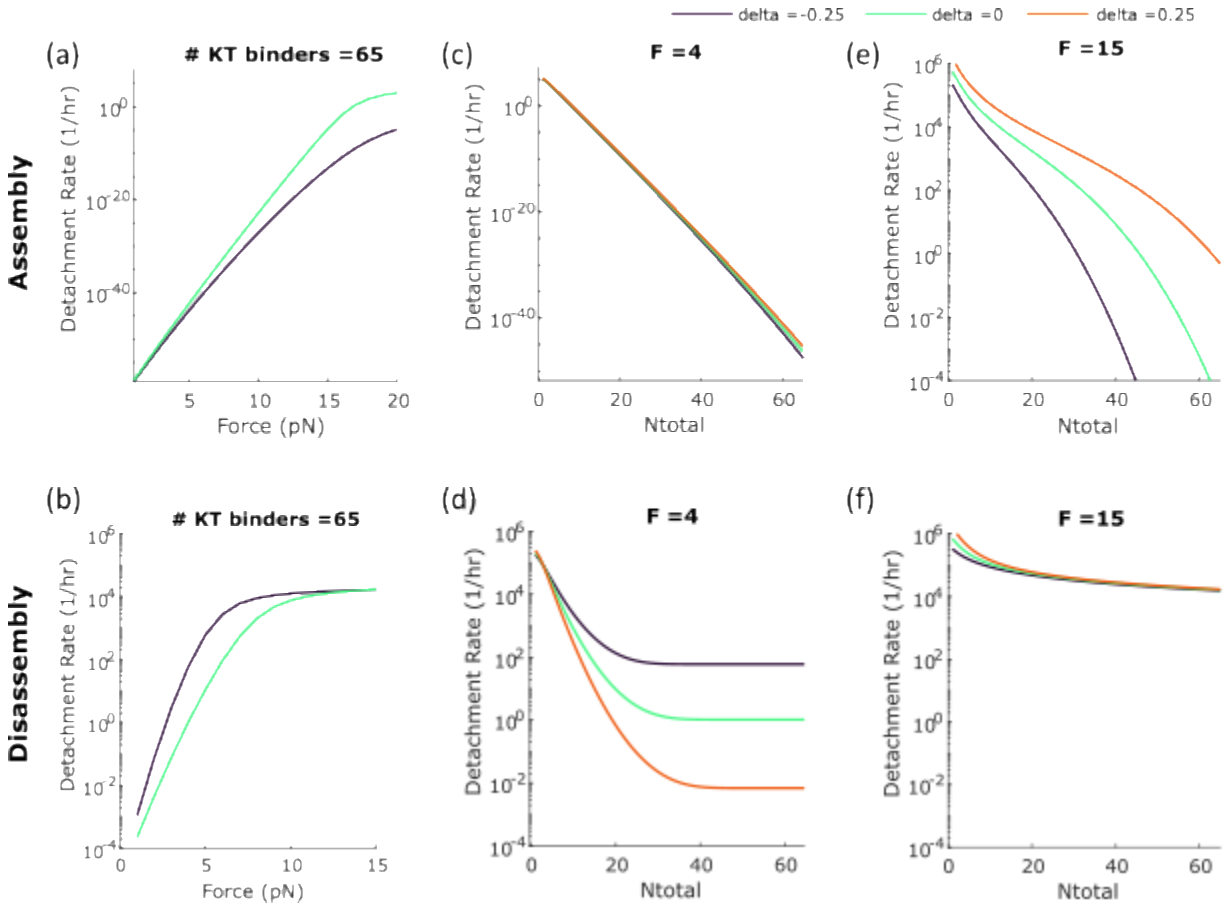

Figure 6: Analytical solutions of the Hill model for parameters chosen by Joglekar and Hunt. (a) Predicted detachment rates vs. force for assembling tips. (b) Predicted detachment rates vs. force for disassembling tips. (c) Predicted detachment rates vs. number of elements in the kinetochore for assembling tips at 4 pN. (d) Predicted detachment rates vs. number of elements in the kinetochore for assembling tips at 4 pN. (e) Predicted detachment rates vs. number of elements in the kinetochore for assembling tips at 15 pN. (f) Predicted detachment rates vs. number of elements in the kinetochore for disassembling tips at 15 pN.

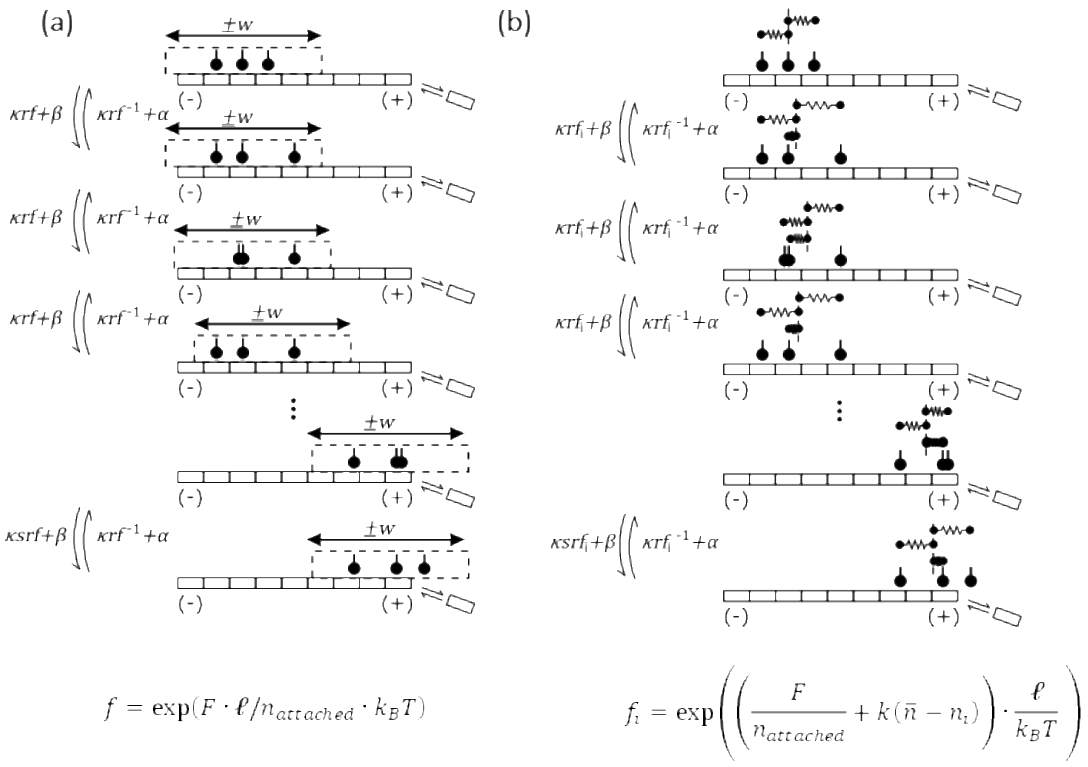

$$f = \exp(F \cdot \ell / n_{attached} \cdot k_B T)$$

$$f_i = \exp\left(\left(\frac{F}{n_{attached}} + k(\bar{n} - n_i)\right) \cdot \frac{\ell}{k_B T}\right)$$

Figure 7: (a) cartoon depicting steps for a “diffusors in a box model” (b) cartoon depicting steps for “diffusors flexibly linked” model. (c) Position traces of “diffusors in a box” model are plotted for a single box width for a 3-diffusor coupler under a variety of forces. (d) Position traces for a “diffusors flexibly linked” model are plotted for a single box width for a 3-diffusor coupler under a variety of forces.

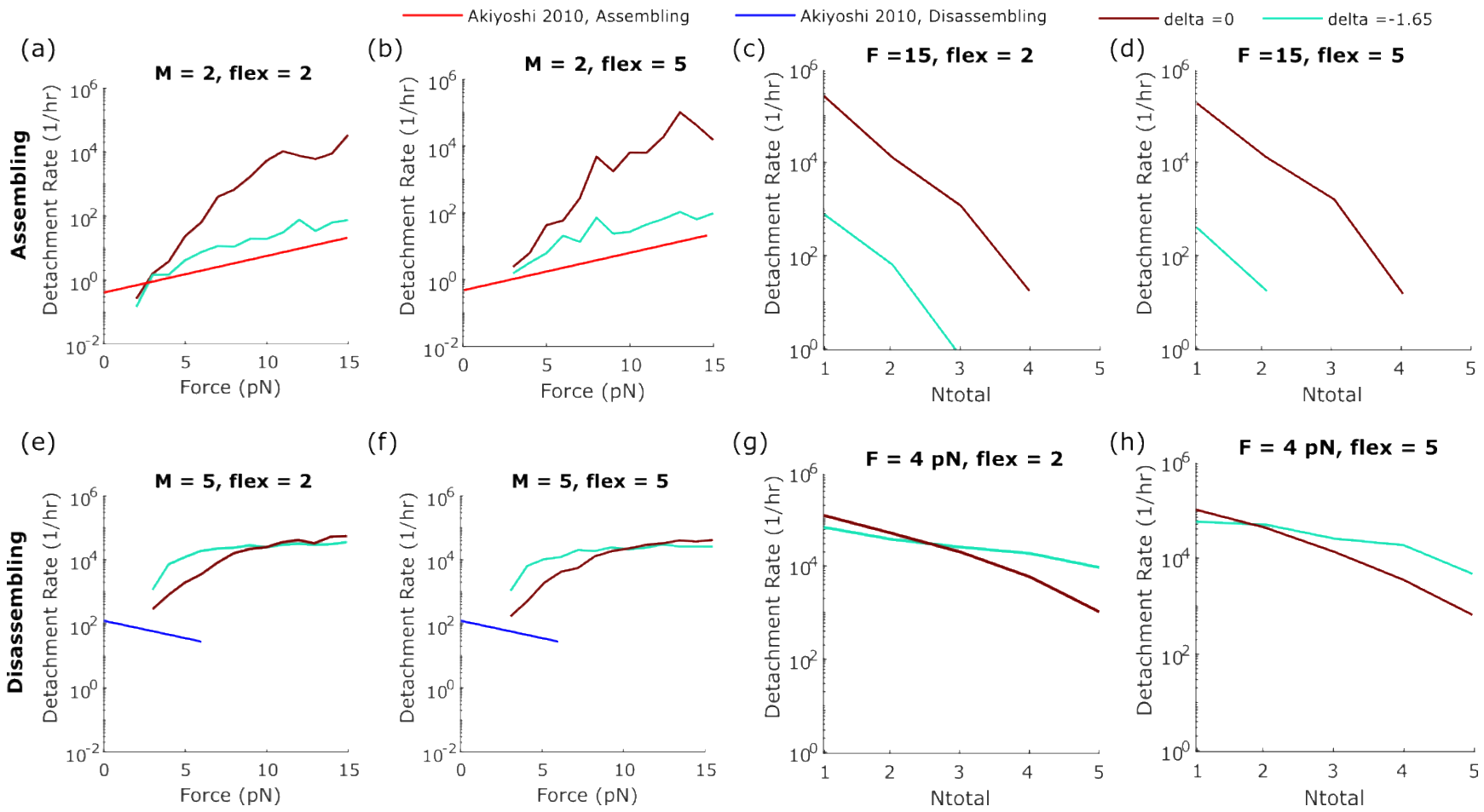
Akiyoshi 2010, Assembling
Akiyoshi 2010, Disassembling
delta =0
delta =-1.65
(a)
M = 2, flex = 2
(b)
M = 2, flex = 5
(c)
F =15, flex = 2
(d)
F =15, flex = 5
(e)
M = 5, flex = 2
(f)
M = 5, flex = 5
(g)
F = 4 pN, flex = 2
(h)
F = 4 pN, flex = 5
Assembling
Disassembling
Detachment Rate (1/hr)
Force (pN)
Ntotal

Figure 8: Diffusors in a box numerical simulation results. The detachment rates for immunoprecipitated kinetochores attached to real microtubule tips as measured in Akiyoshi et al. 2010 are overlayed on the detachment rate vs. force plots for assembling (red) and disassembling (blue) microtubules. (a-b) Detachment rates as a function of force predicted for assembling tips for two different box widths. M denotes the number of diffusors, and flex denotes with box width. (c-d) Detachment rates as a function of number of diffusors in the simulated kinetochore predicted for assembling tips for two different box widths. (e-f) Detachment rates as a function of force predicted for disassembling tips for two different box widths. (g-h) Detachment rates as a function of number of diffusors in the simulated kinetochore predicted for disassembling tips for two different box widths.

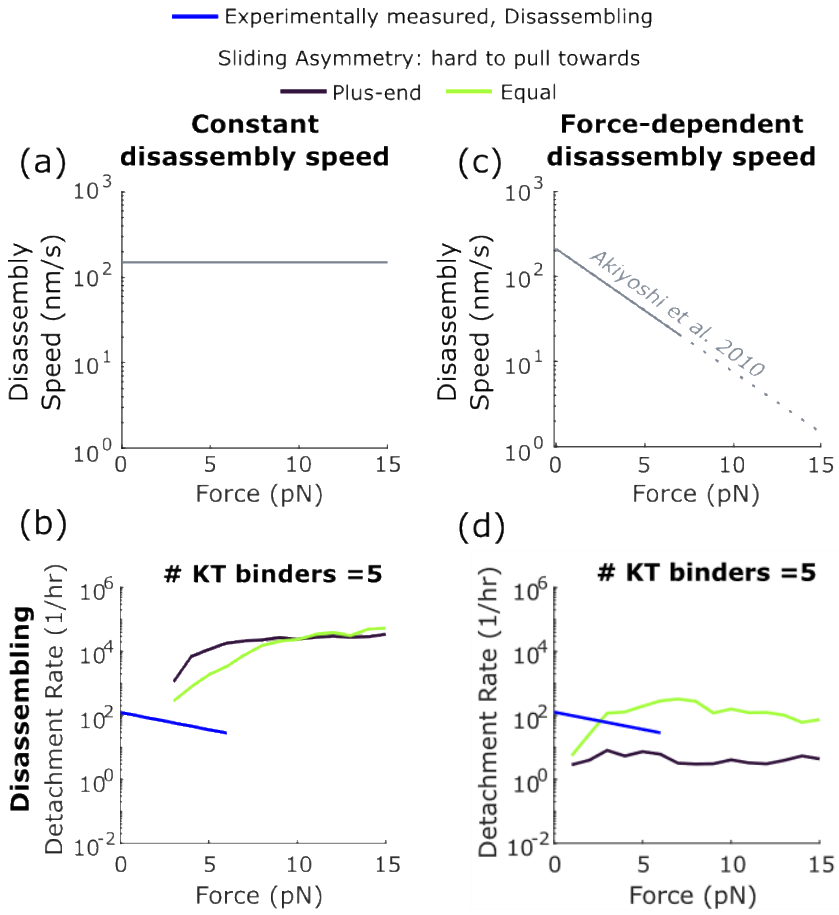

Figure 9: Reductions in disassembly speed with increased force observed in experiment assist in establishing agreement between 'diffusor in a box' model and experimentally determined detachment rates. (a) The disassembly speed-force relationship assumed for prior versions of the model is plotted (the disassembly speed was held constant). (b) The predicted detachment rate for a constant disassembly speed is plotted as a function of force for comparison to experimental data (blue); plot recopied from figure 8e. (c) A function fit to the experimentally determined detachment rate as a function of force is plotted (data sourced from Akiyoshi et al. 2010). Where data does not exist to support the single-exponential fit, the fit is plotted as a dashed line. (d) The predicted detachment rate for a force-dependent disassembly speed is plotted as a function of force for comparison to experimental data (blue).

References:

[1] B. Akiyoshi, K. K. Sarangapani, A. F. Powers, C. R. Nelson, S. L. Reichow, H. Arellano-Santoyo*, et al.*, "Tension directly stabilizes reconstituted kinetochore-microtubule attachments," *Nature,* vol. 468, pp. 576-U255, Nov 2010.

[2] M. P. Miller, C. L. Asbury, and S. Biggins, "A TOG Protein Confers Tension Sensitivity to Kinetochore-Microtubule Attachments," *Cell,* vol. 165, pp. 1428-1439, Jun 2016.

[3] N. T. Umbreit, D. R. Gestaut, J. F. Tien, B. S. Vollmar, T. Gonen, C. L. Asbury*, et al.*, "The Ndc80 kinetochore complex directly modulates microtubule dynamics," *Proceedings of the National Academy of Sciences of the United States of America,* vol. 109, pp. 16113-16118, Oct 2012.

[4] N. T. Umbreit, M. P. Miller, J. F. Tien, J. C. Ortola, L. Gui, K. K. Lee*, et al.*, "Kinetochores require oligomerization of Dam1 complex to maintain microtubule attachments against tension and promote biorientation," *Nature Communications,* vol. 5, p. 11, Sep 2014.

[5] L. A. Helgeson, A. Zelter, M. Riffle, M. J. MacCoss, C. L. Asbury, and T. N. Davis, "Human Ska complex and Ndc80 complex interact to form a load-bearing assembly that strengthens kinetochore-microtubule attachments," *Proceedings of the National Academy of Sciences of the United States of America,* vol. 115, pp. 2740-2745, Mar 2018.

[6] E. A. Geyer, M. P. Miller, C. A. Brautigam, S. Biggins, and L. M. Rice, "Design principles of a microtubule polymerase," *Elife,* vol. 7, p. 23, Jun 2018.

[7] A. P. Joglekar, D. C. Bouck, J. N. Molk, K. S. Bloom, and E. D. Salmon, "Molecular architecture of a kinetochore-microtubule attachment site," *Nature Cell Biology,* vol. 8, pp. 581-585, Jun 2006.

[8] K. Johnston, A. Joglekar, T. Hori, A. Suzuki, T. Fukagawa, and E. D. Salmon, "Vertebrate kinetochore protein architecture: protein copy number," *Journal of Cell Biology,* vol. 189, pp. 937-943, Jun 2010.

[9] A. V. Zaytsev, F. I. Ataullakhanov, and E. L. Grishchuk, "Highly Transient Molecular Interactions Underlie the Stability of Kinetochore-Microtubule Attachment During Cell Division," *Cellular and Molecular Bioengineering,* vol. 6, pp. 393-405, Dec 2013.

[10] B. Shtylla and J. P. Keener, "A MATHEMATICAL MODEL FOR FORCE GENERATION AT THE KINETOCHORE-MICROTUBULE INTERFACE," *Siam Journal on Applied Mathematics,* vol. 71, pp. 1821-1848, 2011.

[11] E. L. Grishchuk, M. I. Molodtsov, F. I. Ataullakhanov, and J. R. McIntosh, "Force production by disassembling microtubules," *Nature,* vol. 438, pp. 384-388, Nov 2005.

[12] T. L. Hill, "THEORETICAL PROBLEMS RELATED TO THE ATTACHMENT OF MICROTUBULES TO KINETOCHORES," *Proceedings of the National Academy of Sciences of the United States of America,* vol. 82, pp. 4404-4408, 1985.

[13] A. P. Joglekar and A. J. Hunt, "A simple, mechanistic model for directional instability during mitotic chromosome movements," *Biophysical Journal,* vol. 83, pp. 42-58, Jul 2002.

[14] A. K. Sharma, B. Shtylla, and D. Chowdhury, "Distribution of lifetimes of kinetochore-microtubule attachments: interplay of energy landscape, molecular motors and microtubule (de-)polymerization," *Physical Biology,* vol. 11, Jun 2014.

[15] J. P. Keener and B. Shtylla, "A Mathematical Model of Force Generation by Flexible Kinetochore-Microtubule," *Biophysical Journal,* vol. 106, pp. 998-1007, Mar 2014.

[16] C. B. O'Connell, A. Khodjakov, and B. F. McEwen, "Kinetochore flexibility: creating a dynamic chromosome-spindle interface," *Current Opinion in Cell Biology,* vol. 24, pp. 40-47, Feb 2012.

[17] Z. Bertalan, C. A. M. La Porta, H. Maiato, and S. Zapperi, "Conformational Mechanism for the Stability of Microtubule-Kinetochore Attachments," *Biophysical Journal,* vol. 107, pp. 289-300, Jul 2014.

[18] A. Efremov, E. L. Grishchuk, J. R. McIntosh, and F. I. Ataullakhanov, "In search of an optimal ring to couple microtubule depolymerization to processive chromosome motions," *Proceedings of the National Academy of Sciences of the United States of America,* vol. 104, pp. 19017-19022, Nov 2007.

[19] N. B. Gudimchuk, E. V. Ulyanov, E. O'Toole, C. L. Page, D. S. Vinogradov, G. Morgan*, et al.*, "Mechanisms of microtubule dynamics and force generation examined with computational modeling and electron cryotomography," *Nature communications,* vol. 11, p. 3765, 2020 Jul 2020.

[20] V. A. Volkovn, P. J. H. in't Veldt, M. Dogterom, and A. Musacchio, "Multivalency of NDC80 in the outer kinetochore is essential to track shortening microtubules and generate forces," *Elife,* vol. 7, Apr 2018.

[21] J. F. Tien, N. T. Umbreit, D. R. Gestaut, A. D. Franck, J. Cooper, L. Wordeman*, et al.*, "Cooperation of the Dam1 and Ndc80 kinetochore complexes enhances microtubule coupling and is regulated by aurora B," *Journal of Cell Biology,* vol. 189, pp. 713-723, May 2010.

[22] V. Bormuth, V. Varga, J. Howard, and E. Schaffer, "Protein Friction Limits Diffusive and Directed Movements of Kinesin Motors on Microtubules," *Science,* vol. 325, pp. 870-873, Aug 2009.

[23] A. F. Powers, A. D. Franck, D. R. Gestaut, J. Cooper, B. Gracyzk, R. R. Wei*, et al.*, "The Ndc80 Kinetochore Complex Forms Load-Bearing Attachments to Dynamic Microtubule Tips via Biased Diffusion," *Cell,* vol. 136, pp. 865-875, Mar 2009.

[24] A. Bar-Haim and J. Klafter, "Escape from a fluctuating system: A master equation and trapping approach," *Physical Review E,* vol. 60, pp. 2554-2558, Sep 1999.

[25] J. Howard, "The movement of kinesin along microtubules," *Annual Review of Physiology,* vol. 58, pp. 703-729, 1996.

[26] G. I. Bell, "Models for the specific adhesion of cells to cells," *Science,* vol. 200, pp. 618-27, May 12 1978.